New Three Phase Photovoltaic Energy Harvesting System for Generation of Balanced Voltages in Presence of Partial Shading, Module Mismatch, and Unequal Maximum Power Points

By

Saleh Mohamed M. Eshtaiwi

Submitted to the graduate degree program in the Department of Electrical Engineering and Computer Science and the Graduate Faculty of The University of Kansas in partial fulfillment of the requirements for the degree of Doctor of Philosophy

Dr. Reza A. Ahmadi, Chairperson

Dr. Jerzy Grzymala-Busse

Committee members: Dr. Rongqing Hui

Dr. Christopher T. Allen

Dr. Elaina J. Sutley

Date Defended: 14 May 2019

The dissertation committee for Saleh Mohamed M. Eshtaiwi certifies

that this is the approved version of the following dissertation:

New Three Phase Photovoltaic Energy Harvesting System for Generation of Balanced Voltages in Presence of Partial Shading, Module Mismatch, and Unequal Maximum Power Points

_____

Dr. Reza A. Ahmadi, Chairperson

Date Approved: 14 May 2019

Abstract

The worldwide energy demand is growing quickly, with an anticipated growth rate of 48% from 2012 to 2040. Consequently, investments in all forms of renewable energy generation systems have been growing rapidly due to growth rate and climate concerns. Increased use of clean renewable energy resources such as hydropower, wind, solar, geothermal, and biomass is expected to noticeably alleviate many present environmental concerns associated with fossil fuel-based energy generation. In recent years, wind and solar energies have gained the most attention among all other renewable resources. As a result, both have become the target of extensive research and development for dynamic performance optimization, cost reduction, and power reliability assurance.

The performance of Photovoltaic (PV) systems is highly affected by environmental and ambient conditions such as irradiance fluctuations and temperature swings. Furthermore, the initial capital cost for establishing the PV infrastructure is very high. Therefore, it is essential that the PV systems always harvest the maximum energy possible by operating at the most efficient operating point, i.e. Maximum Power Point (MPP), to increase conversion efficiency to reach 100% and thus result in lowest cost of captured energy.

The dissertation is an effort to develop a new PV conversion system for large scale PV grid-connected systems which provides 99.8% efficacy enhancements compared to conventional systems by balancing voltage mismatches between the PV modules. Hence, it analyzes the theoretical models for three selected DC/DC converters. To accomplish this goal, this work first introduces a new adaptive maximum PV energy extraction technique for PV grid-tied systems.

Then, it supplements the proposed technique with a global search approach to distinguish absolute maximum power peaks within multi-local peaks in case of partially shaded PV module conditions.

Next, it proposes an adaptive MPP tracking (MPPT) strategy based on the concept of model predictive control (MPC) in conjunction with a new current sensor-less approach to reduce the number of required sensors in the system. Finally, this work proposes a power balancing technique for injection of balanced three-phase power into the grid using a Cascaded H-Bridge (CHB) converter topology which brings together the entire system and results in the final proposed PV power system. The developed grid connected PV solar system is evaluated using simulations under realistic dynamic ambient conditions, partial shading, and fully shading conditions and the obtained results confirm its effectiveness and merits comparted to conventional systems. The resulting PV system offers enhanced reliability by guaranteeing effective system operation under unbalanced phase voltages caused by severe partial shading.

Acknowledgements

First, praise be to Allah and then I would like to express my appreciation and thankful to my advisor, Prof. Reza Ahmadi for his invaluable guidance during my research in the area of power electronics. I also would like to thank him for his insights and supervision throughout my journey as a Ph.D. student. Further, I also would like to thank Prof. Busse, Prof. Hui, Prof. Allen, and the outside examiner Prof. Sutley who have agreed to serve as members in my honorable and revered Ph.D. committee. Their time spent on my dissertation review and the valuable comments and suggestions strengthened my research and helped me to introduce such novel work. I would like to express my gratitude to my mother, sisters, wife for their continued enthusiasm and support throughout my study abroad and also my children for their patience and encouragements. In addition, special thanks to my friends who always present non- discontinued and sustainable support. Finally, my acknowledgement to GECOL mid sector manager and to my indirect sponsor, GECOL for granting me the opportunity to get my degree abroad.

Dedication

To my dear mother, Fatima and to spirit of both my father, Mohamed and my brother Mohamed.

Contents

Table of Figures

List of Tables

Chapter 1

1. Introduction

1.1 Motivation

World energy demand is growing tremendously. Global energy demand jumped by 2.1% in 2017--twice the 2016 rate [1]. As a result, carbon dioxide emissions also rose by 1.4% despite having held steady for almost three years prior to 2017 [1]. Consequently, the environmental issues associated with use of fossil fuels have also exacerbated. Acid rain and global warming are examples that threaten both the earth and humanity. Exhaustion of limited fossil fuel reserves, escalating impacts of climate change, increased power consumption due to population and industrial growth, and oil politics pricing are dire challenges that have resulted in the push toward clean and renewable energy resources [2].

Recently collected data indicates that switching gradually to renewable energy resources and decentralizing power generation has become a major goal of all the developed and a number of emerging countries around the world [3]. However, the cost of electric power generated from renewable energy resources must be able to compete with fossil fuel-based electricity generation in order to be considered a serious alternative to conventional power plants. Consequently,

developing highly efficient renewable energy systems that offer a competitive price advantage over conventional generation systems is the main goal of research and development efforts toward next generation photovoltaic (PV) systems [4].

1.2 Renewable Energy Trends

Figure 1. 1 illustrates the global renewable energy capacity growth from 2007 to 2017 [5]. This figure indicates that a significant portion of renewable energy generation is still based on hydropower, but there has been a steady growth in wind and solar generation with a slight rise in biomass energy. In 2017, the cumulative additions to worldwide renewable energy generation reached 178 GW while the same figure was 138 GW by the end of 2013. Hence, the renewable energy growth rate was around 29% in the period of four years, i.e., 10 GW per year. Moreover, it can also be clearly seen that the total renewable generation capacity more than doubled in a period of ten years thanks to capacity additions in wind and solar energy [5].

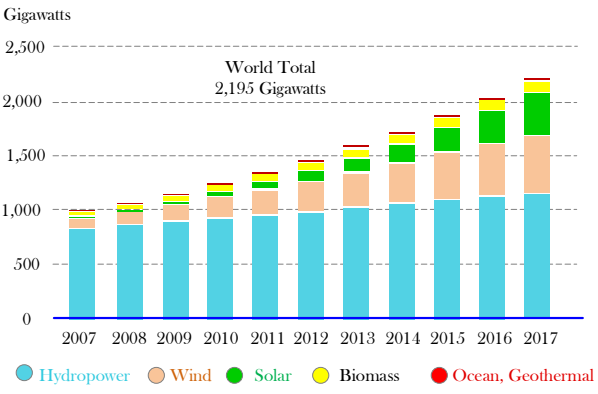

Figure 1.1: The global renewable energy capacity growth (2007-2017) [5]

Figure 1.2 shows the history and projection of all traditional and nontraditional power resources. The renewable energy record performance forms the bedrock of the future growth expectation. Therefore, the forecasted renewable energy curve illustrates that generated power

from renewable energy will exceed 60% by 2045 [6]. The projection also indicates that the world will no longer count on fossil fuels as a conventional resource. The anticipated renewable energy growth will gradually increase to reach 920GW by 2022, whereas the total expected power under the accelerating case might increase to more than 1,150 GW by 2022 [6]. Thus, according to the U.S. Energy Information Administration (eia), the electrical power generated from renewable resources will see a strong expansion rate of 43% in 2022, a rate that was only 12% from 2016 to 2017 [6].

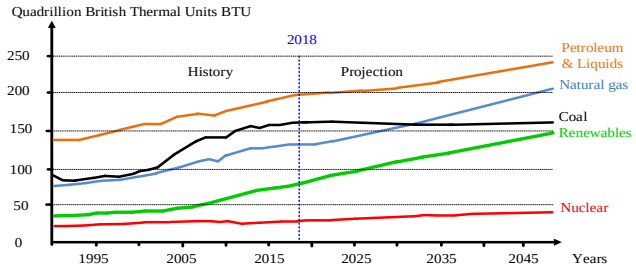

Figure 1.2: World Energy Consumption by Source (1990-2045) [6]

In general, as stated by eia, most generated power will come from PV solar systems and will present the highest capacity additions for the next five years starting from 2019 to 2024, mainly in China and India [7]. The following subsections introduce the various types of available renewable energy and their tradeoffs.

1.2.1 Geothermal Energy (Earth Heat)

Geothermal energy is harnessed from heat continuously generated by the earth and is used daily to heat water and buildings in addition to generating electricity by using hot steam to power turbines [8]. In 2015, the total electric power generated from geothermal energy in 22 countries around the world was approximately 76 billion kWh [9]. In 2017, Indonesia led the world by generating 39% of the total world capacity and Turkey came in second with 34% [8-10].

1.2.2 Hydropower Energy

Hydropower availability is limited to countries that have rivers flow and waterfalls. In addition, establishing hydropower plants is restrained by natural rainfall resources, geographic topology, and water flow rate, and thereby it will necessitate creating dams to control the flow rate through the hydro turbines to generate electricity on demand. Despite these restrictions, Figure 1.1 shows that the global capacity of hydropower ranks first among all other renewable energy resources. In 2017, total global hydropower capacity slightly increased to almost 1,114 GW [11]. Therefore, it is expected to keep increased but with very slow rate [11].

1.2.3 Wind Energy

Wind energy is a free, unlimited, and clean source of energy that can be harvested on a large scale. Figure 1.3 illustrates a period of ten years of the global wind turbine capacity and annual additions that indicate upward growth.

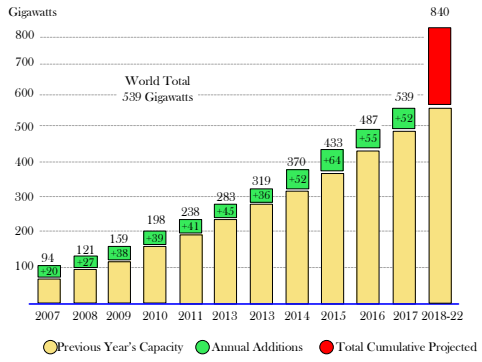

Figure 1.3: Wind turbine capacity globally and annual additions 2007-2017 [5]

However, promising locations for wind turbine farms are limited to rural areas or offshore sites. An intensive and long-term site survey study is required to evaluate the feasibility of founding a wind farm in terms of wind continuity and speed variation rate. Although the advantages of wind energy are more apparent than the disadvantages, wind farms come with

several drawbacks including high initial construction cost, low reliability, high maintenance, and noise. Noticeably, hydropower and wind turbines are both abundant energy resources, but availability and feasibility limit them from widespread use [5] [12].

1.2.4 Biomass Energy

Biomass or biopower energy is a renewable energy resource. As Figure 1.4 illustrates, examples of biomass include all organic physical material such as agriculture crops, animal manure, plants, etc. These materials absorb solar energy and store it in the form of chemical energy. This is a natural process called photosynthesis.

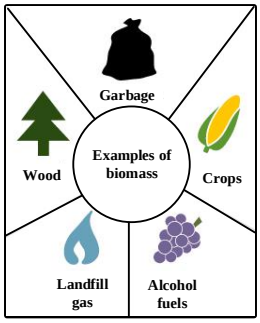

Figure 1.4: Examples of biomass energy [13]

Biomass energy is normally extracted by either direct burn or indirectly by converting the material to fuel, called liquid biofuels, which are then burned to release the potential energy as heat. The heat usually powers steam turbines to generate electricity [13].

1.2.5 Solar Energy

Solar energy is available wherever the sun shines. Considering the advantages of solar energy, solar is the most favorable and promising source of energy among all other sustainable energy resources. In the past decades, the energy generated from solar power is growing noticeably thanks to the use of PV systems. PV solar systems require limited maintenance, especially when

no power storage is included. Currently, the PV solar industry is witnessing huge technological improvements and rapid development. China is the largest manufacturer of PV systems and the world leader in PV generation capacity. China was the first country to exceed 100GW of total global cumulative PV capacity [14]. Figure 1.5 shows the top ten countries in PV solar generation in 2017 and the annual expected additions [5].

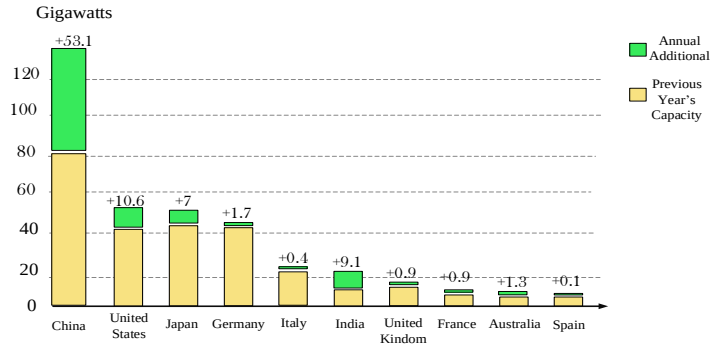

Figure 1.5: Solar PV capacity and additions in top 10 countries, 2017 [5]

A drawback of solar energy is that the sun is only available during the day; hence, solar energy has to be stored for later use, which adds an extra cost.

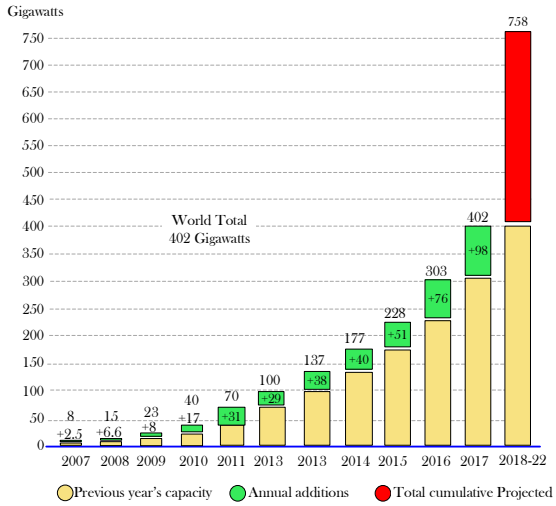

Figure 1.6: Solar PV global capacity and annual additions 2007-2017 [5]

PV solar systems generate abundant, cost-effective, inexhaustible, clean power. However, two

major defects hinder their development: the manufacturing cost and the low photovoltaic conversion efficiency. Most PV modules have efficiencies as low as 9% to 18%. Today, the modules available in the market reach efficiencies of 22.5%. Therefore, improving technologies implemented to control PV systems and raising the efficiency by extracting the maximum available power is crucial for the future of PV industrial competition. Figure 1.6 shows the annual additions of PV solar power systems. At least 98 GW DC power was added worldwide by 2017. The global PV solar capacity increased by 33% and the world total hits 402 GW [5]. By 2022 will exceed 758GW and by 2025 will surpass 969GW [15].

1.3 Photovoltaic Modules (PV):

Edmund Becquerel first discovered the PV effect in 1839 using copper oxide in an electrolyte. In 1954, the PV conversion was revealed by Bell Telephone when an element found in sand (silicon) created an electronic charge when exposed to sunlight. A PV module, or panel, is made up of several individual cells with positive and negative polarity for each layer [16]. The first generation of solar cells were made from silicon, while the second generation was manufactured from a thin-film of vapor-deposited on the silicon layer on a carrier, e.g., glass. Currently they are made from thin films comprising copper, indium and selenium. PV manufacturing cost limits quick growth and widespread use. Therefore, an existing challenge is a tradeoff between cost reduction and technological development. It is absolutely true that the technology leads to an obvious efficiency improvement, but it will temporarily increase the PV module's cost.

1.3.1 PV Solar Cell Structure

The PV cell is made of essentially two layers of silicon, P-layer and N-layer. The boundary

between them acts as a diode. Thus, only electrons can move from the N to P-layer, when sunlight (photons) strikes the surface of the solar cell. The photons contain particles of energy that are absorbed by the top layer, which is the N-layer as shown in Figure 1.7. The energy causes electrons to become energized and then released from a covalent bond. This produces free electrons that start moving from the N to P-layer and leave behind a hole that can accept other electrons. The holes drift toward the P-layer material side and likewise electrons move toward the N-layer. Therefore, an electrical field across the P-N junction will be induced and sunlight can easily separate the electrons and holes, generating electricity [16-19].

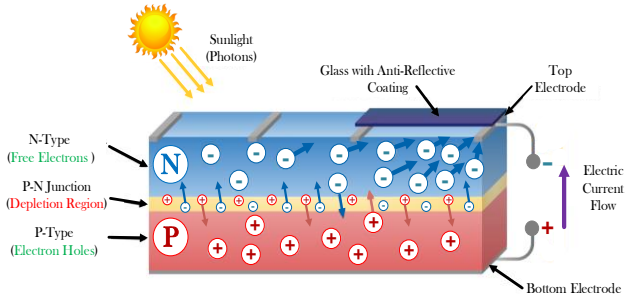

Figure 1.7: The structure of the PV cell [20]

1.3.2 Concepts of PV System Modeling

A common model of a PV cell is shown in Figure 1.8. Based on the operating point on the I-V curve, the real PV cell behaves as either a voltage source or a current source as illustrated in Figure 1.9.

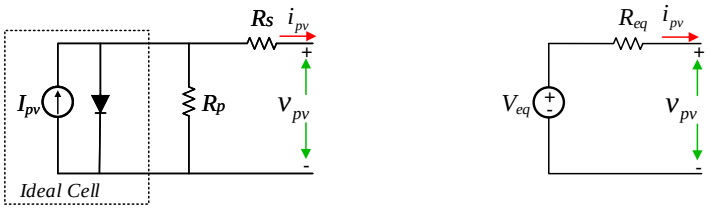

a. Equivalent model of an ideal and practical PV cell b. Equivalent model of PV cell as a voltage source.

Figure 1.8: Equivalent circuit of the PV cell

In Figure 1.8 (a), i_{pv} is the PV current source and R_p represents parallel resistance whose influence is stronger in the current source region of operation, and R_s represents series resistance whose impact is influential when the PV cell operates in the voltage source region. The R_s resistance is the sum of several structural resistances of each PV cell.

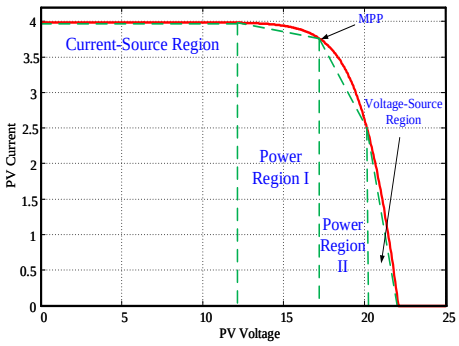

Figure 1.9: The I-V characteristic of BP365 for a certain insolation level and temperature.

Equation (1.1) defines a PV cell that is shown in Figure 1.8 (a) and represents the I–V characteristic of a real PV panel. The real PV panel is made from several connected PV cells, and for complete observation, Equation (1.1) considers the characteristics at the terminals of each PV panel and requires the inclusion of additional parameters,

$$i_{pv} = I_{pv} - I_o\left[\exp\left(\frac{v_{pv} + R_s i_{pv}}{v_t a}\right) - 1\right] - \frac{v_{pv} + R_s i_{pv}}{R_p} \qquad (1.1)$$

Where I_{pv} and I_o are the PV and saturation currents, respectively, of the array.

v_{pv} : PV input voltage.

i_{pv} : PV input current.

v_t : Thermal voltage, $v_t = N_s kT/q$.

N_s : Number of cells connected in series.

k: Boltzmann constant, $k = 1.3806503 \times 10^{-23}\ J/k$.

q: Electron charge, $q = 1.60217646 \times 10^{-19} C$.

T: Temperature of the $p-n$ junction in Kelvin.

a: Ideality constant of the diode

Further, as shown in Figure 1.8 (b), linear approximation is needed since the I-V characteristics of a photovoltaic cell are nonlinear. In the meantime, the ratio of the voltage on a photovoltaic cell to the current flowing through the PV cell varies with either the voltage or current. Therefore, the change rate in voltage to the change rate in current is identified as the dynamic resistance and is simply obtained from the slope of I–V curve.

Figure 1.9 shows realistic linearization at a chosen operating point and is a valid approximation of the PV cell for a small signal design analysis at the vicinity of that point. When the PV module is connected to a DC/DC converter, the dynamic behavior of the system will depend on the operating point of the PV module.

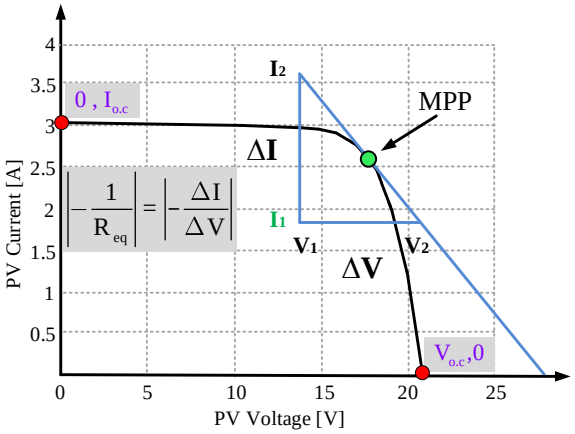

Figure 1.10: Dynamic resistance at the chosen operating point

As a result, the convertors must be designed to operate at the MPP in addition to several adjacent operating points. V_{eq} is Thevenin's voltage source and can be computed by Equation (1.2)

and dynamic resistance is denoted by R_{eq} of the PV module in Figure 1.8 (b), which can be obtained by Equation (1.3),

$$V_{eq} = V_{pv} + R_{eq} I_{pv} \tag{1.2}$$

Hence;

$$R_{eq} = -\frac{1}{I_{pv}} V_{pv} + \frac{1}{I_{pv}} V_{eq} \tag{1.3}$$

1.3.3 Characteristics of (I-V) and (P-V) Curves

The output of the PV panel is highly dependent on ambient and environmental factors. The voltage and current of PV cells are varied nonlinearly with changes in ambient temperature and irradiance.

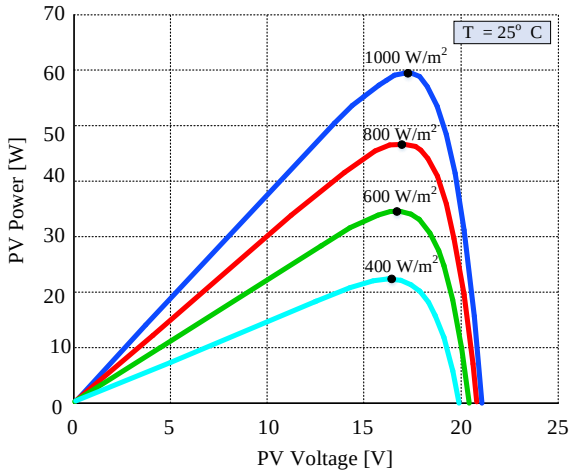

(a). The P-V characteristics curves of BP 365 PV module for various levels of irradiance and constant temperature

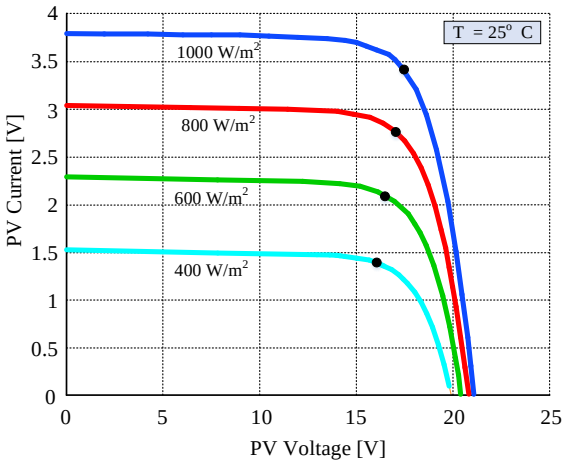

(b). The I-V characteristics curves of BP 365 PV module for various levels of irradiance and constant temperature

Figure 1.11: I-V and P-V curves characteristics in terms of solar irradiance change

As a result, the amount of power generated by the PV panel is a function of many parameters, most notably, local solar radiation, panel temperature, and panel voltage. The power-voltage (P-V) and (I-V) characteristic of a BP365 solar panel for different insolation levels and temperatures is illustrated in Figure 1.11 and Figure 1.12. Typically, the power converter is responsible for regulating the panel voltage to achieve the maximum output power by using a

maximum power point tracking (MPPT) algorithm. Figure 1.11 illustrates the PV cell under various levels of irradiance while the ambient temperature is kept constant at 25C^{o}. The operating point shifts slightly, causing a small voltage to drop at the PV terminals. The change in irradiance can is affected by wind speed and can occur gradually or suddenly in the case of cloudy days.

Figure 1.12 shows the effect of temperature variations on MPP location and how the MPP location shifts at different levels of temperature while the irradiance is set to 1000 W/m^2. Typically, the PV voltage drops when the temperature keeps increasing. The variations on the irradiance and temperature require a power converter and a robust MPPT technique to professionally address all unexpected challenges and result in an accurate MPP. Figure 1.12 shows clearly that finding the MPP might be very challenging and tricky when temperature variations occur since MPP moves horizontally rather than vertically within the P-V curve; however, in comparison, radiation step change seems to be more manageable and experimentally accessible when the MPP moves vertically.

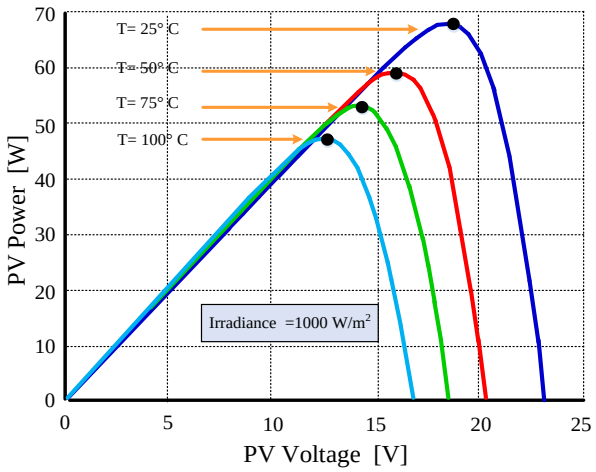

(a). The P-V characteristics curves of BP 365 PV module for various levels of temperature and constant irradiance

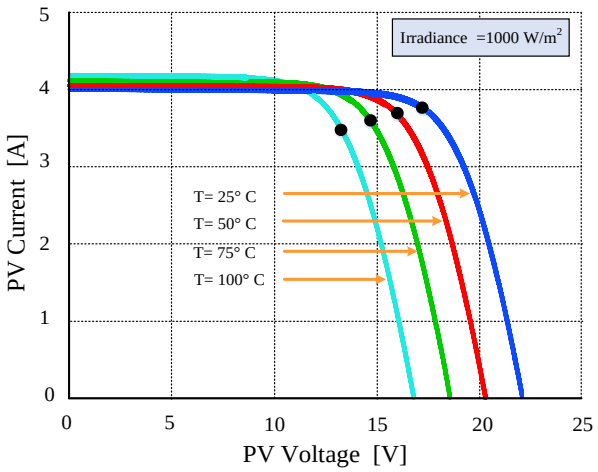

(b). The I-V characteristics curves of BP 365 PV module for various levels of temperature and constant irradiance

Figure 1.12: I-V and P-V curves characteristics in terms of ambient temperature change

In conclusion, according to irradiation and temperature changes, the output voltage can vary widely. At a constant temperature, the output power is increased once the irradiation is increased. At a constant irradiation, the relationship reverses. Thus, the output power increases if the temperature decreases. The output voltage of the PV module should be controlled at an appropriate level to obtain maximum power from the PV module. MPPTs are methods commonly known as real-time optimization approaches. They can identify the maximum power point (MPP) of a PV module throughout the P-V curve where power delivery is at the highest possible level. These techniques are used to maximize the PV captured power in various conditions of ambient temperature and solar irradiance levels.

1.3.4 Partial Shading of PV Modules

Partial shading is a common mismatch phenomenon encountered by the photovoltaic modules that leads to a significant power reduction. The partial shading occurs when a number of PV cells or a couple of modules in a string are partially or entirely covered.

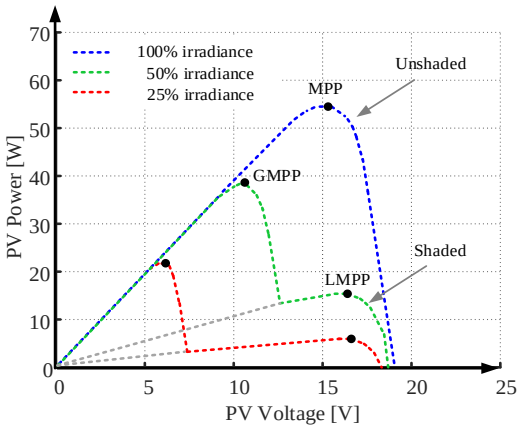

Figure 1.13: Global and local MPP on a power-voltage (P-V) curve.

The obscurations block the sunlight from hitting a single PV surface or larger PV arrays as a result of shading movement during daylight [21-25]. Meanwhile, under non-uniform irradiation

conditions, the P-V characteristics have only one global peak or global maximum power point (GMPP), whereas the P-V curve will contain multiple local maximum power points (LMPP), depending on the number of shaded modules. Figure 1.13 shows P-V curves with different levels of partial shading. During partial shading, the P-V curve characteristics become more complex because of multiple peaks that occur while modules under various irradiances are present. Due to the power mismatch, modules in the same string generate different voltages while conducting the same current [26-30].

In fact, to avoid damages due to module reverse bias, each module in a string must have a bypass diode. The characteristics and configuration of bypass diodes were analyzed previously [31-35]. The bypass diode is connected parallel to the terminal of each panel, as is the blocking diode, which is connected in a series at the positive terminal of every string to avoid damaging the PV modules due to a negative current that flows through each shaded cell.

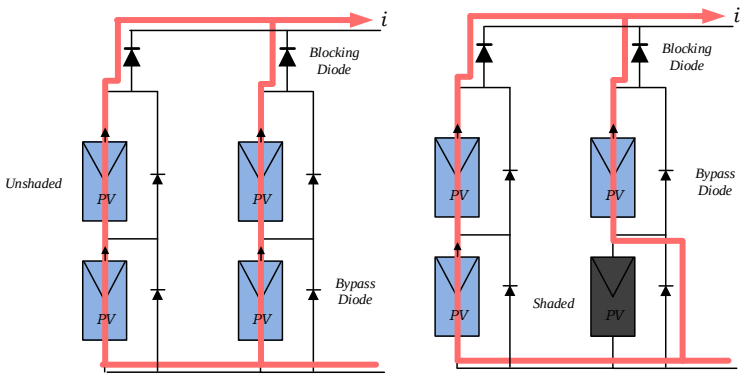

Figure 1.14: Bypass and blocking diodes in photovoltaic arrays

Additionally, under partial shading conditions, the PV module voltages decrease and become negative as a result of irradiance reduction. Consequently, the PV will be turned off by the bypass diodes, resulting in multiple peaks that appear in the P-V curve, as shown in Figure 1.13 and Figure 1.15 [23-26, 30, 36, 37]. Figure 1.14 illustrates bypass and blocking diodes connecting to PV

panels and the direction of current flow before and during partial shading. Therefore, using only maximum power tracking methods will lead to the wrong power peak, causing significant loss of energy. For example, in a partial shading condition of 20 PV modules with 15 unshaded modules at standard test conditions (STC) and 5 shaded modules under 400 W/m^2, a conventional MPPT technique would lead to an energy loss of 25% due to tracking a local peak.

During the daylight, PV panels may encounter different partial shading scenarios. Therefore, specific methods are required to take the strings operation point to the precise GMPP. In general, two important sets of approaches exist: a hardware-based method that changes the PV array configurations dynamically to increase the output power, and a software-based method that sweeps the operation voltage over a wide range through the P-V curve to find the GMPP using different global search techniques.

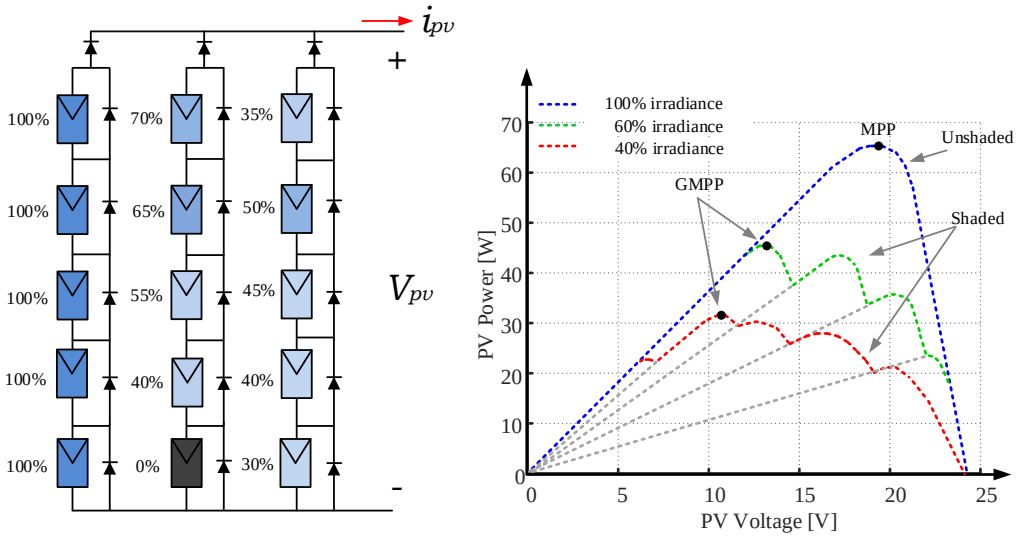

Figure 1.15: Additional power peaks on P-V curve due to partial shading.

The MPPT with global search can simply scan the PV curve and store the power peak information while sweeping and distinguishing the GMPP correctly to impose the balancing of the output power at DC/DC power stage terminals.

In conclusion, partial shading apparently has inevitable or unavoidable consequences that impact the PV solar systems production. Either hardware schemes or software-based methods can successfully identify the global peak. However, software-based methods are widely implemented due to higher reliability and lower costs.

1.4 Contributions

This dissertation introduces a three-phase grid-connected PV solar system that can guarantee generation of balanced three-phase voltages and currents in case of either MPP voltage mismatch of PV arrays or partial shading conditions. The proposed PV system is designed using a cascaded H-bridge (CHB) multilevel inverter topology for the grid interface. The inputs to the CHB's power cells are DC/DC power converters fed from PV modules. A litany of important contributions enables the design of the proposed PV system as follows.

1. At the CHB inverter control level, a new control scheme is proposed that can generate balanced voltages and currents even when the voltages of power cells are unequal due to intrinsic mismatches or unequal insolation of PV modules that result in unequal MPP voltages. The proposed method uses the concept of fundamental phase shift compensation (FPSC) to balance the inverter voltages by modifying the phase angles of line-ground inverter voltages. Also, at this level, a power injection control algorithm is implemented to freely control the flow of active and reactive power.
2. At the MPPT level, a new adaptive MPPT strategy based on the model predictive control (MPC) approach is proposed, which provides excellent power tracking performance in case of ambient and environment fluctuations. The proposed MPPT method is also enhanced by developing a new global power tracking capability that can identify the MPPT even in the case of partial shading of PV modules.
3. At the DC/DC converter control level, a new sensorless current control technique is proposed that allows for estimating the input current (and thus power) of the DC/DC converter without

the need for a current sensor. This would reduce the cost and complexity of the entire system, which is designed using several DC/DC power converters.

1.5 Overview of Dissertation

The remaining chapters of this dissertation are organized as follows. Chapter 2 presents the findings from the literature review of the existing conventional maximum power point tracking techniques. This chapter also reviews global search methods and current sensorless techniques. It also provides a review of techniques for balancing of three phase voltages using a CHB converter.

In Chapter 3, the first section finds the transfer functions of three important DC/DC converters. The derived transfer functions are used to analyze the dynamic performance of each converter. Next, it explains the model predictive control theoretically and the procedure for developing a specific model that can be effectively used for MPPT based on MPC. Then, the proposed global search strategy is explained, which alleviates the consequences of partial shading conditions and successfully reduces the effect of power losses by extracting maximum available power. Then this section introduces the design of the proposed current sensorless model. The following section details the employed power injection models and their application to the CHB converter. Finally, this chapter ties together the discussed elements of the system and proposes the voltage balancing technique for a high level of control of the CHB for balanced power operations.

In Chapter 4, the proposed systems and approaches are verified using experimental results as well as simulations. The first section verifies the dynamic performance of three DC/DC converters and presents the obtained results. Then, the experimental results of the new harvesting strategy as well as a comparison between the proposed technique and the most common methods are displayed

and discussed. The obtained outcomes of the proposed new control scheme that describes the dynamic performance are also included and analyzed.

Finally, in Chapter 5, the dissertation provides a conclusion to summarize all contributions and outcomes.

Chapter 2

2. Literature Review

This chapter presents a brief overview of previous approaches that sought to address the challenges that restrain the power harvesting of PV solar systems under various ambient changes including partial shading conditions. It also provides finding of current sensorless model in addition to previous research of grid power injection methods and phase shift compensation using a cascaded H-bridge converter to balance three phase waveforms.

2.1 Traditional Maximum Power Harvesting Methods

Several maximum power point tracking (MPPT) techniques have been proposed to search and continuously maintain the maximum power point. In general, MPPT techniques monitor the output of PV solar systems and impose a controlling command to extract the maximum available power from daylight regardless of ambient environment changes. Perturb and observe (P&O), hill climbing, and incremental conductance (IncCond) are the most commonly used techniques for low-cost applications and simplicity. All these MPPT methods consider the characteristics of the P-V curve to determine the MPP. In recent years, numerous methods have been explored to track

the MPP. These include an optimized and developed version of traditional MPPT methods [38-43] , such as optimized perturb and observe (OPO), estimated perturb-perturb (EPP), or adaptive P&O. New advanced and artificial intelligence techniques-based approaches also exist, which provide high levels of efficient performance and accuracy such as fuzzy logic control (FLC) and artificial neural networks (ANN). Furthermore, hybrid strategies have also been introduced to improve the performance of the traditional methods by integrating methods, such as combining P&O with ANN and fuzzy logic with IncCond [44]. The idea behind the proposed methods is to balance cost, complexity, and accuracy. The authors try to classify a number of the proposed methods in the literature based on factors such as ease of implementation, effectiveness, and convergence speed [45]. Consequently, they are subject to increased tracking time, which may cause extra power loss due to significant delays or complexity and possibly increased costs. Next, four widely recognized MPPT algorithms and other sophisticated MPPT versions are studied and compared in this chapter. The next sections offer a brief description of each previous work strategy.

2.1.1 Perturb and Observe (P&O)

This technique is one of the simplest and most well-known among MPPT algorithms in the literature [46-49]. P&O works by perturbating the input voltage repeatedly by fixed steps in a given direction and then observing the resulting change in power. Then, P&O is going to decide to change direction of the voltage step once a drop-in power is detected. A small step size will reduce the oscillation around the maximum power point but will result in slow tracking speed, while a big step size results in fast tracking but with high oscillations.

2.1.2 Hill Climbing Method

Hill climbing is the most commonly used technique to achieve maximum power. This method is similar to the P&O technique except the perturbation is in the duty cycle instead of the voltage. In the work of [50], the method alters the duty cycle of the DC/DC power electronic converters in the direction that results in an increase in the generated power. Another way the publications use the hill climbing technique is to locate GMPP after analyzing the solar irradiance pattern [51].

2.1.3 Incremental Conductance (IncCond) Method

Incremental conductance MPPT technique, or IncCond, was proposed to eliminate PV voltage oscillation. The theory of IncCond refers to the fact that the slope of the P-V curve is equal to zero at the MPP, and it is negative on the right side of MPP, positive on the left. A PI controller is usually used in IncCond to regulate and guide the calculated slope to zero by altering the input voltage of the selected DC/DC converter. Therefore, the purpose behind the incremental conductance MPPT method is to diminish any resulting oscillation in the output power [52] [49]. The maximum power is then tracked and attained by comparing the incremental conductance $\Delta I/\Delta V$ to the instantaneous conductance I/V. Once the system reaches the MPP, the operation is preserved.

2.1.4 Estimated Perturb-Perturb (EPP) Method

This method is introduced in [53] to improve the tracking speed and dynamic response to the ambient environmental conditions. This method is similar to the P&O method except that it implements one estimate process for every two perturb processes while searching for MPP. The details and a block diagram representation of this method can be found in [53].

2.1.5 Optimized P&O (OPO) Method

This method is introduced in [54]. In the conventional P&O method, the perturbation step size has a fixed value; however, in optimized P&O, an average of different samples of the PV power is used to dynamically alter the size of perturbation steps. The idea behind altering the step size is to reduce the oscillations around the MPP and improve the performance of the conventional P&O method. More details and the block diagram representation of this method is published in [54].

2.1.6 Fuzzy Logic Control (FLC)

The structure of fuzzy logic is composed of three processes: fuzzification, lookup table of rules base, and de-fuzzification [55]. The numerical input variables are converted based on a membership function to fuzzy variables known as linguistic variables. A membership function might be in the form of triangular, trapezoidal, or Gaussian, and the symmetry or asymmetry of the membership function depends on the importance of the fuzzy level.

The rule base table contains fuzzy levels such as NB (negative big), NS (negative small), ZE (zero), PS (positive small), and PB (positive big). Additional levels might be added to emphasize the desired level of accuracy, such as NM (negative medium) or PM (positive medium) [56]. More importantly, linguistic variables are assigned on rule base tables based on the chosen DC/DC converter so that different converters will have different rule bases. Further, most conventional fuzzy levels used for tracking MPP consist of two inputs and one output. The output might be voltage reference, current reference, or duty cycle. Fuzzy logic controller based MPPT techniques are also available in [57]. Compared to the conventional methods, they improve the tracking performance under variation of ambient atmospheric conditions. However, establishing

the proper fuzzy rules mainly depends on trial and error; therefore, it is greatly affected by the best of the user's experience. In [58], both fuzzy-logic and a dual MPPT controller were implemented. One of MPPT controllers tracks the sun over the azimuth axis and elevation axis angles to achieve maximum solar radiation. The other controls DC/DC buck converter using MPPT algorithm and applies a new FLC-based P&O technique and voltage control approach to continue harvesting the maximum available power. In [59], an adaptive P&O algorithm is presented that makes use of fuzzy logic control to change the operating point according to changes measured in power and voltage. Other previous research found in [60] uses a single phase multilevel cascaded H-bridge inverter with fully fuzzy logic.

2.1.7 Artificial Neural Networks (ANN)

Artificial neural networks (ANN) have also been utilized in the MPPT methods to find the optimum voltage point [61]. Extensive training is required, and the training uses enormous amounts of real collected data at various possible temperature and irradiance conditions. The ANN structure generally builds from three layers: input, hidden, and output layers. The data will include panels, open circuit voltage, and short circuit current. The output is usually one or several reference signal(s) such as a duty cycle or voltage reference. The accuracy of ANN depends on the algorithms used by the hidden layer and how well the neural network is trained. The links that connect between each single node contain the weights. To accurately identify the MPP, the weights are carefully determined through a training process, whereby the PV array is tested over months or years and the patterns between the input(s) and output(s) of the neural network are recorded. Since most of the PV arrays have different characteristics, a neural network must be trained for a specific array. The characteristics of a PV array also change with time, implying that the neural

network must be periodically trained to guarantee accurate MPPT. The above-mentioned methods are known as heuristic techniques, and their operation can be summarized as disturbing the PV system, observing the effect, and then taking the appropriate action. The drawback of using ANN for MPPT is that the network weights must be properly tuned using a large amount of training data. In [62], a genetic algorithm trained a radial basis function neural network-based model to carry out the maximum power point tracking for grid-connected PV power generation control systems. The hidden layer of the neural network is self-organized by the genetic algorithm-based radial basis function growing algorithm. The trained ANN model based MPP model is then employed to predict the maximum power points of a PV array using measured environmental data. In [63], Figure 2.1 shows a classification diagram of various MPPT techniques that are used in PV harvesting techniques [64-66].

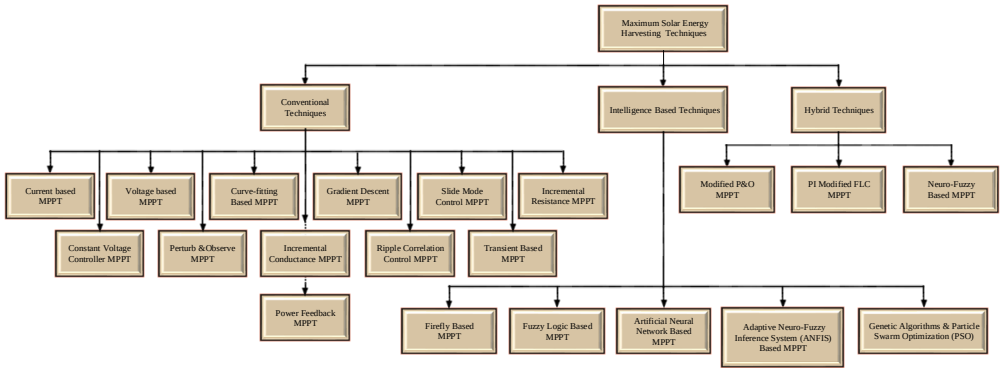

Figure 2.1: Classification of MPPT methods

2.2 Some Approaches to Reduce the Effect of Partial Shading

Partial shading is a nonhomogeneous sun insolation and the P-V curve of the PV solar system exhibits multiple peaks. Certainly, the partial shading decreases the overall operational efficiency of the PV solar system due to output power reduction All traditional MPPT techniques are designed to maximize the harvested power at ambient weather changes in irradiance and

temperature. However, the available MPPTs may fail to distinguish between multiple peaks while the PV system experiences partial shading conditions. If the initial point of MPP is not located close to the GMPP, the conventional MPPT will track one of the local peaks, LMPP. Thus, most of the classical MPPT approaches need to jump out of the current MPP and explore the entire search space frequently to ensure harvesting as much power as possible and prevent any power loss due to partial shading.

In recent years, many techniques have been proposed for MPPT under partial shading [26, 29, 67-82]. Two methods are basically used to decrease shading side effects: either hardware-based or software-based. The hardware-based method needs extra measurements and a different configuration [68, 69, 82]. It may include dynamic reconfiguration, distributed architecture or an equalizer. The dynamic reconfiguration of PV modules is designed based on the shading patterns. It may add more measurements. For example, in [19], a global search is designed based on two strategies; however, the second strategy is more expensive since it necessitates an additional current sensor at each bypass diode. Furthermore, [23] introduces a mathematical formulation for the optimal reconfiguration of PV arrays. It formulates the reconfiguration problem as a mixed integer quadratic programming issue and searches for the optimal solution using a branch and bound algorithm. In [83], the plan comprises two compensations for modules and strings. Each module is connected in parallel with a current-compensating converter, and each string is connected in a series with a voltage-compensating converter.

In distributed architecture, each panel is individually connected to a single controller assigned for each module. These hardware-based methods can resolve the problem, since the P-V characteristic of a module (with just one bypass diode) always has a single peak. These methods,

however, are expensive and require many more devices compared to software-based algorithms.

On the other hand, the equalizer is effectively implemented to guarantee the same voltage generated in case of partial shading. For example, in [30], the two-switch voltage equalizer uses an LLC resonant inverter and voltage multiplier. However, the aforementioned techniques are clearly complicated and expensive. Therefore, the software-based methods are more cost effective and are based on algorithms that can track the GMPP via developing sophisticated control algorithms. For instance, the artificial neural network technique has been used for global search, but it depends on the accuracy of given data for training. All different conditions need to be included, and ANN must be retrained if the PV strings will likely be extended. The particle swarm optimization, or PSO approach, has also been efficiently used in [7]. However, the method contains many parameters, and the implementation is very complicated commercially. In [84], the authors use a modified particle velocity-based particle swarm optimization technique for global maximum power point tracking of PV arrays under partial shading conditions. Likewise, grey wolf optimization technique, chaotic search modified fireflies, and genetic algorithms are applied in PV partially shaded applications. In [79], the MPPT algorithm based on colony of fireflies was also applied for PV arrays under partial shade.

The tracking procedure consists of positioning (locating) the fireflies in the possible solution space, and based on the PV power output, the flies move to defined regions. However, these techniques share the complexity and similarities of evolutionary computations. They further encounters sudden and random fluctuations, which result in poor dynamic performance. In [28], a two stage MPPT control method is proposed to realize a relatively simple control system that can track the real maximum power point even under non-uniform insolation conditions.

Moreover, [27] presents maximum power trapezium where the P-V plane contains all possible GMPPs for any partial shading. The global MPPT algorithm is proposed by using the maximum power trapezium and information about the minimum voltage difference between adjacent local peaks. Another approach is based on hill claiming. It measures PV current to map out the solar irradiance pattern. It then selects suitable points for tracking the local points. Next, it applies hill claiming in these points and tracks all the local points. Finally, by comparing the acquired local points, it selects the global maximum point.

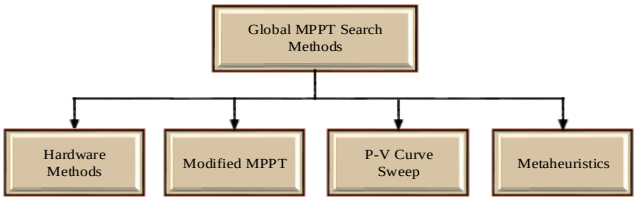

Figure 2.2: Classification of global MPPT search methods

Figure 2.2 classifies the methods into four groups that can typically limit partial shading consequences. Essentially, micro converters or module-integrated converters is the simplest approach to distinguish GMPP independently on every single module, when there will be only one maxima. However, this approach is too expensive, especially in huge PV systems. The approach also requires individual control, making remote control complicated.

2.3 Current Sensorless Methods

A lot of research has been proposed to achieve the current sensorless mode based on several concepts and techniques. The current sensorless mode intends to substitute for the existing current sensor by creating the same current sensor measurements with an acceptable compromise between accuracy and cost effectiveness. Certainly, most of introduced models are used in the area of maximum power point tracking. In fact, current sensors are typically bulky, expensive and the

highest point of failure in reliability and accuracy. Additionally, the cost is considerable when PV solar systems contain huge number of PV arrays, and each MPP tracker will need a single current sensor. Therefore, [86] introduces an effective approach of sensorless current mode to avoid including a current sensor. The approach uses an observer-based model as a surrogate to the current signal. However, as seen in [87] and [88], both approaches exploit the ripples of capacitor current to estimate the current. In [89], the research uses a transcendental PV cell relations and single voltage sensor to determine the maximum power point. In [90], the plan uses power estimation based on the switching information of a hysteresis voltage regulator. Moreover, the current sensorless is used for voltage control of a DC/DC converter in discontinuous conduction mode using the charge balance principle and current error compensation as in [91]. Finally, [92] presents a flyback converter with current sensorless mode. The converter current analysis and resistive load observer model are obtained and evaluated to eliminate the current sensor using model predictive control.

2.4 Balancing PV Grid-Tied System Using a CHB Inverter

Three classical topologies of multilevel converters were introduced in industry. Flying capacitor, neutral point clamped (diode clamped), and cascaded H-bridge inverter have been presented in studies [93-101]. A cascaded H-bridge converter, or CHB, is built from a number of cells that are mainly single-phase inverters connected in a series [102-104]. CHB topology is more suitable for a PV grid-tied system. It offers a unique option in which each CHB cell has a PV source, i.e., they function independently. This topology reduces the voltage stress on each switch due to multiple levels and any faulty switch can be effectively tolerated and successfully addressed without turning off the entire system [85]. CHB also shows improvement in quality and efficiency,

and has become an ideal in large scale PV applications [105]. Nevertheless, CHB can increase the number of voltage levels and reduce total harmonic distortion (THD). To date, almost all the research performed on multilevel or multicell converters applications is concentrated on internal fault tolerance due to the large number of semiconductors power switches [106-117]. Therefore, reliability has become a very important criterion since any faulty power cells in the cascaded H-bridge converter will promote instability and potential power losses [112, 118].

Indeed, CHB multilevel converter topology presents several advantages during abnormal conditions in PV systems, including internal faults, severe partial shading, and temperature inhomogeneity. Such conditions could lead to the entire PV distributed generation system to quit unexpectedly as a result of generating unbalanced three phase waveforms. In fact, the arrays can be assembled on a number of levels using a CHB converter. The CHB can recover the quality of line to line output voltage waveforms even during unequal generation of phase voltages. Consequently, CHB converters can impose system balancing strategies that increase the number of line to line voltage levels with a smaller number of one phase utilized cells. The strategies are achievable since the cascaded multicell converter is constructed based on a series connection of multiple cells [93, 119].

Earlier research tried to compensate for the unbalanced three phase voltages due to a fault by changing the output phase shift angles to new pre-calculated angles based on the number of faulty levels. In [108], the authors successfully avoid switches states i.e., no longer available due to the faulty cell using the redundant of states. In [85], the authors introduced a new compensation technique that can locate the inverter and load neutral points and then use the optimum angles and modulation indexes in order to obtain the maximum balanced load voltages. Another approach

skips one or more damaged power cells through additional switches to bypass the faulty cell and control the phase shift angle in the carrier signals in the power circuit and then modifies the modulation strategy in addition to adjusting the reference signals of the pulse width-modulation to the modulator to increase the output voltage and maintain the generation of balanced voltages at the load side [114].

2.5 Grid Power Injection Strategies

Grids contain numerous reactive power resources. Synchronous generators, overexcited synchronous motors and flexible AC transmission systems (FACTS) are the most common controllable reactive power sources. In the IEEE 1547 published on 2003, injected reactive power by PV systems in low voltage grids was prohibited [120-122]. However, in 2014, new IEEE standard regulations determined strategies to supply reactive power for grid power quality enhancement using PV grid-tied systems [123]. Further, it allowed ancillary services to be provided by the PV grid-connected systems to support the utility grid stability for basic active power delivery.

In different literature, many reactive power control strategies for a PV connected to a single-phase inverter have been proposed [124, 125]. A 1-kW single-phase grid-connected system in a low-voltage ride-through related to reactive current injection and voltage support through reactive power control was introduced in [126]. In [121], the research presents a decentralized control scheme for controlling active and reactive power of PV grid-tied AC-stacked PV inverter architecture using single member phase compensation. The decentralized control scheme allows for a fully distributed architecture, both in terms of active and reactive power control and in physical implementation of a PV system. Moreover, [127] proposes a decentralized nonlinear auto-

adaptive controller for reducing system losses by the optimal management of the reactive power supplied by the inverters of PV units. The control design is based on an optimization procedure involving the sensitivity theory in conjunction with the Lyapunov function to provide control laws acting as references of the PV inverter local controller. A PV inverter will operate in a decoupled manner to provide the reactive power imposed by the control law and to transfer the active power produced by PV modules. Furthermore, in [128], a compensation strategy combining reactive power compensation with a novel modulation method is proposed to extend the operating range in terms of module mismatch. [129]

2.6 Modulation Strategies of Multilevel Converters

Figure 2.3 shows the classification of multilevel modulation techniques [119, 130]. However, the space vector modulation, or SVM, is efficiently used whether in classical or multilevel three-phase voltage source inverters. The switching frequency criteria can further subdivide multilevel modulations into three classes: fundamental, mixed, and high switching frequency.

The fundamental switching is also known as a “selective harmonic elimination” or “programmed modulation,” and the optimization computation is done offline on a more powerful computer. The result of the calculation is a set of switching angles in function of the modulation index m, to be stored in memory (ROM, EPROM) of the PWM controller. However, as the output frequency decreases, a number of pulses also must decrease in order to keep switching frequency low. In space vector control (SVC), voltage reference and average value will not be equal, creating an error that remains uncompensated, and the error made decreases as the number of levels increases [131]. Figure 2.3 also shows zones nearest to one of the vertices defined by the medians.

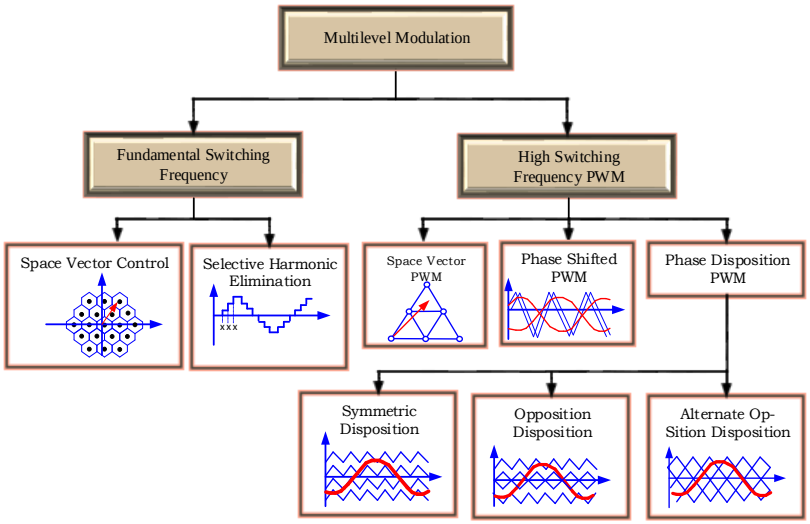

Figure 2.3: Classification of multilevel modulation

These medians of all grid triangles create hexagonal mesh centered in each vertex and determine the sets of points closest to each generable vector. Therefore, the aim of the modulation is to choose among all the generable vectors the one that minimizes the error. If the reference vector is rotating at a constant angular speed, the output voltage will have a symmetrical staircase waveform, and switches will commutate at the fundamental (low) frequency. The adopted and selected strategy in this dissertation is space vector modulation (SVM). SVM implementation starts by detecting the reference vector in which the sector is located by using the voltage magnitude and angle and then determining the three nearest voltage space vectors. After that, the SVM strategy calculates the switching time duration of voltage space vectors, and finally selects the optimized switching sequence, i.e., exactly matching the vector in three phases.

Based on the literature review provided in this chapter, the desirable properties of the MPPT and the possibility of partial shading incidents necessitate an efficient and inexpensive technique in which all challenges can be effectively addressed using high quality underlying algorithms for standalone PV systems or PV grid-tied systems

Chapter 3

In this chapter, the mathematical models of three DC/DC converters are derived and then the dynamic performance is evaluated as well. Following, a brief theory introduces the principles of model predictive control (MPC). Next is the implementation steps of MPC strategy on the proposed maximum power point tracking method. Then the chapter describes global search techniques during partial shading. After that, the chapter clarifies the introduced flowchart to detect the global power peak while the modules experience mismatch scenarios. The algorithm can successfully address and show the necessity of global search in MPPT control. In addition, Chapter 3 introduces a new current sensorless model to replace the existing current sensor. This chapter also presents a balanced control strategy for a cascaded H-bridge (CHB) multilevel inverter with three-phase connecting to the grid side and PV arrays connected to DC/DC converter from the other side. Furthermore, the strategy of phase shift compensation is used along with balanced model through a new control topology of CHB converter to overcome imbalances in three phase voltage and address the voltage generation mismatch due to severe shading. Moreover, the strategy applies a reactive power injection control model which result in the desired power factor and freely control the injected reactive power.

3.1 Derive and evaluate three DC/DC converters performance

The proposed system has DC/DC power converter that will be responsible for extracting the maximum power from PV string, thus studying dynamic performance becomes necessary and so important. Three selected DC/DC power converters will be evaluated in terms of transient behavior and will include dynamic performance analysis. The converters are analyzed in continuous conduction mode during two switching states where the switches are either turned ON or OFF. To perform the analysis, first the transfer function of each converter is obtained and then apply five operating point that represents each region in I-V characteristic curve as shown in figure 1.9.

3.1.1 Flyback Converter:

Flyback is one of DC/DC converters that is widely used in different power electronics applications. It is used in AC/DC conversion as well. This converter is galvanically isolating the input from the outputs. Flyback is considered a buck-boost converter, but its inductor was divided to form a transformer. Therefore, additional added feature includes multiple voltage ratio and insolation. Figure 3.1 illustrates flyback circuit schematic

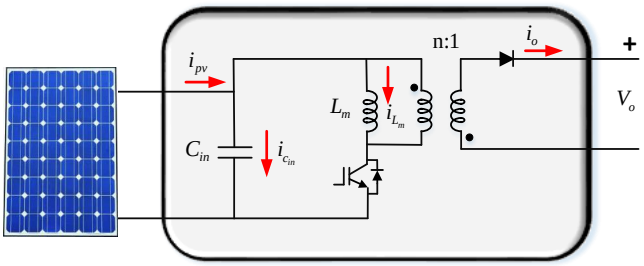

Figure 3.1: Flyback converter schematic connected to PV panel

First, in mode (1), in case of switch is ON and diode is OFF, and form Kirchhoff Voltage law (KVL):

$$V_{L_m} = L_m \frac{di_{L_m}}{dt} = V_{c_{in}} \tag{3.1}$$

$$i_{C_{in}} = C_{in} \frac{dv_{C_{in}}}{dt} = \frac{V_{eq} - V_{C_{in}}}{R_{eq}} - i_{L_m} \tag{3.2}$$

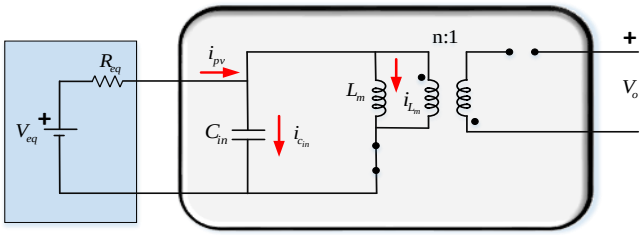

Figure 3.2: Flyback converter when the switch is ON, and diode is OFF

In mode (2), in case of switch is OFF and diode is ON, and by using KVL:

$$V_{L_m} = L_m \frac{di_{L_m}}{dt} = -nV_o \tag{3.3}$$

$$i_{C_{in}} = C_{in} \frac{dv_{C_{in}}}{dt} = \frac{V_{eq} - V_{C_{in}}}{R_{eq}} \tag{3.4}$$

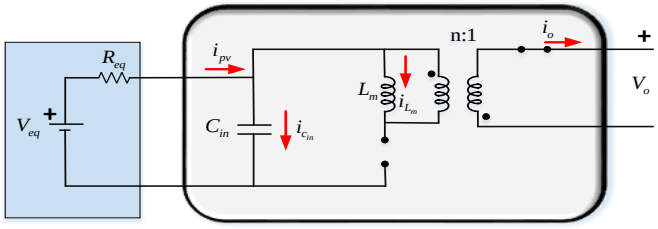

Figure 3.3: Flyback converter when the switch is OFF, and diode is ON

Flyback duty cycle (D) and voltage transfer ratio is given by:

$$D = \frac{nV_o}{nV_o + V_{in}} \tag{3.5}$$

Thus, by averaging both modes equations and linearizing them, the equations can be rewritten:

$$L_m \frac{di_{L_m}}{dt} = DV_{c_{in}} - (1-D)nV_o \tag{3.6}$$

$$C_{in} \frac{dv_{c_{in}}}{dt} = \frac{V_{eq} - V_{in}}{R_{eq}} - Di_{L_m} \tag{3.7}$$

The equations (3.6) and (3.7) in state space form are given as following:

$$\frac{di_{L_m}}{dt} = \frac{1}{L_m} DV_{c_{in}} - \frac{1}{L_m}(1-D)nV_o \tag{3.8}$$

$$\frac{dv_{c_{in}}}{dt} = \frac{1}{C_{in}} \frac{V_{eq} - V_{in}}{R_{eq}} - \frac{1}{C_{in}} Di_{L_m} \tag{3.9}$$

The state space matrixes A, B, and matrix C can be written in this form:

$$A = \begin{bmatrix} 0 & \frac{D}{L_m} \\ -\frac{D}{C_{in}} & -\frac{1}{R_{eq}C_{in}} \end{bmatrix}, \; B = \begin{bmatrix} \frac{V_{C_{in}} + nV_o}{L_m} \\ -\frac{I_{L_m}}{C_{in}} \end{bmatrix}, C = \begin{bmatrix} 1 & 0 \\ 0 & 1 \end{bmatrix}$$

The state space transfer function model is found by using the following formula:

$$H(s) = C(SI - A)^{-1} B \tag{3.10}$$

Therefore, flyback transfer function shows the effect of duty cycle on input voltage is given by:

$$H(s) = \frac{V_{c_{in}}(s)}{D(s)} = \frac{-I_{L_m} L_m R_{eq} s - DR_{eq} V_{c_{in}} - nDR_{eq} V_o}{L_m R_{eq} C_{in} s^2 + L_m s + R_{eq} D^2} \tag{3.11}$$

3.1.2 SEPIC Converter:

Figure 3.4 shows one of DC/DC converters known as **S**ingle-Ended Primary-Inductor Converter

or (SEPIC). This DC/DC converter is very common and typically used in special applications where output voltage is significantly higher than the input voltage.

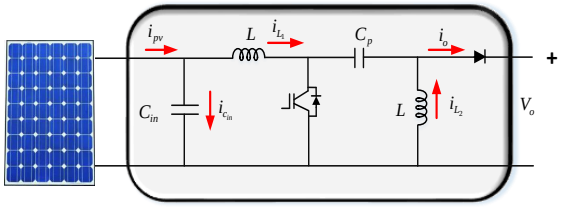

Figure 3.4: SEPIC converter circuit schematic connected to PV panel

In mode (1), in case of switch is ON and diode is OFF, and form Kirchhoff's voltage law

$$V_{L_1} = L_1 \frac{di_{L_1}}{dt} = V_{c_{in}} \tag{3.12}$$

$$V_{L_2} = L_2 \frac{di_{L_2}}{dt} = V_{c_p} \tag{3.13}$$

$$i_{c_{in}} = C_{in} \frac{dv_{c_{in}}}{dt} = \frac{V_{eq}}{R_{eq}} - \frac{V_{c_{in}}}{R_{eq}} - i_{L_1} \tag{3.14}$$

$$i_{c_p} = C_p \frac{dv_{c_p}}{dt} = -i_{L_2} \tag{3.15}$$

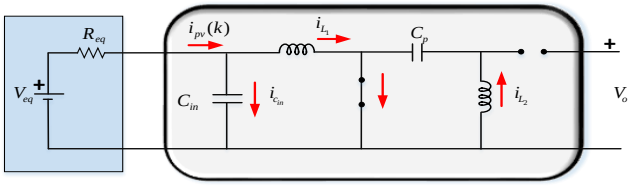

Figure 3.5: SEPIC converter, when the switch is ON, and diode is OFF

In mode (2), the switch is OFF, and diode is ON, and also by using Kirchhoff's voltage law,

$$L_1 \frac{di_{L_1}}{dt} = V_{in} - V_{C_p} - V_o \tag{3.16}$$

$$L_2 \frac{di_{L_2}}{dt} = -V_o \tag{3.17}$$

$$C_{in} \frac{dv_{C_{in}}}{dt} = \frac{V_{eq}}{R_{eq}} - \frac{V_{in}}{R_{eq}} - i_{L_1} \tag{3.18}$$

$$C_p \frac{dv_{C_p}}{dt} = -i_{L_1} \tag{3.19}$$

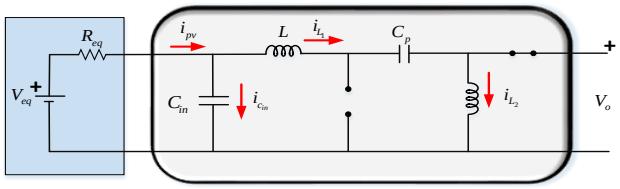

Figure 3.6: SEPIC converter, when the switch is OFF, and diode is ON

SEPIC duty cycle and voltage transfer ratio are given by:

$$D = \frac{V_o}{V_o + V_{in}} \tag{3.20}$$

Hence, the averaging equations in both modes and after linearizing can be written as following:

$$L_1 \frac{di_{L_1}}{dt} = V_{in} - (1-D)V_{C_p} - (1-D)V_o \tag{3.21}$$

$$L_2 \frac{di_{L_2}}{dt} = DV_{C_p} - (1-D)V_o \tag{3.22}$$

$$C_{in} \frac{di_{C_{in}}}{dt} = \frac{V_{eq}}{R_{eq}} - \frac{V_{in}}{R_{eq}} - i_{L_1} \tag{3.23}$$

$$C_p \frac{dv_{C_p}}{dt} = -i_{L_2} d + i_{L_1} (1-D) \tag{3.24}$$

Therefore, state space matrixes A, B, and matrix C can be written in this form:

$$A = \begin{bmatrix} 0 & 0 & \frac{1}{L_1} & -\frac{(1-D)}{L_1} \\ 0 & 0 & 0 & \frac{D}{L_2} \\ -\frac{1}{C_{in}} & 0 & -\frac{1}{R_{eq} C_{in}} & 0 \\ \frac{(1-D)}{C_p} & -\frac{D}{C_p} & 0 & 0 \end{bmatrix}, \; B = \begin{bmatrix} \frac{V_{C_p} + V_o}{L_1} \\ \frac{V_{C_p} + V}{L_2} \\ \frac{-I_{L_2} - I_{L_1}}{C_p} \end{bmatrix}, \; C = \begin{bmatrix} 1 & 0 & 0 & 0 \\ 0 & 1 & 0 & 0 \\ 0 & 0 & 1 & 0 \\ 0 & 0 & 0 & 1 \end{bmatrix}$$

Also, the state space transfer function model can be found by using formula (3.10):

$$H(s) = \frac{V_{C_{in}}(s)}{D(s)} = \frac{\left(-C_p L_2 R_{eq} V_{C_p} - C_p L_2 R_{eq} V_o\right) s^2 + \left(D I_{L_1} L_2 R_{eq} - I_{L_2} L_2 R_{eq} - I_{L_1} L_2 R_{eq} + D I_{L_2} L_2 R_{eq}\right) s - D R_{eq} V_{C_p} - D R_{eq} V_o}{C_{in} C_p L_1 L_2 R_{eq} s^4 + C_p L_1 L_2 s^3 + C_p L_2 R_{eq} + C_{in} L_2 R_{eq} - 2 C_{in} D L_2 R_{eq} + C_{in} D^2 L_1 R_{eq} + C_{in} D^2 L_2 R_{eq}) s^2 + (L_2 + D^2 L_1 + D^2 L_2 - 2 D L_2) s + D^2 R_{eq}}$$

3.1.3 Positive Buck Boost Converter:

This converter is also known as non-inverting DC/DC converter, and it combine the features of two converters, buck and boost. Thus, the converter has the capability transition from buck to boost and vice versa. Figure 3.7 shows the structure of the Positive Buck-Boost converter.

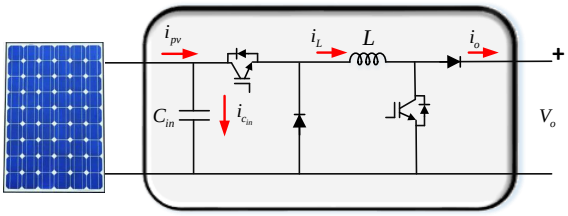

Figure 3.7: Positive buck boost circuit schematic connected to PV module

In case of two switches are ON and the two diodes are OFF, the equations according to

Kirchhoff's voltage law are:

$$L\frac{di_L}{dt} = V_{in} \tag{3.25}$$

$$C_{in}\frac{dv_{C_{in}}}{dt} = \frac{V_{eq} - V_{in}}{R_{eq}} - i_L \tag{3.26}$$

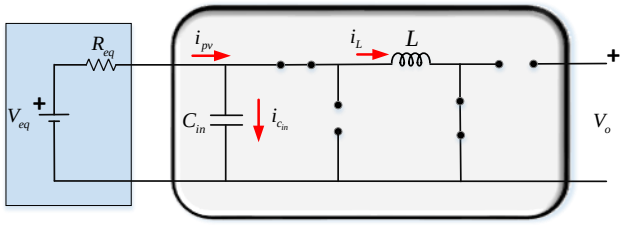

Figure 3.8: The converter when both switches are ON, and both diodes are OFF

However, when switches are both OFF and both diodes are ON the questions are:

$$L\frac{di_L}{dt} = -V_o \tag{3.27}$$

$$C_{in}\frac{dv_{C_{in}}}{dt} = \frac{V_{eq} - V_{in}}{R_{eq}} \tag{3.28}$$

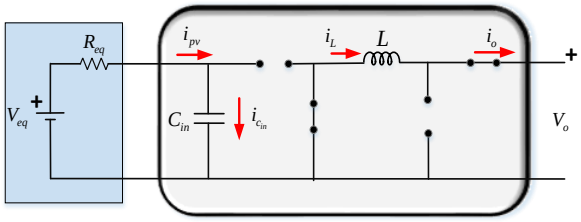

Figure 3.9: The converter when the switches are OFF, and diodes are ON

The voltage transfer ratio and duty cycle of positive buck boost converter is given by:

$$D = \frac{V_o}{V_o + V_{in}} \tag{3.29}$$

Next, after averaging and linearizing the questions are as shown:

$$L\frac{di_L}{dt} = DV_{in} - (1-D)V_o \tag{3.30}$$

$$C_{in}\frac{dv_{C_{in}}}{dt} = \frac{V_{eq} - V_{in}}{R_{eq}} - Di_L \tag{3.31}$$

Therefore, state space matrixes A, B, and matrix C can be written in this form:

$$A = \begin{bmatrix} 0 & \frac{D}{L} \\ -\frac{D}{C_{in}} & -\frac{1}{R_{eq}C_{in}} \end{bmatrix},\quad B = \begin{bmatrix} \frac{V_{in}+V_o}{L} \\ -\frac{I_L}{C_{in}} \end{bmatrix},\quad C = \begin{bmatrix} 1 & 0 \\ 0 & 1 \end{bmatrix}$$

Also, the state space transfer function model can be found by using formula (3.10):

$$H(s) = \frac{V_{C_{in}}(s)}{D(s)} = -\frac{R_{eq}D\left(V_{C_{in}} + V_o\right) - R_{eq}I_L D}{LC_{in}R_{eq}s^2 + Ls + R_{eq}D^2} \tag{3.32}$$

The dynamic performance of the three power converters is studied and stimulatingly verified in five regions illustrated in Figure 1.3. The analysis can be achieved by selecting one operating point within each region. Table 3.1 gives characteristics details for each operation point that reflects the principle of each region.

Table 3.1: Five Operating points on the I-V curve of PV module

Operating Points Characteristics	Operating Point [1]	Operating point [2]	Operating point [3]	Operating point [4]	Operating point [5]
PV voltage [V]	10.013	15.51	17.6	18.5	20.5
Dynamic Resistance [Ω]	-776	-19.652	-4.35	-2.78	-0.99
PV Power [W]	39.9	60.8	65.0	63.8	45.1

The results of each converter are provided and discussed in Chapter 4. The response is accurately described the dynamic behavior of the three-designated converters and therefore positive buck-boost is chosen to utilize the new adaptive energy harvesting and PV grid-tied system.

3.2 The Proposed Adaptive Energy Harvesting Based on MPC

This section introduces a reliable and efficient control strategy for PV applications. In fact, designing and developing an efficient MPPT method is reasonable in terms of cost effectiveness and efficiency compared to improving other system components. For instance, DC/DC converters have an efficiency range between 92-98% [132] while 15-25% is the efficiency of the common PV module, which therefore is a target of manufacturing innovation and tracking techniques development [133]. The aim of this section is to significantly improve the MPPT dynamic tracking performance for the PV systems to reach the highest available power by introducing a new adaptive maximum power harvesting technique based on model predictive control and achieve efficacy target of 100%. The proposed technique assures further tracking accuracy, fast convergence, less fluctuation, constant DC voltage link, and a reduction in complexity, which leads to faster responses and improves the tracking efficacy.

The method implements a finite set of model predictive controls, which are suited to optimize operation control and include a feature of predicting future behavior of the PV system. Several sampling steps in the time horizon illustrated in Figure 3.10 are used to predict the future behavior along with the system model. The steps will be selected based on a set of possible control actuation. The algorithm decides on the optimal next control actuation based on references and predicted next values that minimize a desired cost function. While two predicted states are computed, one is sent to the process and the other is rejected based on cost function evaluation.

Note, the introduced scheme is designed to predict the system behavior one step ahead to the next sampling interval $(k+1)$. However, other applications may use more steps, so the predictive abilities depend on the application and performance requirements.

The optimization problem is solved at every sample time (k+1), and a new sequence of optimal actuation is obtained. The system states are periodically predicted by using a new set of measured data $V_{pv}(k)$ and $V_{dc\_link}(k)$ in the discrete model. Once the horizon is shifted by one step further, another optimization will be used. Figure 3.10 shows a horizon with length of 3 (N = 3). The horizon considers the minimization of the cost function. It keeps moving forward while the k sample increases [134]. An open-loop optimal control scheme makes use of the optimum open-loop initial decision at each stage, and then incorporates feedback in the observation of the obtained actual state [135].

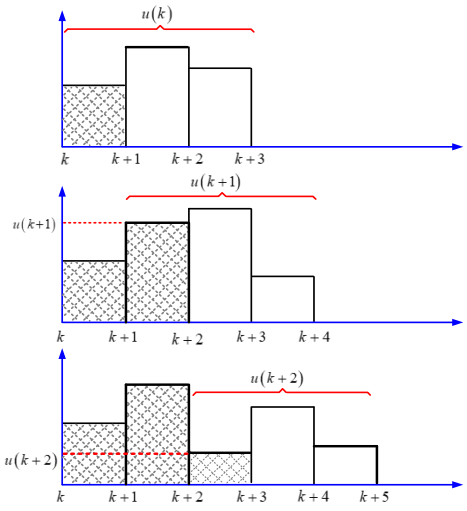

Figure 3.10: Moving horizon optimization [92]

The MPC scheme shown in Figure 3.11 determines the optimal actuation by using the system model in an open loop and uses the feedback measurements to adjust the system accordingly. Thus, MPC amounts to an open-loop-optimal feedback control methodology. The

predicted system control response is used to determine the optimal next switching state by minimizing a cost function that considers the two future states and the reference signal received from MPPT. The discrete time model of the control variables used for prediction can be presented as a state-space model. The optimization problem is solved at every sample time, and a new sequence of optimal actuation is obtained by using a new set of measured data. The general scheme of MPC for power electronics converters is illustrated in Figure 3.11.

Both measured values in the block diagram are used in the discrete model to provide two possible variables. On the other hand, the MPPT block generates the reference value and evaluates the cost function by comparing the two possible values with the reference. Finally, an appropriate switching state is selected and applied to the positive buck-boost converter to enforce the PV modules to generate the maximum DC power. The primary use of model predictive control here is to track the system toward the maximum power point and then stabilize the operating point around MPP; therefore, the controlled outputs should follow a reference trajectory as closely as possible.

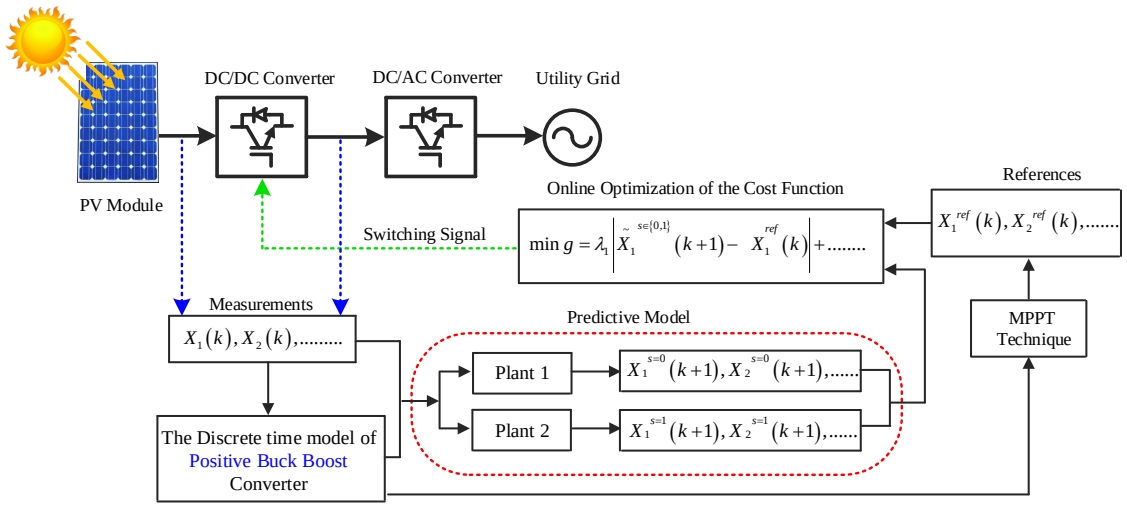

Figure 3.11: The introduced MPC scheme for the proposed PV grid-connected system.

If the proposed PV grid connected system implements model-based predictive control principle, it will eliminate the PI controller as well. The integral action of PI tends to increase the oscillatory or rolling behavior of the PV and can neither predict the future errors of the system nor decrease rise time. However, it only assists in minimizing the steady state error. Figure 3.11 illustrates the principle of introduced model predictive block diagram scheme of the proposed maximum power harvesting system. As depicted, the proposed new maximum energy harvesting is implemented to the DC/DC conversion stage and uses a prediction model of selected converters to find the reference power and then apply cost function under the subject of minimization. The introduced model only uses two voltage sensors, PV input voltage and DC link voltage sensor. The scheme will predict the error of a predicted sample time. Based on optimization of the cost function *g*, the switching sequence will be generated. The scheme controls a positive buck-boost converter to harvest the maximum DC power that would be available at any time in each connected PV module. Therefore, the algorithm observes the changes and then takes appropriate and highly efficient action. Figure 3.12 demonstrates the topology of the PV grid connected system with the proposed model predictive control scheme-based energy extracting algorithm, which executes in multiple stages. The following steps clearly describe the procedure.

First, at any given sampling time k during the normal operation, the converter is commanded to draw the maximum possible power while increasing or decreasing the PV voltage $V_{pv}(k)$ based on the switching states. Two possible values for the future PV voltage $V_{pv}(k+1)$ at sample time $k+1$ are continuously generated by the proposed approach. Thus, in the first step, the algorithm calculates the two-possible PV voltage values,

$$V_{pv}^{S=1}(k+1) = V_{pv}(k) + \frac{T_s}{C_{dc\_link}} \frac{\overset{*}{P}_{qd}(k)}{V_{pv}(k)} \tag{3.33}$$

$$V_{pv}(k+1)^{S=0} = V_{pv}(k) + \frac{T_s(1-D)}{C_{dc\_link}} i_{pv}(k) + \frac{T_s}{C_{dc\_link}} \left[\frac{\overset{*}{P}_{qd}(k)}{V_{dc\_link}(k)} \right] \left(\frac{V_{pv}(k)}{V_{dc\_link}(k)} \right) \tag{3.34}$$

Second, the algorithm computes the power that is expected to be drawn from the PV modules based on the PV voltage found in (step 1) that basically has two predicted values. The power can also be shifted to either of the two possible values, $P_{pv}^{S=1}(k+1)$ or $P_{pv}^{S=0}(k+1)$ Frequently, at each sampling time, the algorithm necessitates the knowledge of the P-V characteristic around the current measurement of the $V_{pv}(k)$ besides $V_{dc\_link}(k)$ to predict the generated power. The digital observer shown in Figure 3.12 models the PV modules in a form of Thevenin equivalent circuit as depicted in Chapter (1) Figure 1.8 (b). The elements of the circuit in Figure 1.8 (b), are the equivalent voltage $V_{eq}(k)$ and equivalent resistance $R_{eq}(k)$ of the PV module, and both are functions of the P-V characteristic of the PV module as depicted in chapter 1. They are also subject to local estimation by the digital observer. The estimator equations are as follows:

$$R_{eq}(k) = \left| -\frac{V_{pv}(k) - V_{pv}(k-1)}{I_{pv}(k) - I_{pv}(k-1)} \right| \tag{3.35}$$

$$V_{eq}(k) = V_{pv}(k) + R_{eq}(k) I_{pv}(k) \tag{3.36}$$

Where $V_{pv}(k-1)$ and $I_{pv}(k-1)$ are the values of the PV module voltage and current from the previous sampling time.

Estimating the equivalent resistance and voltage of the PV module, the two possible values for the generated power in the next sampling time can be easily predicted from

$$P_{pv}^{S=1}(k+1) = V_{pv}^{S=1}(k+1) \times I_{pv}^{S=1}(k+1) \tag{3.37}$$

where

$$I_{pv}^{S=1}(k+1) = \frac{V_{eq}(k) - V_{pv}^{S=1}(k+1)}{R_{eq}(k)} \tag{3.38}$$

and likewise, the $P_{pv}^{S=0}(k+1)$ is given by:

$$P_{pv}^{S=0}(k+1) = V_{pv}^{S=0}(k+1) \times I_{pv}^{S=0}(k+1) \tag{3.39}$$

where

$$I_{pv}^{S=0}(k+1) = \frac{V_{eq}(k) - V_{pv}^{S=0}(k+1)}{R_{eq}(k)} \tag{3.40}$$

After the algorithm calculates the two predicted powers, it computes the change in power.

$$\Delta P_{pv}^{S\in\{0,1\}}(k+1) = P_{pv}^{S=\{1\}}(k+1) - P_{pv}^{S=\{0\}}(k+1) \tag{3.41}$$

The approach checks whether global search conditions are met. If so, it will start searching on the global peak. Otherwise, it will continue implementing the new adaptive harvesting power point and search on the unique maximum power point.

Then the algorithm verifies the change in the predicted power, which can have three different scenarios. In the first scenario, when the change in power is greater than zero (based on the sign), the operating point should continue climbing up toward the maximum peak.

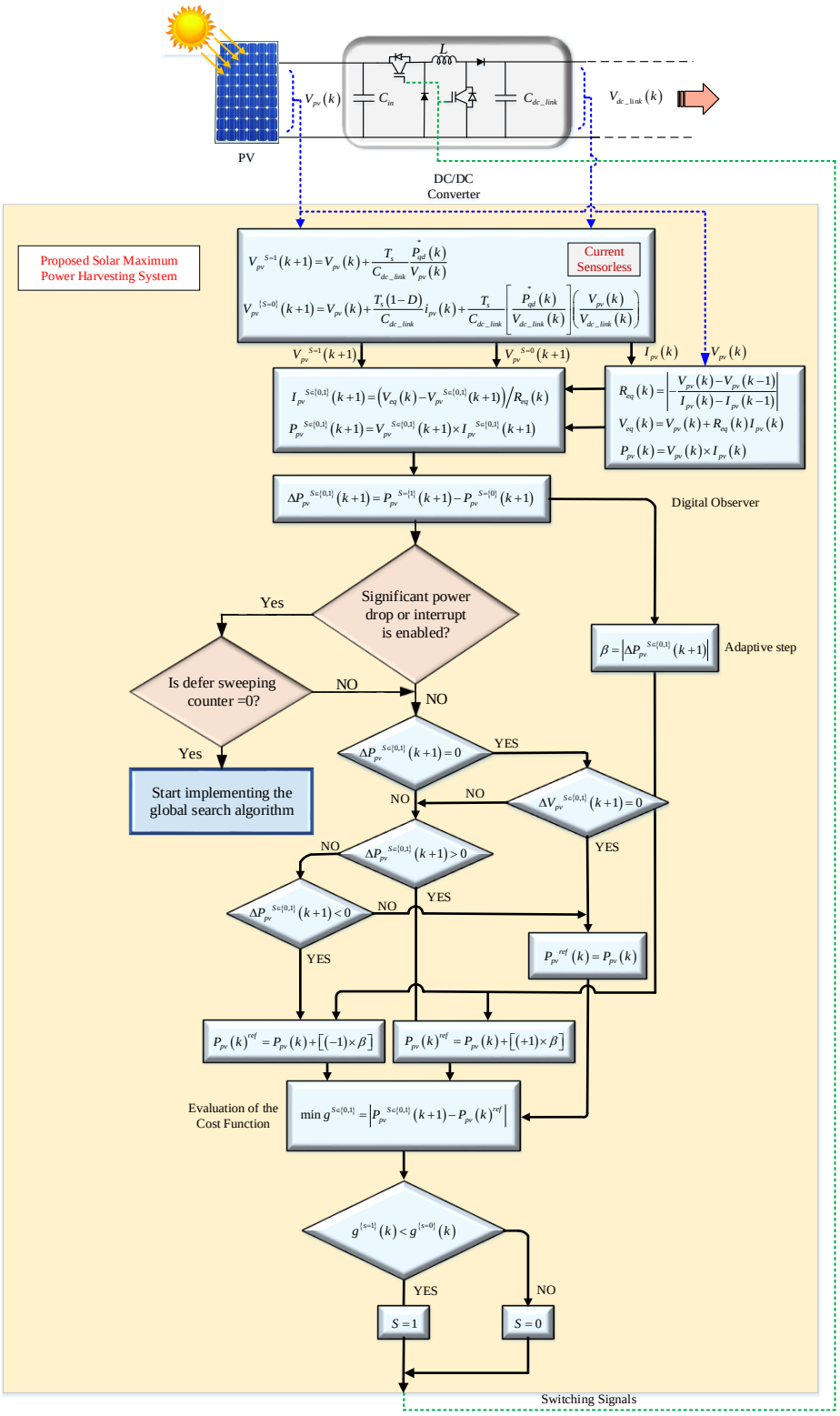

Figure 3.12: Block diagram of the proposed model predictive based maximum power peak tracking system

$$\Delta P_{pv}^{S\in\{0,1\}}(k+1) > 0 \tag{3.42}$$

$$P_{pv}(k)^{ref} = P_{pv}(k) + \left[(+1)\times\beta\right] \tag{3. 43}$$

The algorithm's decision will generate reference power equal to $P_{pv}(k)$ added to a positive adaptive factor.

The adaptive factor is a scale (β), a weighted factor that will be added to accelerate the performance response as needed. The value of β is frequently updated based on the predicted power, and it will reduce to improve the performance once the algorithm detects that the operating point is around the desired MPP.

$$\beta = \left|\Delta P_{pv}^{S=\{0,1\}}(k+1)\right| \tag{3. 44}$$

The second scenario, which occurs if the change in power is less than zero, means the targeted MPP has been passed, so the algorithm should force the operating point to move backward.

$$\Delta P_{pv}^{S\in\{0,1\}}(k+1) < 0 \tag{3. 45}$$

$$P_{pv}(k)^{ref} = P_{pv}(k) + \left[(-1)\times\beta\right] \tag{3. 46}$$

Therefore, the generated reference power will equal $P_{pv}(k)$ added to a negative adaptive coefficient. The last case, when the change in power is equal to zero, indicates that the operating point is exactly at the MPP, which can be confirmed if the change in the predicted voltage is equal to zero. Thus, the reference power is equal to $P_{pv}(k)$.

$$\Delta P_{pv}^{S\in\{0,1\}}(k+1)=0 \tag{3.47}$$

Here, the change in predicted input voltage is checked within the two switching states

$$\Delta V_{pv}^{S\in\{0,1\}}(k+1)=0 \tag{3.48}$$

$$P_{pv}^{ref}(k)=P_{pv}(k) \tag{3.49}$$

Third, now the two cases of the expected power are applied in the cost function. At each sampling time, the cost function is repeatedly evaluated by comparing it to the reference values. The optimization problem is then addressed again by using a new set of measured $V_{pv}(k)$ and $V_{dc\_link}(k)$ to generate a new sequence of optimal actuation by considering the design constraints. Finally, the selected optimal actuation $s\{0,1\}$ is applied to the converter.

The implemented form of the cost function here is $g\in\{0,1\}$, which is subject to minimization, and can be formulated as follows:

$$\min\ g^{S=\{0,1\}}=\left|P_{pv}^{S=\{0,1\}}(k+1)-P_{pv}^{ref}(k)\right| \tag{3.50}$$

Finally, to increase the power delivery in each step, the anticipated power, $P_{pv}^{\{S=1\}}(k+1)$ or $P_{pv}^{\{S=0\}}(k+1)$ that will increase the value of g in Equation (3.50), will be selected as the desirable trajectory for the next step. For example, in the case of $g^{\{S=1\}}>g^{\{S=0\}}$, the algorithm chooses to generate $V_{pv}^{S=1}(k+1)$ in the next sampling time, and as result, the PV voltage will be shifted to $V_{pv}^{S=1}(k+1)$ via the switching sequence. The generated sequence is interiorly adjusting the converter duty cycle to reach the desirable (target) value of the PV voltage. The optimal

solution is reached by the objective optimization approach. The proposed system has been tested and the results were verified with other maximum power point tracking techniques mentioned in Chapter 2. The comparison between the obtainable results in Chapter 4 is to confirm the robustness and excellent performance of the new harvesting strategy in terms of fast convergence, tracking accuracy, and efficacy.

3.3 Principles of the Introduced Global Search Strategy:

This section focuses on global search methods in the case of single or multiple PV modules operating under partially shaded conditions when the P-V characteristics curve exhibits multiple local maxima and one global peak. In such cases, locating the global peak requires an intelligent technique since finding the global peak becomes tricky due to the presence of multiple maxima.

One of the goals of this dissertation is to increase the captured power effectively. Therefore, new P-V characteristic sweeping strategy-based power is introduced and executed to distinguish the global peak under partial shading conditions. The introduced approach can instantly respond to recover the maximum power available from the presented PV system and sustain it at highest maximum output power delivery.

This section presents an example of a string that has ten PV modules, four of which are partially shaded. The simulation results of this section are presented and discussed in Chapter 4. Moreover, the proposed partial shading scenarios are time-variant to examine the intelligence and robustness of the introduced global search technique. Three different partial shading scenarios are applied, and the algorithm will frequently implement the global search to update the global peak since it assumes that shading is time-variant.

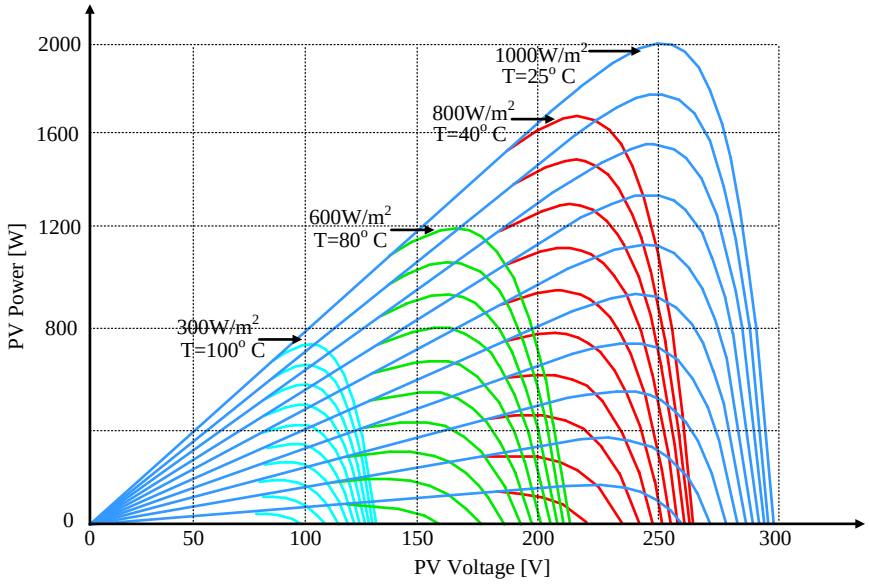

Figure 3.13: A string of PV modules under various insolation and temperatures

Figure 3.13 illustrates several P-V curves for a string under miscellaneous levels of irradiance and temperature. Figure 3.14 shows a global search flowchart of the proposed technique-based power. The method can successfully track PV systems under partial shading conditions and harness the maximum available power.

The new important feature of the introduced approach is perturbing the power. Therefore, any variation in voltage or current due to changes in illumination or temperature can be easily addressed. The other added feature, i.e., the main program, is designed to call the global search subroutine if one of the two different criteria is fulfilled.

In the first step, the algorithm notices a sudden change in the irradiance level due to partial shading that leads to a significant power drop and changes the recent operating point so that it no longer is the maximum power peak. Second, an interruption is scheduled. In such cases, the algorithm assumes that the global peak is located in the P-V curve plane, and it is randomly varied due to the variation of ambient weather changes. Thus, the introduced main program contains an

interruption that calls the global search subroutine program periodically to address any approaching variations and maintain the maximum power peak.

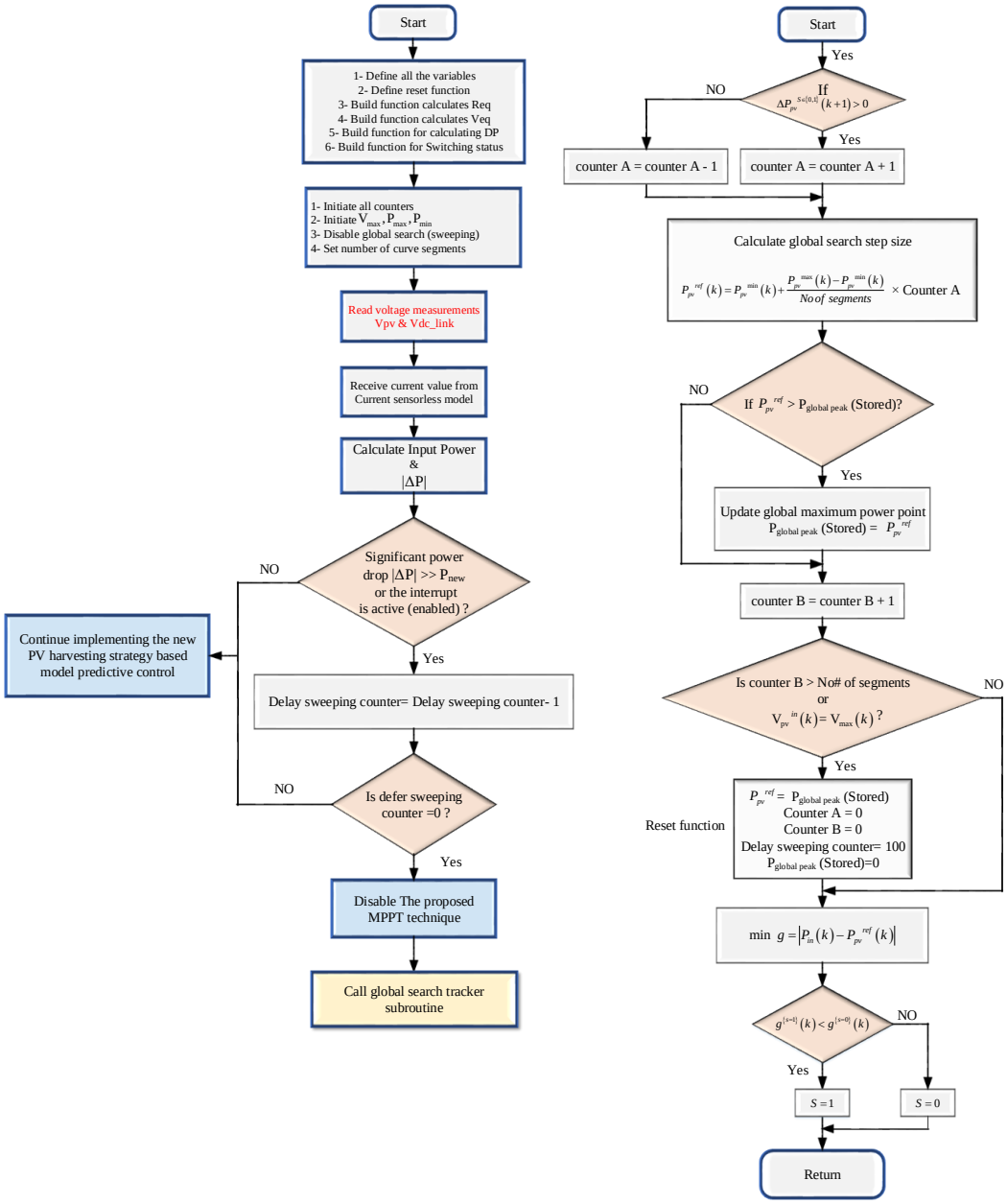

Figure 3.14: The proposed global search flowchart

If one of the aforementioned conditions is met, the algorithm checks the delay sweeping counter before it performs the global search. The delay sweeping counter was added to emphasize

the system's stability and ensure better performance consistency. It can postpone any necessary global search to allow some time for the system to stabilize between each scan and prevents instability or voltage swings. As a result, it prevents unnecessary fluctuation at the output and the counter stabilization value is basically chosen upon a required delay. The time delay between each scan can be also chosen based on the expected ambient changes. Once the delay counter is reset, the algorithm will disable the new MPPT harvesting strategy and call the global search subroutine.

For the second step, the subroutine checks the change in power. If it is greater than zero, the counter A will be incremented by 1 and the reference power steps up. Otherwise, counter A will be decremented by 1 and the reference power will step down. Hence, counter A controls the perturbation direction. If the change in power is still positive (greater than zero), the power step will continue climbing up to achieve the next power peak. Otherwise, counter A will decrease by one, which means a new peak was just reached and the scanning direction should flip down until the change in power becomes positive. The reference power equation is given by:

$$P_{pv}^{ref}(k) = P_{pv}^{\min} + \left(\frac{P_{pv}^{\max} - P_{pv}^{\min}}{No\#of\ segments} \times counter\ A \right) \tag{3.51}$$

where $P_{pv}^{\max}$ is the maximum possible power at normal conditions, and $P_{pv}^{\min}$ is a minimum sweeping start point and the operator has the option to change it based on minimum desired power. The number of segments indicates that the P-V characteristics curve is divided into specific number of segments (zones). The technique is set to continually begin from minimum reference power $P_{pv}^{ref} = P_{pv}^{\min}$. In this algorithm, the scanning start point is designed to launch the searching from 25% of the total output power $P_{\max}$ and stop at the final segment. Hence the sweeping can effectively go over the entire P-V plane and scan only within an operable defined range. For

example, if the minimum acceptable power delivery from the PV system is 500W, then the sweeping start point $P_{ref}^{\min}$ =500W could be the maximum available global peak. Likewise, the lower the value of sweeping start points, the more additional scanning area and time will be added. The power step is carefully computed in a given formula, and it gives the minimum possible displacement between the two successive peaks to ensure that no peak is missed or left during global tracking.

$$\Delta P_{pv}^{S\in\{0,1\}} >> \left[P_{pv}(k)\right]\beta \tag{3.52}$$

To call the global search subroutine even for a specific variation in power, the recent measured power can be multiplied by factor β.

On the third step, the algorithm checks whether the P_{pv}^{ref} is greater than P_{global_peak} (Stored), if so, the P_{global_peak} will be updated.

$$P_{pv}^{ref} > P_{global\_peak}(stored) \tag{3.53}$$

Therefore, during this process, if a higher peak is observed, it will be verified with the last stored peak and the larger value will be stored. Otherwise, counter B will be incremented by 1 and the algorithm will check if it is greater than the number of segments. If so, the global search will stop searching and the last P_{global_peak} is the new global peak; otherwise, the algorithm continues on the right-side and repeats step 1 and so on. The algorithm uses a cost function to decide on generating the switch pulses through global search.

This method is designated to overcome unexpected changes in insolation when the PV system experiences partial shading conditions. Otherwise, the operating point is going to be tracked to the nearest local power peak by the proposed MPPT method. Figure 3.15 displays two

different scenarios of partial shading and shows the global search tracking the global peak in multiple P-V characteristics curves.

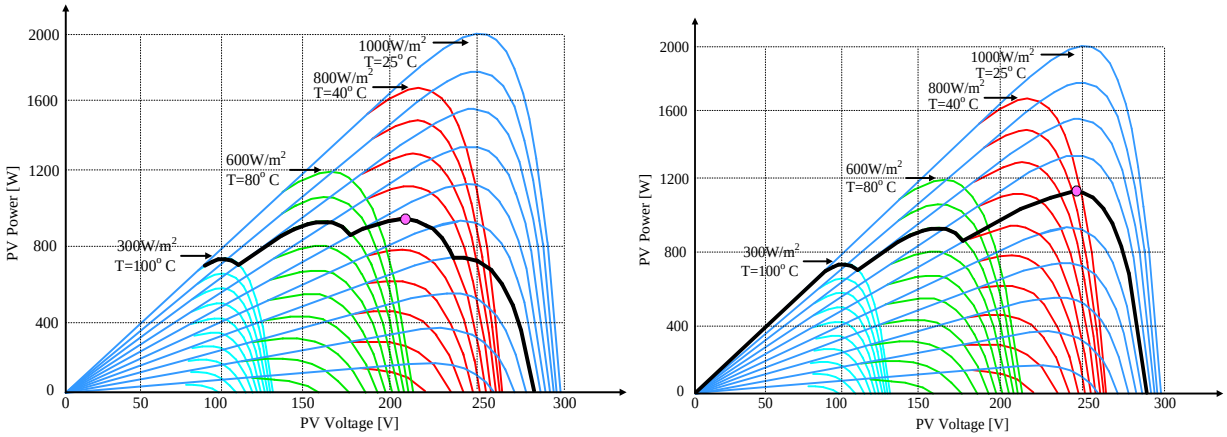

Figure 3.15: Two different scenarios of partial shading incidences on the P-V curve

In conclusion, the global search strategy is essential while the occurrence of partial shading (non-uniform insolation) is designed to alleviate the influence of complicated power reductions. As a result, it also acts as a monitor to improve the PV system performance and increase the power production. Before global search is active, the introduced PV system continually performs the new maximum power tracking method-based model predictive control (MPPT). Once power drop or change in power (ΔP) less than a certain amount or interruption becomes an active, the PV system is going to switch to global search. If either condition comes first, the global search will be launched and the other will be terminated and ignored to impose system stability. The interruption is regularly scheduled and accordingly as soon as it is enabled, the main program will stop implementing the new PV harvesting algorithm and call the global search subroutine. The global search tracking then starts searching and distinguishing the location of GMPP among the local maximum power peaks. Since the pattern of shading changes randomly throughout the daylight, the algorithm regularly repeats the global search to detect the accurate global power peak. In

Chapter 4, Figures 4.28 and 4.30 confirm that the proposed global search strategy successfully observes and effectively recovers the maximum power possible. The introduced new maximum power point method works together along with global search to maintain injecting maximum power that is available to the grid.

3.4 Current Sensorless Model Based on Model Predictive Control

One obstacle that limits the growth of PV systems is the high cost of infrastructure, and as a result, the generated power is more expensive than traditional sources. This section proposes a new PV current sensorless model to reduce the overall cost of installed PV systems while maintaining a high-performance improvement to tracking the maximum power harvesting. The introduced current sensorless is a mathematical control model based on model predictive control. It is introduced on the proposed PV grid connected system to substitute for the existing current sensor of positive buck-boost converter. This section and the results in Chapter 4 verify that the introduced model can effectively eliminate the PV current sensor, and therefore the goal of reducing the overall PV system's cost is achievable as well.

Moreover, the discrete model of positive buck-boost converter is analyzed using model predictive control to predict the PV current without the need for an expensive current sensor while reducing the number of measured signals. Consequently, only two voltage sensors are used that employ both the input PV voltage and DC link voltage through a predictive model and a power injection model. Figure 3.16 offers more details about the behavior of DC/DC converter currents with respect to the switching sequence in continuous conduction mode.

Figure 3.16 states that $i_{D_2}(k)$ is fed by $i_L(k)$ when both switches are "OFF" (s = 0). However, while the switches are both still "OFF", the inductor discharges the magnetized current

$i_L(k)$ into $i_o(k)$ and $i_{dc\_link}(k)$. Further, $i_{dc\_link}(k)$ discharges into $i_o(k)$ when both switches are "ON" (s = 1) and both diodes are "OFF" (D = 0).

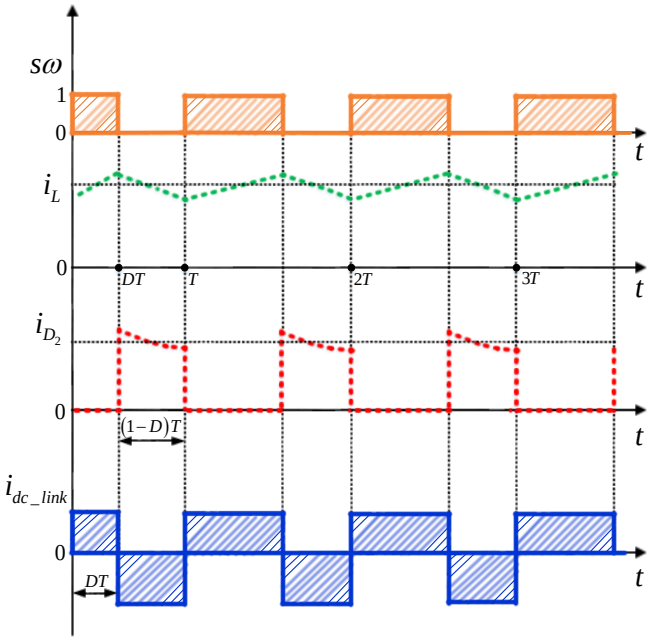

Figure 3.16: Currents in continuous conduction mode during two switching states

Also, the $i_{dc\_link}(k)$ switches the direction because of the charge and discharge of DC link capacitor based on the switching states.

Furthermore, the positive buck-boost converter is analyzed in continuous conduction mode during two switching states to obtain all the currents node equations that precisely describe the mathematical relationship between the PV input current $i_{pv}(t)$ and both measured voltages $V_{pv}(t)$ and $V_{dc\_link}(t)$ through the two existing sensors. Accordingly, Figure 3.17 analyzes the DC/DC converter in continuous conduction mode during first switching states, i.e., when S_1, S_2 are ON and D_1, D_2 are turned OFF.

First, when the switches are turned ON (S_1&S_2=1), the node equations are given by:

$$i_{pv}(t) = i_{c_{in}}(t) + i_L(t) \tag{3.54}$$

$$i_{dc\_link}(t) = i_o(t) \tag{3.55}$$

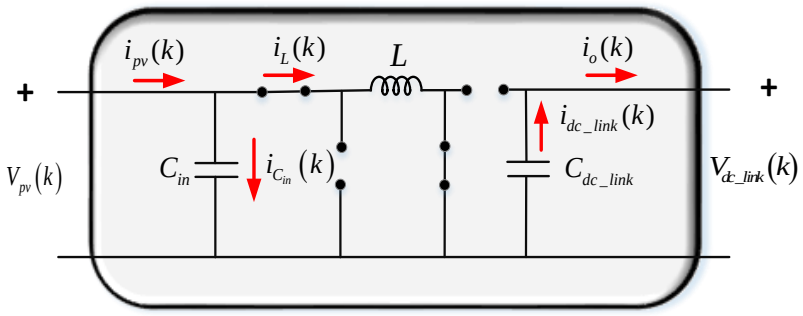

Figure 3.17: Converter currents when switches S_1, S_2 are ON and D_1, D_2 are turned OFF

Where $i_L(t)$ is the magnetizing inductor current, $i_{C_{in}}(t)$ is the current of PV input capacitor and output current, $i_o(t)$ of the DC/DC converter.

Second, when the switches are turned OFF (S_1&S_2=0), currents node equations are obtained by:

$$i_{pv}(t) = i_{c_{in}}(t) \tag{3.56}$$

$$i_L(t) = i_{dc\_link}(t) + i_o(t) \tag{3.57}$$

According to Figure 3.17 and Figure 3.18 and the two modes equations, the PV input current $i_{pv}(t)$ equation that is based on switching states can be written in this form:

$i_{pv}(t) = i_{C_{in}}(t) + i_L(t)$, and since $i_L(t) = i_{dc\_link}(t) + i_o(t)$

Figure 3.18: Converter currents when switches S_1, S_2 are OFF and D_1, D_2 are turned ON

Therefore, the $i_{pv}(t)$ equation that can precisely represent the PV current in two different switching states is given by:

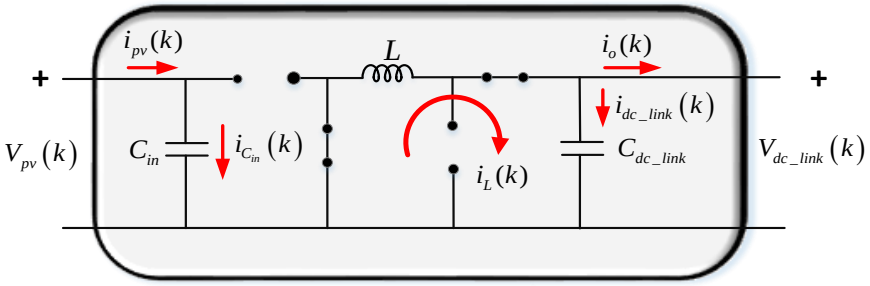

Figure 3.18: Converter currents when switches S1, S2 are OFF and D1, D2 are turned ON

$$i_{pv}(t) = i_{c_{in}}(t) + (S)\left[i_L(t)\right] = i_{c_{in}}(t) + (S)\left[i_{dc\_link}(t) + i_o(t)\right] \tag{3.58}$$

likewise, the equations of $i_{pv}(t)$, based on the switching states are as follows:

when S=1

$$i_{pv}(t) = i_{c_{in}}(t) + (S=1)\left[i_{dc\_link}(t) + i_o(t)\right] = i_{c_{in}}(t) + i_{dc\_link}(t) + i_o(t) \tag{3.59}$$

when S=0

$$i_{pv}(t) = i_{c_{in}}(t) + (S=0)\left[i_{dc\_link}(t) + i_o(t)\right] = i_{c_{in}}(t) \tag{3.60}$$

The average $i_{pv}(t)$ as function of measured voltages $V_{pv}(t)$ and $V_{dc\_link}(t)$ is given by:

Likewise, when S=1

$$i_{pv}(t) = C_{in}\frac{dv_{pv}}{dt} + C_{dc\_link}\frac{dv_{dc\_link}}{dt} + i_o(t) \tag{3.61}$$

when S=0

$$i_{pv}(t) = C_{in}\frac{dv_{C_{in}}}{dt} \tag{3.62}$$

From the power injection model presented in next section, the current $i_o(t)$ can be simply found by calculating the injected active power and DC link voltage received from the DC link sensor. Therefore $i_o(t)$ equation is given by:

$$i_o(t) = \frac{\overset{*}{P}_{qd}(t)}{V_{dc\_link}(t)} \tag{3.63}$$

At a steady state, Equation (3.61) in discrete time can be written by using the Forward (Standard) Euler method for discretization to solve first order first degree differential equations with a given initial value of both measurements V_{pv} and V_{dc_link}.

$$\begin{aligned} i_{pv}(k) = {} & \frac{C_{in}}{T_s}\left[{V_{pv}}^{S=\{0,1\}}(k+1) - V_{pv}(k)\right] + ... \\ & \left\{\frac{C_{dc\_link}}{T_s}\left[{V_{dc\_link}}^{S=\{0,1\}}(k+1) - V_{dc\_link}(k)\right] + \frac{\overset{*}{P}_{qd}(k)}{V_{dc\_link}(k)}\right\} \end{aligned} \tag{3.64}$$

where $V_{pv}(k)$ and $V_{dc\_link}(k)$ are the recent measurements of PV voltage and DC link voltage respectively at the current sample time (k). However, $V_{pv}(k+1)$ and $V_{dc\_link}(k)$ are the predictive voltages at the next sampling time $(k+1)$ and both are obtained from the discrete time model of a positive buck-boost converter in two switching modes in the continuous conduction mode. From Equation (3.64), it is clear that the PV input current is directly related to the PV input voltage and DC link voltage. This equation is effectively applied in the proposed current sensorless model to eliminate the current sensor. Further, at a steady state, the $V_{dc\_link}(k)$ and $V_{dc\_link}(k+1)$

are approximately equal, especially if the sampling time is too small and indeed in PV grid-tied systems, the DC link voltage must be controlled to maintain completely fixed. Hence, when switches are both ON the predicted voltage is given by:

$$V_{pv}(k+1)^{S=1} = V_{pv}(k) + \frac{T_s}{C_{dc\_link}}\left[\frac{P^{*}_{qd}(k)}{V_{dc\_link}(k)}\right]\left(\frac{D}{1-D}\right) \tag{3.65}$$

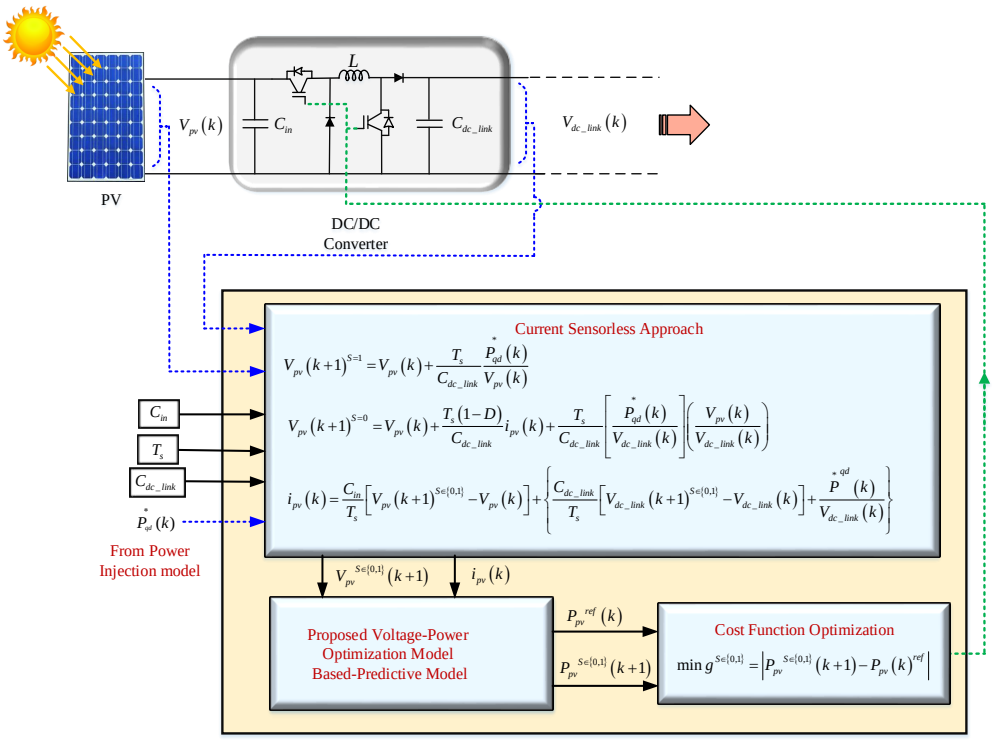

Figure 3.19: Block diagram for current sensorless model

Where T_s is the sampling period of the MPC microprocessor and D is the duty cycle of a positive buck-boost converter:

$$D = \frac{T_{on}}{T_s} = \frac{V_{dc\_link}(k)}{V_{pv}(k) + V_{dc\_link}(k)} \tag{3.66}$$

Therefore, for simplification, the predicted $V_{pv}(k+1)^{S=1}$ can be rewritten in terms of $V_{pv}(k)$

$$V_{pv}(k+1)^{S=1} = V_{pv}(k) + \frac{T_s}{C_{dc\_link}}\left[\frac{\overset{*}{P}_{qd}(k)}{V_{pv}(k)}\right] \tag{3.67}$$

Next, the predicted $V_{pv}(k+1)^{S=0}$ when the switches are turned OFF:

$$V_{pv}(k+1)^{S=0} = V_{pv}(k) + \frac{T_s(1-D)}{C_{dc\_link}} i_{pv}(k) + \frac{T_s}{C_{dc\_link}}\left[\frac{\overset{*}{P}_{qd}(k)}{V_{dc\_link}(k)}\right]\left(\frac{V_{pv}(k)}{V_{dc\_link}(k)}\right) \tag{3.68}$$

It also can be written in this form:

$$V_{pv}(k+1)^{S=0} = V_{pv}(k) + \frac{T_s(1-D)}{C_{dc\_link}} i_{pv}(k) + \frac{T_s}{C_{dc\_link}}\left[\frac{\overset{*}{P}_{qd}(k)}{V_{dc\_link}(k)}\right]\left(\frac{1-D}{D}\right) \tag{3.69}$$

The block diagram in Figure 3.19 presents a scheme of current sensorless based model predictive control. Both $V_{pv}(k+1)^{S=1}$ and $V_{pv}(k+1)^{S=0}$ are substituted in Figure 3.64 along with recent measurements of $V_{pv}(t)$, and $V_{dc\_link}(t)$ to develop a predictive model for the PV- side current determines $i_{pv}(t)$. Thus, Figure 3.64 is used as an observer model for the PV current to eliminate the current sensor. This section elaborates that the behavior of a voltage's variable can be predicted at the next sampling time (k + 1) by derived discrete time set equations. The predicted PV voltage for the positive buck-boost converter is given by Figure 3.67 when the switches are ON and Figure 3.68 when the switches are OFF. In addition, the output current fed into the grid is variable and controlled by the power injection model. Hence, an effective calculation can find the output current from active power as specified in Figure 3.94, which can simply provide better monitoring on the injected current using an observer-based approach, without need for current $i_o(t)$ measurement.

To conclude, it is clear that the proposed predictive model is well-analyzed and designed. It uses only the already existing sensors of $V_{pv}(t)$ and $V_{dc\_link}(t)$ for the PV input voltage and DC link voltage, respectively. The relationship between PV current and output current is given in Equation (3.64) and illustrated in Figure 3.19. Moreover, in terms of engineering trade-off, showing small ripples in transient response will make a difference in performance. It is a feasible option and worth it to cut down on equipment costs rather than have the current sensor. The proposed system has been validated experimentally and analytically using PLECS simulation. Current-sensorless model for MPPT implementation results are provided in Chapter 4 as shown in Figures 4.31 and 4.32. The obtained results display a similar current signal to classical sensors whereas traditional MPPT methods achieve the maximum power via direct current measurement. The proposed schematic avoids the drawbacks of traditional current sensors while retaining MPPT capability. The available microcontrollers-based approach allows an easy implementation of such model and tuning of the MPPT algorithms in response to the environmental conditions. The proposed can partially decrease the cost of expensive PV solar power harvesting systems.

3.5 Controllable Power Injection Model:

The active power is the actual power used to provide useful work while the reactive power upholds the grid voltage against failure due to increases in power demand. Therefore, the reactive power reserve is available within the grid to support the AC voltage bus and prevent voltage collapse under increases in load conditions or faults disturbance. One of the DC power sources is the PV panels where only active power is being generated. Consequently, no reactive power is associated with PV modules. The maximum active power can be extracted and varied by controlling the DC/DC converters. However, reactive power cannot be absorbed or injected in the stand-alone PV

systems. In the meantime, the reactive power is a unique concept of AC power, and thus the DC/AC inverters can effectively inject the reactive power into the grid. In order to inject reactive power into a utility grid, the injected AC current must be in phase shift with grid voltage based on the desired power factor. When the PV module is directly connected to the inverter, the d-axis current is used to control the active power. The reactive power is controlled by q-axis current.

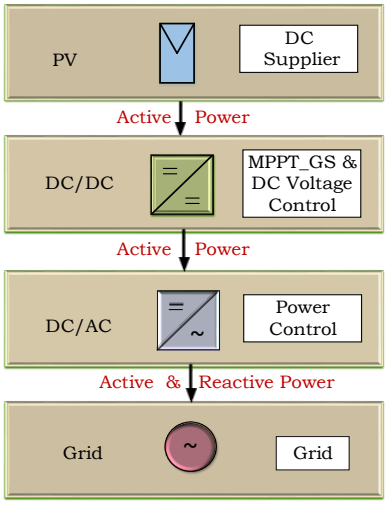

Figure 3.20: The block diagram of a grid-connected PV solar system

This is a common structure known as single stage conversion. Figure 3.20 presents a power flow diagram that shows that the generated DC power flows from PV arrays as a DC power supplier throughout DC/DC. Once reached, the DC/AC converter's reactive power occurs along with active power and both are injected into the grid. Therefore, controlling both converters will be imperative to develop an efficient model of a PV grid-connected system, and consequently, it will improve the PV system's performance and regulate the reactive power. The amount of reactive power in the utility grid is based on the operation requirements and the location of the reactive power reserves as well as the voltage drop due to overloading. Moreover, voltage stability is the ability of an electrical power system to preserve a satisfactory voltage at all grid buses whether the

system is under normal operating conditions or has been subjected to transient environments. An inadequate reactive power resource leads to partial or full system collapse. Hence, the reserve of reactive power is a critical indicator of voltage stability level in order to avoid voltage collapse, and, consequently, all the control centers over the world have installed reactive power monitors.

3.5.1 Grid-Connected PV System Based on Classical DC/AC Inverters:

The generated DC power by PV solar arrays flows through a DC/DC positive buck-boost converter. The proposed system is built from a PV string that includes ten modules connected to a DC/AC positive buck-boost converter, and the total power capacity defines the number of PV modules and how they connect to each other. Further, the DC/DC converter is connected to DC/AC classical inverter through a capacitor demonstrated as Vdc link.

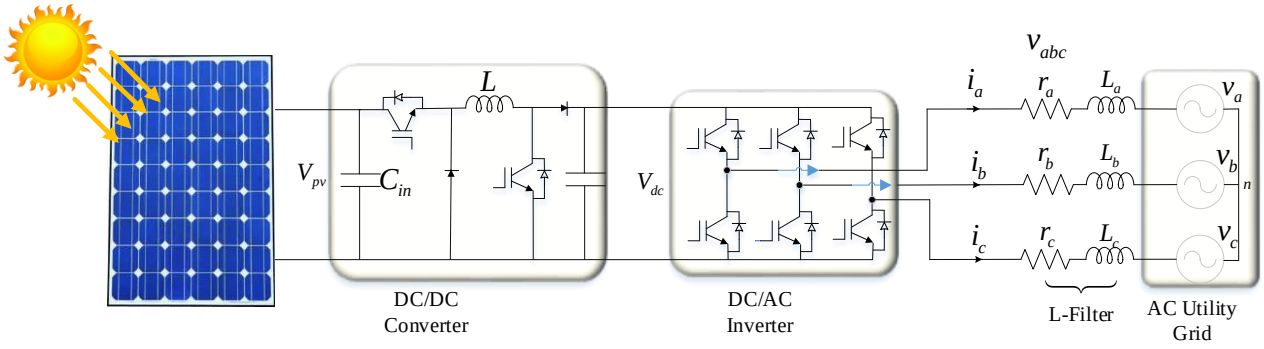

Figure 3.21: Grid connected PV solar system using traditional DC/AC inverter

Here, the proposed power control model is responsible for directing the DC/AC inverter to inject the AC power into the grid throughout the L-filter. Note: The L-filter is part of the proposed system. Figure 3.21 shows the power stage of the proposed system without the control models' scheme. The advantage of introducing the power injection model is not limited to increasing the decentralized generation share in distribution grids to improve the voltage regulation but also can contribute to power factor correction. Both are apparently major factors that contribute to system

stability enhancement. The q and d components of the injected power control are used to control the active and reactive power that are fed into the grid based on the desired power factor. The desired voltage vector in $q-d$ rotating reference frame is $\overset{*}{V}_{qd}$ generated by a power injection model. According to the power factor, the generated current will be in phase shift with the utility grid voltage. The magnitude of $\overset{*}{V}_{qd}$ depends also on the commanded V_{dc_link} and inverter gain k_{inv} The power injection control contains three major blocks:

1. Power injection model.
2. The stationary reference frame $\alpha-\beta$ transformation.
3. Space vector modulation (SVM) technique.

The three-phase equations can be avoided by using $q-d$ stationary reference frame equations. The following mathematical formula gives the relationship between the three phase voltages and the voltages in $q-d$ stationary reference frame:

$$V_{ref}^{\ Space\_Vector} = V_q + jV_d = \frac{2}{3}\left(V_{an} + V_{bn}e^{-j\frac{2\pi}{3}} + V_{cn}e^{j\frac{2\pi}{3}}\right) \tag{3.70}$$

Where V_{an}, V_{bn}, and V_{cn}, are three phase voltages, and V_{ref}, is the reference voltage vector, rotating at an angular speed of $\omega = 2\pi f$

Figure 3.22 illustrates $q-d$ rotating reference frame circuits that represents the $q-d$ equivalent circuit of a three phase in two dimensions. The $q-d$ values of the input voltages to the $q-d$ equivalent circuits in the synchronous reference frame are found based on the synchronous reference frame $\omega = \omega_e$ (synchronous speed).

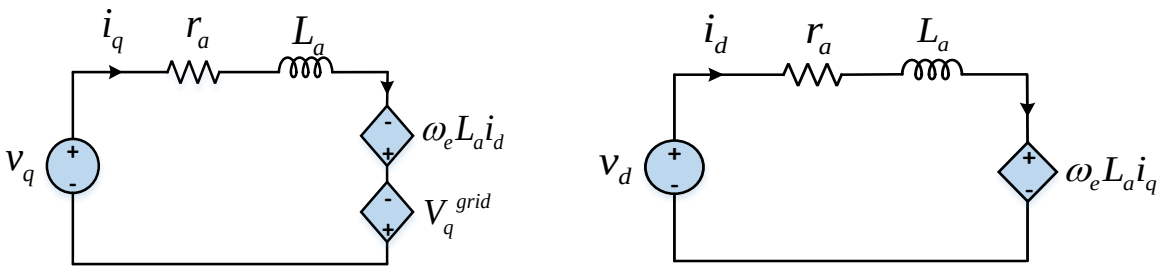

(a) q-axis circuit (b). d-axis circuit

Figure 3.22: The $q-d$ equivalent circuits

In the steady state condition, the derivative terms in the $q-d$ equivalent circuits are equal to zero, whether inductors or capacitors are both eliminated. Since the modulation strategy is SVM, the inverter gain is given by:

$$k_{inv} = \frac{\sqrt{v_{qs}^{\ 2} + v_{ds}^{\ 2}}}{V_{dc\_link}} \tag{3.71}$$

Thus, for different modulations such as sine wave modulation, the DC link voltage is divided by 2. The voltage equation V_s can be found by:

$$\left|\vec{v}_s\right| = \sqrt{v_q^{\ 2} + v_d^{\ 2}} = k_{inv} V_{dc\_link} \tag{3.72}$$

Therefore, an analytical expression model derives for calculating V_d and V_q from the following

$$\frac{I_d}{I_q} = -\frac{I_s \sin\phi}{I_s \cos\phi} = -\tan\phi = -\tan\left[\cos^{-1}\left(p.f\right)\right] \tag{3.73}$$

Steady state equations:

$$V_d^{\ 2} + V_q^{\ 2} = \left(k_{inv}\right)^2 \left(V_{dc\_link}\right)^2 \tag{3.74}$$

$$V_d = r_a I_d - \omega_e L_a I_q \tag{3.75}$$

$$V_q = r_a I_d + \omega_e L_a I_q + V_q^{grid} \tag{3.76}$$

$$I_d = -I_q \tan\left[\cos^{-1}\left(p.f\right)\right] \tag{3.77}$$

Where:

V_q & I_q : Voltage and current reference frame at q axis.

V_d & I_d : Voltage and current reference frame at d axis.

V_q^{grid} : The grid voltage, here V_q^{grid} =120 V.

V_{dc_link} : The DC link voltage is the output of the DC/DC converter.

r_a : Grid resistor at phase "A" and assumed to be the same at every phase.

L_a : The grid inductance at phase "A" and assumed to be the same at every phase.

ω_e : Grid angular frequency.

k_{inv} : DC/AC inverter gain.

Power factor is a ratio that provides the phase angle between the injected current and utility grid voltage. The power injection model is derived mathematically to generate a reference value of rotating reference frame V_{qd}^* . The V_q^* and V_d^* controls the inverter through SVM model converge according to the provided k_{inv} and will also shift the injected current into the grid by phase angles the same as the commanded power factor $p.f$.

Therefore, the generated reference vector depends on the commanded power factor, DC link voltage, and inverter gain, which is based on the difference between DC link voltage and its reference.

$$\left(r_a I_d - \omega_e L_a I_q\right)^2 + \left(r_a I_q + \omega_e L_a I_d + V_q^{\,grid}\right)^2 = \left(k_{inv}\right)^2 \left(V_{dc\_link}\right)^2 \tag{3.78}$$

The equation

$$\begin{aligned} &r_a{}^2 I_d{}^2 - 2 r_a I_d I_q \omega_e L_a + \omega_e{}^2 L_a{}^2 I_q{}^2 + r_a{}^2 I_q{}^2 + 2\left(r_a I_q\right)\left(\omega_e L_a I_d + V_q^{\,grid}\right) + \left(\omega_e L_a I_d + V_q^{\,grid}\right)^2 \\ &= \left(k_{inv}\right)^2 \left(V_{dc\_link}\right)^2 \end{aligned} \tag{3.79}$$

The equation

$$\begin{aligned} &r_a{}^2 I_d{}^2 - 2 r_a I_q I_d \omega_e L_a + \omega_e{}^2 L_a{}^2 I_q{}^2 + r_a{}^2 I_q{}^2 + 2 r_a I_q \omega_e L_a I_d + 2 r_a I_q V_q^{\,grid} + \ldots\ldots \\ &\omega_e{}^2 L_a{}^2 I_d{}^2 + 2\omega_e L_a I_d V_q^{\,grid} + \left(V_q^{\,grid}\right)^2 = \left(k_{inv}\right)^2 \left(V_{dc\_link}\right)^2 \end{aligned} \tag{3.80}$$

By substituting I_d since $I_d = -I_q \tan\left(\cos^{-1} p.f\right)$, the equation can be written in this form:

$$\begin{aligned} &r_a{}^2 \left[-I_q \tan\left(\cos^{-1} p.f\right)\right]^2 - 2 r_a I_q \omega_e L_a \left[-I_q \tan\left(\cos^{-1} p.f\right)\right] + \omega_e{}^2 L_a{}^2 I_q{}^2 + r_a{}^2 I_q{}^2 \ldots\ldots \\ &+2 r_a I_q \omega_e L_a \left[-I_q \tan\left(\cos^{-1} p.f\right)\right] + 2 r_a I_q V_q^{\,grid} + \omega_e{}^2 L_a{}^2 \left[-I_q \tan\left(\cos^{-1} p.f\right)\right]^2 \ldots\ldots\ldots \\ &+2\omega_e L_a V_q^{\,grid} \left[-i_q \tan\left(\cos^{-1} p.f\right)\right] + \left(V_q^{\,grid}\right)^2 = \left(k_{inv}\right)^2 \left(V_{dc\_link}\right)^2 \end{aligned} \tag{3.81}$$

Now by rewriting the equation in terms of I_q

$$\begin{aligned} &r_a{}^2 I_q{}^2 \tan^2\left(\cos^{-1} p.f\right) + 2 r_a I_q{}^2 \omega_e L_a \tan\left(\cos^{-1} p.f\right) + \omega_e{}^2 L_a{}^2 I_q{}^2 \ldots\ldots \\ &+r_a{}^2 I_q{}^2 - 2 r_a I_q{}^2 \omega_e L_a \tan\left(\cos^{-1} p.f\right) - \omega_e{}^2 L_a{}^2 I_q{}^2 \tan^2\left(\cos^{-1} p.f\right) \ldots\ldots \\ &+2 r_a I_q V_q^{\,grid} - 2\omega_e L_a V_q^{\,grid} I_q \tan\left(\cos^{-1} p.f\right) + \left(V_q^{\,grid}\right)^2 = \left(k_{inv}\right)^2 \left(V_{dc\_link}\right)^2 \end{aligned} \tag{3.82}$$

Finally, the equation can be rearranged as a function of I_q. Therefore, the current I_q is found from the following mathematical formula:

$$\begin{aligned}&\left[r_a^{\,2}\tan^2\left(\cos^{-1}p.f\right)+2r_a\omega_e L_a\tan\left(\cos^{-1}p.f\right)+\omega_e^{\,2}L_a^{\,2}+r_a^{\,2}-2r_a\omega_e L_a\tan\left(\cos^{-1}p.f\right).....\right.\\&\left.-\omega_e^{\,2}L_a^{\,2}\tan^2\left(\cos^{-1}p.f\right)\right]I_q^{\,2}+\left[2r_aV_q^{\,grid}-2\omega_e L_aV_q^{\,grid}\tan\left(\cos^{-1}p.f\right)\right]I_q+.....\\&\left(V_q^{\,grid}\right)^2-\left(k_{inv}\right)^2\left(V_{dc\_link}\right)^2=0\end{aligned}\tag{3.83}$$

Then, after solving Equation (3.83) mathematically and find i_q, plug in the value in Equations (3.75), (3.76), and (3.77) to get the commanded V_{qd}^{*} .

3.5.2 The Mathematical Transformation from q-d Axis to α-β Axis

The q axis is the reference, thus the transformation from rotating reference frame $q-d$ to the stationary reference frame $\alpha-\beta$ will have a different formula and it can be written based on Figure 3.23:

$$V_\alpha=V_s\cos\left(\theta_v+\phi\right)\tag{3.84}$$

$$V_\beta=V_s\sin\left(\theta_v+\phi\right)\tag{3.85}$$

From Figure 3.23, $\cos\theta_v$ and $\sin\theta_v$ can be found by using the phasor diagram, therefore:

$$\cos\theta_v=\frac{V_q}{V_s}\tag{3.86}$$

$$\sin\theta_v=\frac{V_d}{V_s}\tag{3.87}$$

The mathematical expanding formula for $\cos\left(\theta_v+\phi\right)$ and $\sin\left(\theta_v+\phi\right)$ are given by:

$$\cos\left(\theta_v+\phi\right)=\cos\theta_v\cos\phi-\sin\theta_v\sin\phi \tag{3.88}$$

$$\sin\left(\theta_v+\phi\right)=\sin\theta_v\cos\phi+\cos\theta_v\sin\phi \tag{3.89}$$

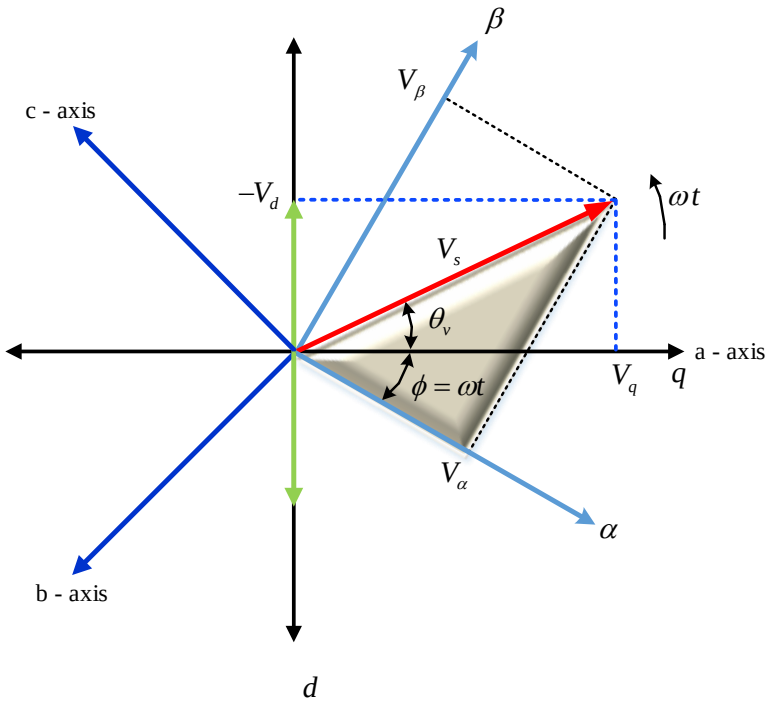

Figure 3.23: The voltages in $q-d$ coordinator

Thus, $\alpha-\beta$ transformation equations will be calculated as shown, since $q-axis$ is the reference axis:

$$V_\alpha=\cancel{V_s}\left[\frac{V_q}{\cancel{V_s}}\cos\phi-\left(-\frac{V_d}{\cancel{V_s}}\sin\phi\right)\right]=V_q\cos\phi+V_d\sin\phi \tag{3.90}$$

$$V_\beta=\cancel{V_s}\left(\frac{V_q}{\cancel{V_s}}\sin\phi-\frac{V_d}{\cancel{V_s}}\cos\phi\right)=V_q\sin\phi-V_d\cos\phi \tag{3.91}$$

Hence, the transformation when $q-axis$ is the reference axis:

. (3.92)

The following is the transformation equation from line to natural voltages to rotating reference frame:

$$\begin{bmatrix} v_q \\ v_d \end{bmatrix} = \frac{2}{3}\begin{bmatrix} -\sin\phi & -\sin(\phi-\gamma) & -\sin(\phi+\gamma) \\ \cos\phi & \cos(\phi-\gamma) & \cos(\phi+\gamma) \end{bmatrix}\begin{bmatrix} V_{an} \\ V_{bn} \\ V_{cn} \end{bmatrix}$$

The line to natural (phase) voltages of the utility grid are described by the following equations:

$$V_{an} = \sqrt{2}V_s \cos\omega t$$

$$V_{bn} = \sqrt{2}V_s \cos\left(\omega t - \frac{2\pi}{3}\right)$$

$$V_{cn} = \sqrt{2}V_s \cos\left(\omega t + \frac{2\pi}{3}\right)$$

In the proposed system the desired voltage vector $V_{qd}^{\ ref}$ or $\overset{*}{V}_{qd}$ is generated by the reactive power model and based on the reference values of power factor, inverter gain, and DC link voltage reference. The injected real and reactive power in $q-d$ domain is given by:

$$\begin{bmatrix} P \\ Q \end{bmatrix} = \frac{3}{2}\begin{bmatrix} V_q & V_d \\ V_d & -V_q \end{bmatrix}\begin{bmatrix} I_q \\ I_d \end{bmatrix} \quad (3.93)$$

or the equations can be written in this form where the $q-axis$ is the reference axis:

$$P = \frac{3}{2}\left(V_d i_d + V_q i_q\right) \quad (3.94)$$

$$Q = \frac{3}{2}\left(V_d i_q - V_q i_d\right) \quad (3.95)$$

Nonetheless, when the $d-axis$ is chosen as the reference then the power equation can be rewritten in this form:

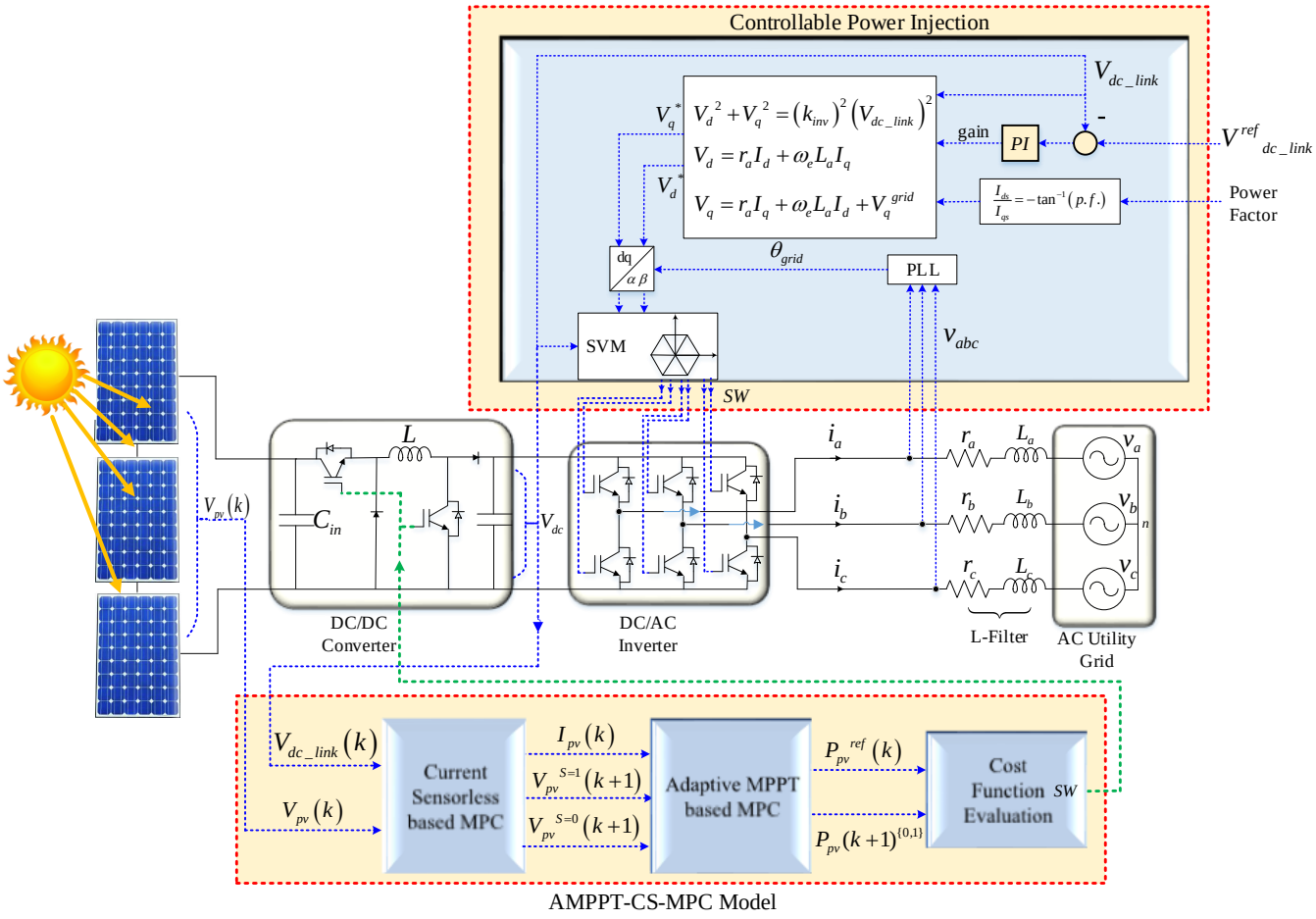

Figure 3.24: Grid connected PV solar system controlled by MPPT and grid power injection models

$$P=\frac{3}{2}\left(V_q i_q+V_d i_d\right) \tag{3.96}$$

$$Q=\frac{3}{2}\left(V_q i_d-V_d i_q\right) \tag{3.97}$$

A complete schematic for proposed control is shown in Figure 3.24 that gives a detailed topology for the unique system. As depicted, the proposed system is presenting V_{dc_link} control, and therefore, it can easily be set to a reference value within a designed range.

Indeed, the DC link capacitor is needed due to natural voltage fluctuation of the PV solar energy systems. Further, the capacitor will stabilize the DC link voltage against sudden voltage swinging and serve as a filter that eliminates the output voltage ripples. It also enhances the V_{dc_link} to remain constant in case of an instantaneous voltage dip or to recover the peak demand without causing voltage drops below the minimum required to ensure a continuous power delivery. DC link capacitor prevents any unexpected failure due to voltage collapse.

Stationary reference frame transforms the AC quantities into synchronously rotating $q-d$ frame which rotates at the grid frequency. After the transformation, the $q-d$ components of the injected grid current controls the reactive power. Generally, in order to transfer power from the PV side in one direction to the utility grid side, the magnitude of the DC link voltage must be higher than the amplitude of the AC voltage. As a result, the higher the DC link voltage, the less electrical current that is needed to transfer the same amount of power. Furthermore, increasing the DC link voltage will lead to reducing the DC current across the DC/DC converter side and, hence will lower the converter component rating. Voltage source inverter (VSI) is the selected three phase inverter. It has features of controllable voltage amplitude, phase and frequency. The inverter can utilize three states i.e., 0, $+V_{dc\_link}$ or $-V_{dc\_link}$ and the total possible switching pattern is 2^3. It includes (000, 001, 010, 011,100, 101, 110, 111) and the inverter can be driven to eight states. Both (000) and (111) are called two null vectors. Either all the bottom switches are turned ON or the top switches are turned ON. Both of them do not generate voltage, but they will be used to control the amplitude of the generated voltage vector V_s. The other six states are mainly applied

to form the stationary vectors in the $\alpha-\beta$ complex plane and they are known as six voltage vectors.

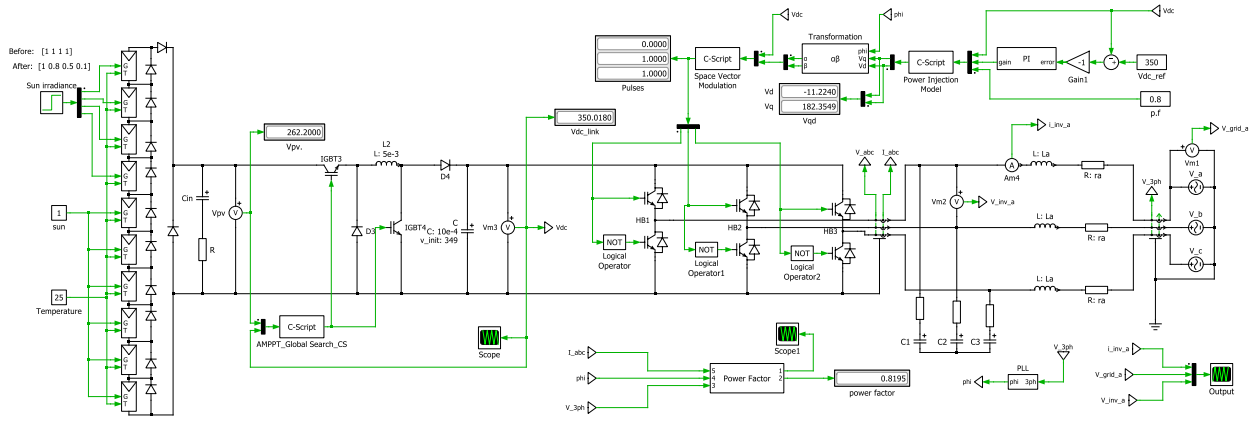

Figure 3.25: The PLECS schematic of PV grid -connected solar system

The model built and evaluated in the PLECS software generates a couple of excellent results and verifies the designed model accuracy. Figure 3.25 demonstrates the entire PV grid-tied system controlled by early introduced PV power extraction technique along with global search, the current sensorless model, and finally the power injection control scheme. The solar panels shown in the PLECS schematic are KC200GT.

Table 3.2: Parameters of Proposal PV Grid-Tied System

System Model Parameters	
Average switching frequency	f =100kHz
Sampling time	T_s =10 μs
DC link capacitor	V_{dc_link} = 350V
Resistor	$R = 0.2\Omega$
Inductor	$L = 50\mu H$

3.5.3 Conventional Space Vector Modulation

The space vector modulation, or SVM, was selected to utilize the proposed system and generate the required switching pulses sequence. It is more appropriate for reducing the total harmonic distortion (THD), an outstanding usage of the DC voltage link, and has an excellent minimization of switching losses [108, 136].

Space vector demonstrates three phase waveforms as a single rotating vector. The three phase voltages V_{abc} are associated to rotating reference frame $\vec{V}_{qd}^{ref}$ and the stationary reference vector $\vec{V}_{\alpha\beta}^{ref}$ (Reference Voltage Vector), i.e., generated via power injection model as shown in Equation 3.98. The tip of the space vectors, when joined together form a Hexagon, which is depicted graphically in Figure 3.26. The hexagonal contains six sectors revolving over 360 degrees, and each sector is 60 degrees. Thus, one sinusoidal wave cycle exhibits every one spin of the hexagon.

$$v_\alpha + jv_\beta = V_{an} + V_{bn}e^{-j\frac{2\pi}{3}} + V_{cn}e^{j\frac{2\pi}{3}} \tag{3.98}$$

Where $v_\alpha + jv_\beta$ are voltage in $\alpha - \beta$ transformation form, and V_{an}, V_{bn}, V_{cn} are phases voltages generated at inverter terminals and are equivalent to the generated $q-d$ reference voltage. From Figure 3.26 in each step, the SVM algorithm finds the three nearest voltage vectors ($V_{qd}{}^{x}$, $V_{qd}{}^{x+1}$, and $V_{qd}{}^{x+2}$) to the reference vector and switches between the three identified voltage vectors during one switching period $T_{s\omega}$. The T_1, T_2, and T_o are amount of time spent at each vector, which are

computed by Equation (3.99) [129]. The SVM strategy first finds the nearest vectors and then calculates the magnitude. After that, it detects the sector and finds the sector angle. Next, it computes the limitation of magnitude. Later, it calculates the relative vectors T_1, T_2, and T_o. The algorithm contains all the possible switching states of the inverter $[S_a\, S_b\, S_c]$. Finally, the SVM algorithm decides on the sequence of switching between the three voltage vectors and chooses an appropriate switching state for generating each voltage vector among the redundant states that lead to the same vector.

$$\begin{bmatrix} v_q^{\,x} & v_q^{\,x+1} & v_q^{\,x+2} \\ v_d^{\,x} & v_d^{\,x+1} & v_d^{\,x+2} \\ 1 & 1 & 1 \end{bmatrix} \begin{bmatrix} T_1 \\ T_2 \\ T_0 \end{bmatrix} = \begin{bmatrix} T_{s\omega} \times V_q^{\,*} \\ T_{s\omega} \times V_d^{\,*} \\ T_{s\omega} \end{bmatrix} \tag{3.99}$$

Where $T_{s\omega} = T_1 + T_2 + T_0$

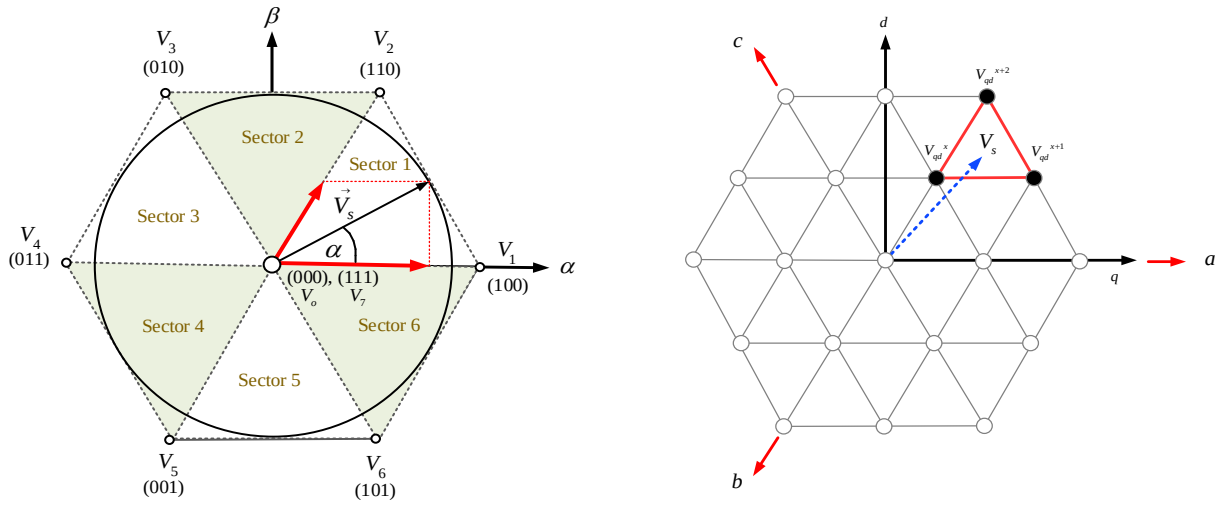

(a). Switching-state vectors of two-level converter in hexagonal coordinate system.

(b). Switching-state vectors of three level converter in hexagonal coordinate system.

Figure 3.26: Space vector modulation principles

Figure 3.26 illustrates the three phase waveforms generated by using the space vector modulation and shows each portion of generated waveforms based on each sector. The active state vectors, or space vectors, are 1 to 6 while 7 and 8 are zero state vectors. The magnitude of each of the six active vectors is equal to V_{dc}. The switching frequency can be minimized by using the zero state vectors (000) or (111) since they are redundant vectors. $\overset{*}{V}_{qd}$ (reference vector) rotates at the speed of the fundamental frequency of the inverter output voltage received from PLL while the space vectors are stationary. It rotates once for one cycle of the fundamental frequency ω.

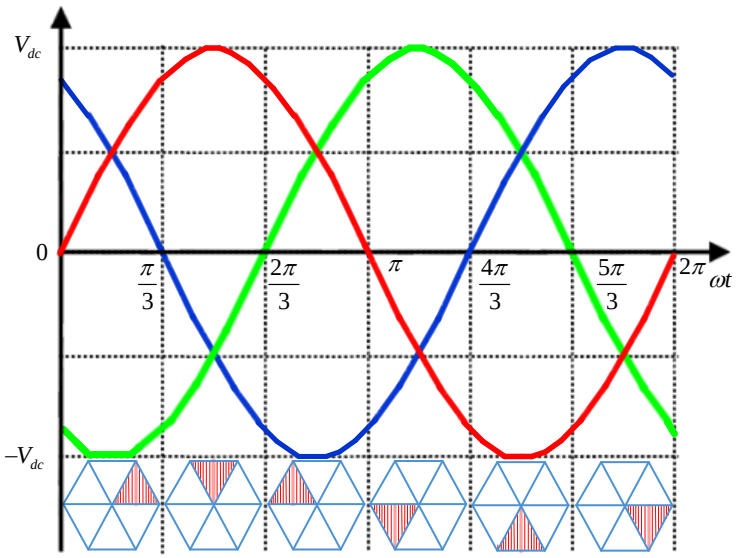

Figure 3.27: The generated three phase voltage using the SVM technique

For generating a given voltage waveform, the inverter moves from one state to another and it circles for one cycle of the fundamental frequency. Figure 3.27 depicts how each stationary vector clearly corresponds to a fundamental angular position. The reference voltage follows a circular trajectory in a linear modulation range and the output is sinusoidal.

In conclusion, the duty of the proposed model is to control the inject power indirectly by setting the desirable power factor. The model controls the phase shift angle of the injected current

with respect to the grid voltage. The space vector modulation will generate switching states corresponding to the generated reference voltage i.e., in a form of rotating reference frame V_{qd}^{*} .

3.6 PV Solar Grid-Connected System Based on A CHB Converter

Voltage fluctuating is the most common incident in PV solar systems due to natural variations in irradiance levels and ambient temperature. However, fluctuations in irradiance is a more frequent variation than in the temperature because of natural or non-natural phenomena. Moreover, it could get worse if it reaches the level of fully shaded. Figure 3.28 provides a block diagram summarizing the connection and control levels as well as the power flow direction of the PV grid connected system using a cascaded H-bridge inverter.

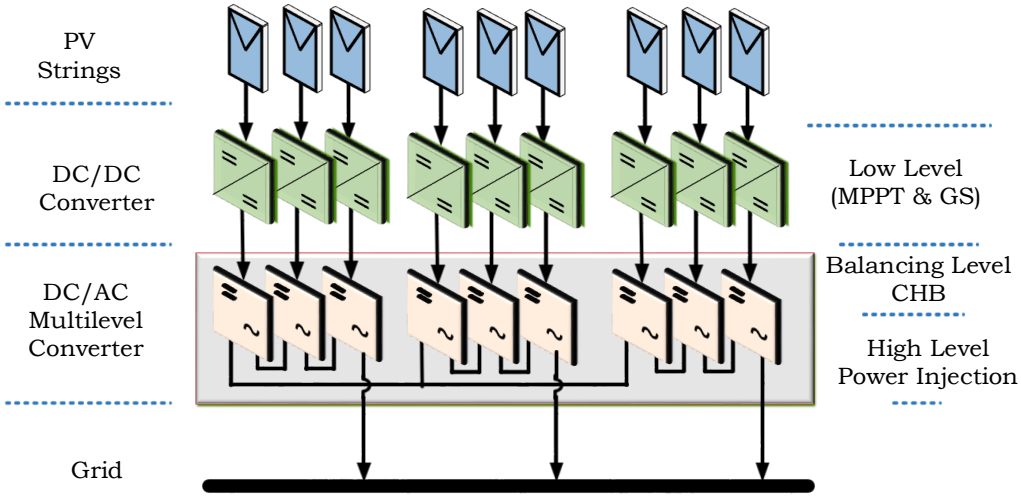

Figure 3.28: Schematic representation of introduced seven-level CHB-based grid connected PV inverter

In general, partial shading or dappled shading can be addressed efficiently by a global search approach as long as the PV panels are only partially limited to direct exposure of sunlight. Fully shaded or completely shaded modules are challenging phenomena. Severe and acute shading will lead to shutting the whole PV system down when the system primarily uses a traditional

DC/AC inverter. Neither central inverters nor micro-inverters can be effective in fully or completed shaded modules. Micro-power inverter is basically attached on the back of each individual module, but a central DC/DC converter is connected to a string of modules. If a multi-string or one string becomes entirely shaded, the complexity will increase and can also cause the whole PV grid-tied system to malfunction and lose synchronization since it no longer meets the grid requirement. It will quit immediately and turn OFF or continue to supply local islanded loads.

A cascaded H-bridge converter, or CHB, is an interesting alternative topology for high power drives, due to its good quality output signals, higher resolution, lower harmonic distortion and uniqueness in terms of each cell utilizing the DC source individually. Therefore, using the CHB converter seems practical, feasible and a very effective solution for such incidents and it may efficiently mitigate the consequences. Under severe partial shading conditions, the phase voltages change. As a result, the DC link voltages of each CHB cell becomes unbalanced and three phase voltage amplitudes for each phase are unequal in addition to line to line voltages.

3.6.1 Balancing Voltage Mismatch in a PV Grid-Connected System

The fully shaded cells of the CHB converter can potentially lead to expensive downtime and great losses on the consumer side. With a fundamental phase shift compensation, the operation can be extended and continue power delivery by utilizing the unshaded cells. Thus, the next section applies fundamental phase shift compensation that effectively balances the line to line voltage under severe shading although phase to neutral voltages are unequal. The aim is to increase the reliability of the system by first extending the operation using fundamental phase shift compensation to rebalance the line to line three phase voltages, even though the phase voltages still have unequal amplitude. Then through the introduced topology, the DC link voltage will be

raised up to increase the phase voltages and return to the same amplitude as under pre-shading conditions. It is true that the balanced will be achieved through the phase shift angle modification; however, the power injection cannot be fulfilled unless the PV system voltage is higher than the utility grid voltage. Figure 3.29 provides details of the PV grid-tied system connected through an H-bridge multilevel inverter.

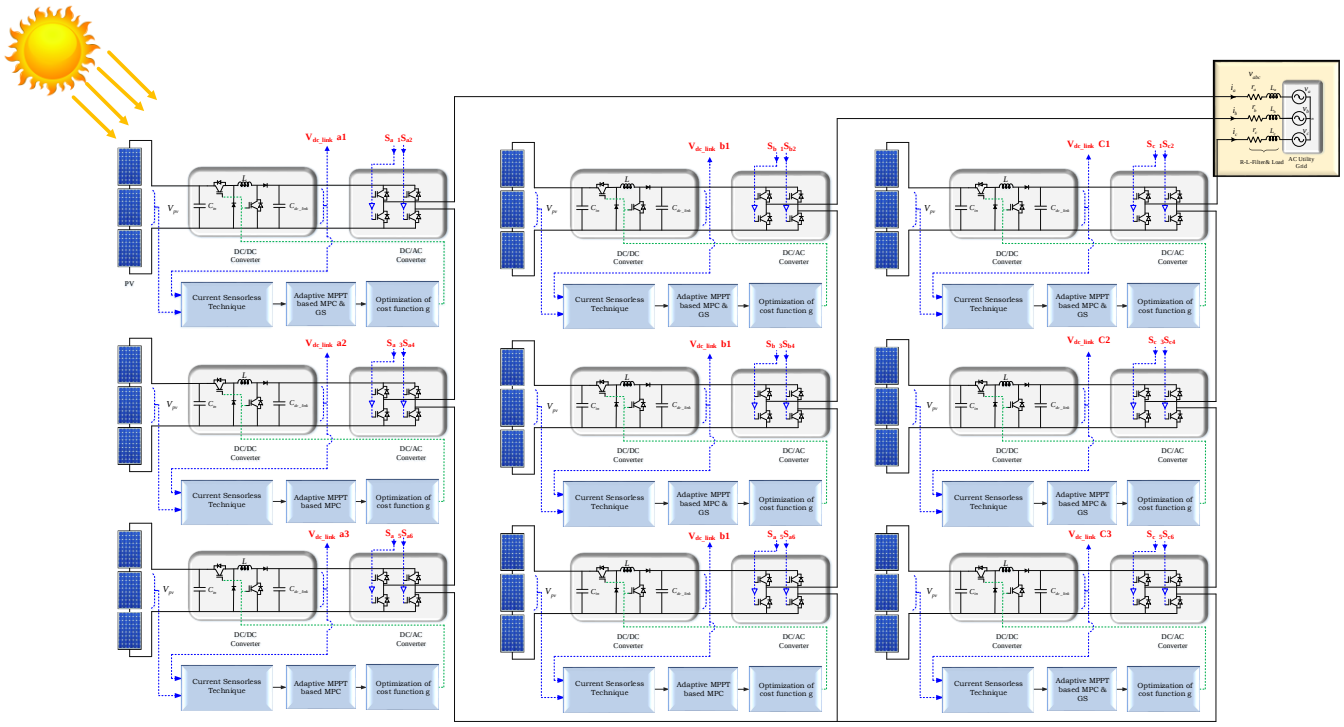

Figure 3.29: New comprehensive structure of a PV grid-connected solar system

3.6.2 Conventional Fundamental Phase Shift Compensation

In [114], the conventional fundamental phase-shift compensation strategy was proposed and discussed in [85]. Hence, in balanced normal operations and pre-shading condition, the line to line voltages are specified in this form:

$$\vec{V}_{ab}^{\,2} = \vec{V}_{bc}^{\,2} = \vec{V}_{ca}^{\,2} \tag{3.100}$$

The line to line voltages V_{ab}, V_{bc} and V_{ca} equations can be written as a function of phase shift angles

$$V_{ab}^{\,2} = V^{2}_{a} + V_{b}^{\,2} - 2V_a V_b \cos\left(\phi_{ab}^{\,\circ}\right) \tag{3.101}$$

$$V_{bc}^{\,2} = V_{b}^{\,2} + V_{c}^{\,2} - 2V_b V_c \cos\left(\phi_{bc}^{\,\circ}\right) \tag{3.102}$$

$$V_{ca}^{\,2} = V_{c}^{\,2} + V_{a}^{\,2} - 2V_c V_a \cos\left(\phi_{ca}^{\,\circ}\right) \tag{3.103}$$

$$\phi_{ab}^{\,\circ} + \phi_{bc}^{\,\circ} + \phi_{ca}^{\,\circ} = 360^{\circ} \tag{3.104}$$

Where ϕ_{ab}, ϕ_{bc} and ϕ_{ca} are line to line angles between the phase voltages V_a, V_b and V_c. The method modifies the line-ground voltages to generate equal and balanced line to line voltages. Therefore, in the case of one or multi cells of CHB encounter severe shading in one single phase, the phase angles can result in balanced line to line voltages are calculated by solving the next set of given equations:

$$V_{a}^{\,2} + V_{b}^{\,2} - 2V_a V_b \cos\left(\phi_{ab}^{\,\circ}\right) = V_{b}^{\,2} + V_{c}^{\,2} - 2V_b V_c \cos\left(\phi_{bc}^{\,\circ}\right) \tag{3.105}$$

$$V_{b}^{\,2} + V_{c}^{\,2} - 2V_b V_c \cos\left(\phi_{bc}^{\,\circ}\right) = V_{c}^{\,2} + V_{a}^{\,2} - 2V_c V_a \cos\left(\phi_{ca}^{\,\circ}\right) \tag{3.106}$$

$$\phi_{ab}^{\,\circ} + \phi_{bc}^{\,\circ} + \phi_{ca}^{\,\circ} = 360^{\circ} \tag{3.107}$$

This mathematical model imposes balanced line to line voltages although phase voltages V_{an}, V_{bn}, and V_{cn} have different. The system can effectively prevent power delivery interruption

only to the local islanded loads since it no longer can continue supplying power into the utility grid as long as the line to line voltages' amplitude becomes a reduced amount of the pre-shading voltage. The condition of power injection fails despite the balancing that was achieved, since the voltage amplitude is less than the utility grid voltages. Therefore, the PV grid tied system implements new topology to avoid the discontinued grid power injection and to always maintain the grid synchronization requirements. The severe shading in some cases is a non-permanent incident that will clear during the earth's natural rotation. Therefore, this strategy can solve the incident temporarily during the full shading. Once the shading is cleared, normal operation will resume.

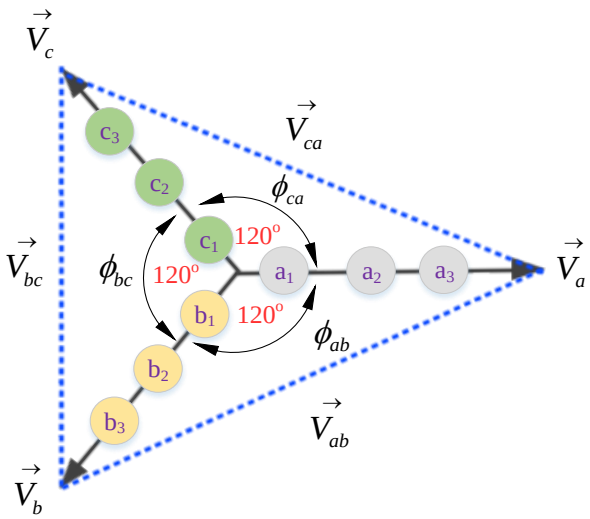

Figure 3.30: Balanced phasor diagram in normal operation

Figure 3.30 shows a phasor diagram of balanced line to line voltages in a normal operation case. When the system experiences complete shading and consequently the phase voltages become

unequal and unbalanced, line to line voltages will occur as long as: $\vec{V}_a \neq \vec{V}_b \neq \vec{V}_c$ and therefore, the line to line voltages become unequal and unbalanced as well $\vec{V}_{ab}^{\,2} \neq \vec{V}_{bc}^{\,2} \neq \vec{V}_{ca}^{\,2}$.

Figure 3.31 shows a phasor diagram when a number of CHB cells are fully shaded. By assuming only one cell lost sun exposure due to full shading in phase "B" and similarly two cells are completely shaded in phase "C", none are shaded in phase "A". By using Equations (3.105), (3.106), and (3.107,) the rebalancing line to line voltages is achieved.

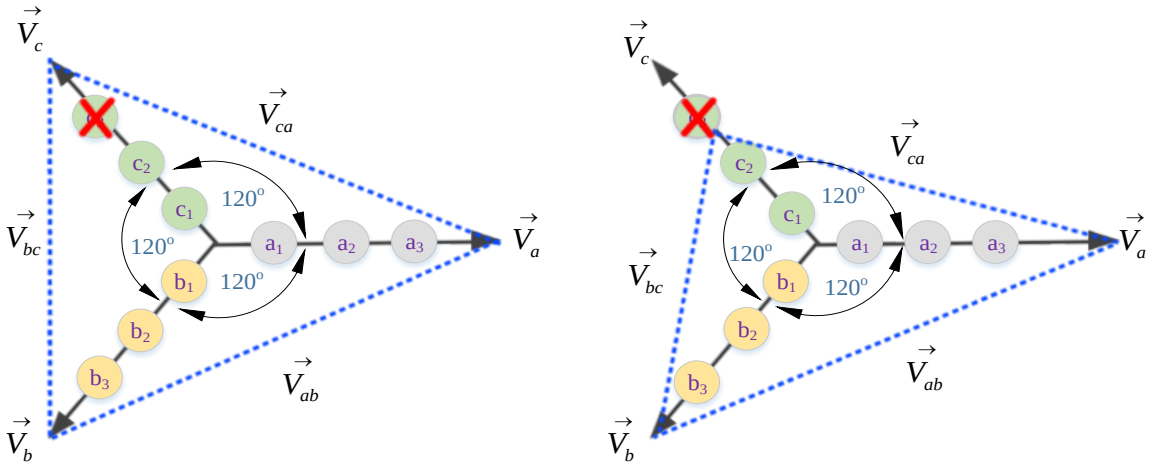

Figure 3.31: The voltage phasor diagram (one shaded cell at phase C)

Each unshaded cell of phases "A" and "B" measures at 58V and the DC link voltage is 174 V. In phase "C," two unshaded cells generate 58V and the DC link voltage total is 116 V. After solving the set of equations, the essential phase shift compensation angles for this case are $\phi_{bc}^{\circ} = \phi_{ca}^{\circ} = 130.5^{\circ}$ and $\phi_{ab}^{\circ} = 99^{\circ}$. According to Figure 3.32, an adjustment was made to the phase angles ϕ_{ab}°, ϕ_{ab}° and ϕ_{bc}°, and the amplitudes of the line-to-line voltages are all made equal as displayed in Chapter 4, Figure 4.44, where $V_{ab} = V_{bc} = V_{ca} =$ 290 V even though the amplitudes of the phase voltages V_a, V_b and V_c. are still unequal.

As a result, each of the modified phase angles are no longer equal as in the normal operation case when $\phi_{ab}^{\circ} = \phi_{bc}^{\circ} = \phi_{ca}^{\circ} = 120^{\circ}$. Additionally, this confirms the possibility of continuing power delivery and the PV system can still supply AC loads locally.

Two of the new phase shift angles increased higher than the pre-shading. The unshaded phase voltages (V_a and V_b) have shifted by more than 10.5° values to increase the line voltage of the effaced lines V_{bc} and V_{ca} to result in equal line to line voltages.

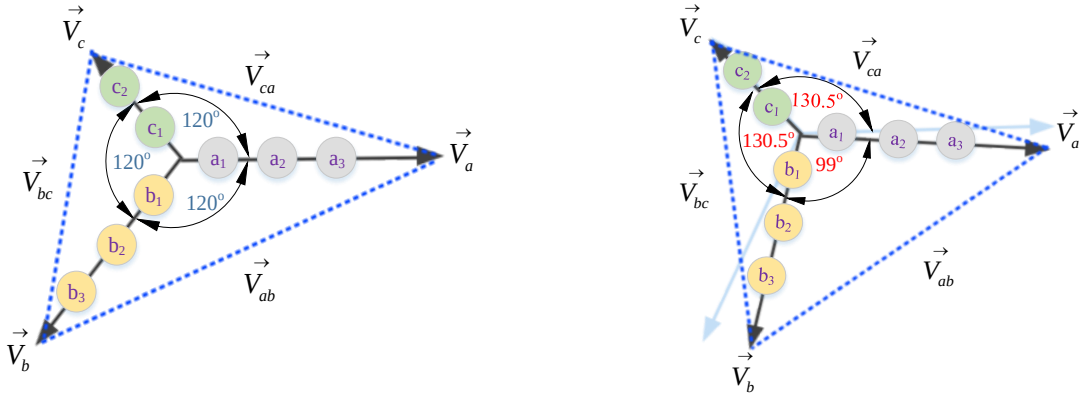

(a) Mismatch line to line voltages

(b) Equal and balanced line to line voltages

Figure 3.32: Phasors diagrams implementing phase shift compensation

3.6.3 New Scheme of PV Grid-Connected System Connected Through CHB

The previous section studied and described the principles of implementing the fundamental phase shift compensation technique as a unique method. This section manages the operation of the PV system to maintain power supply into the grid by boosting the DC link voltage and converging it at the reference DC link voltage.

The introduced method presents a new topology so that the voltage amplitude can be boosted to pre-shading amplitude in addition to recovering the voltage symmetry. As a result, the

new topology unified the DC link voltage balance and increased the CHB output voltages via boosting the DC link voltage based positive buck-boost voltage transfer ratio.

Before that, while the PV grid-tied system supplies local loads, it uses fundamental phase shift compensation as goal of continuing the power delivery. It highly increases the reliability of PV grid connected systems.

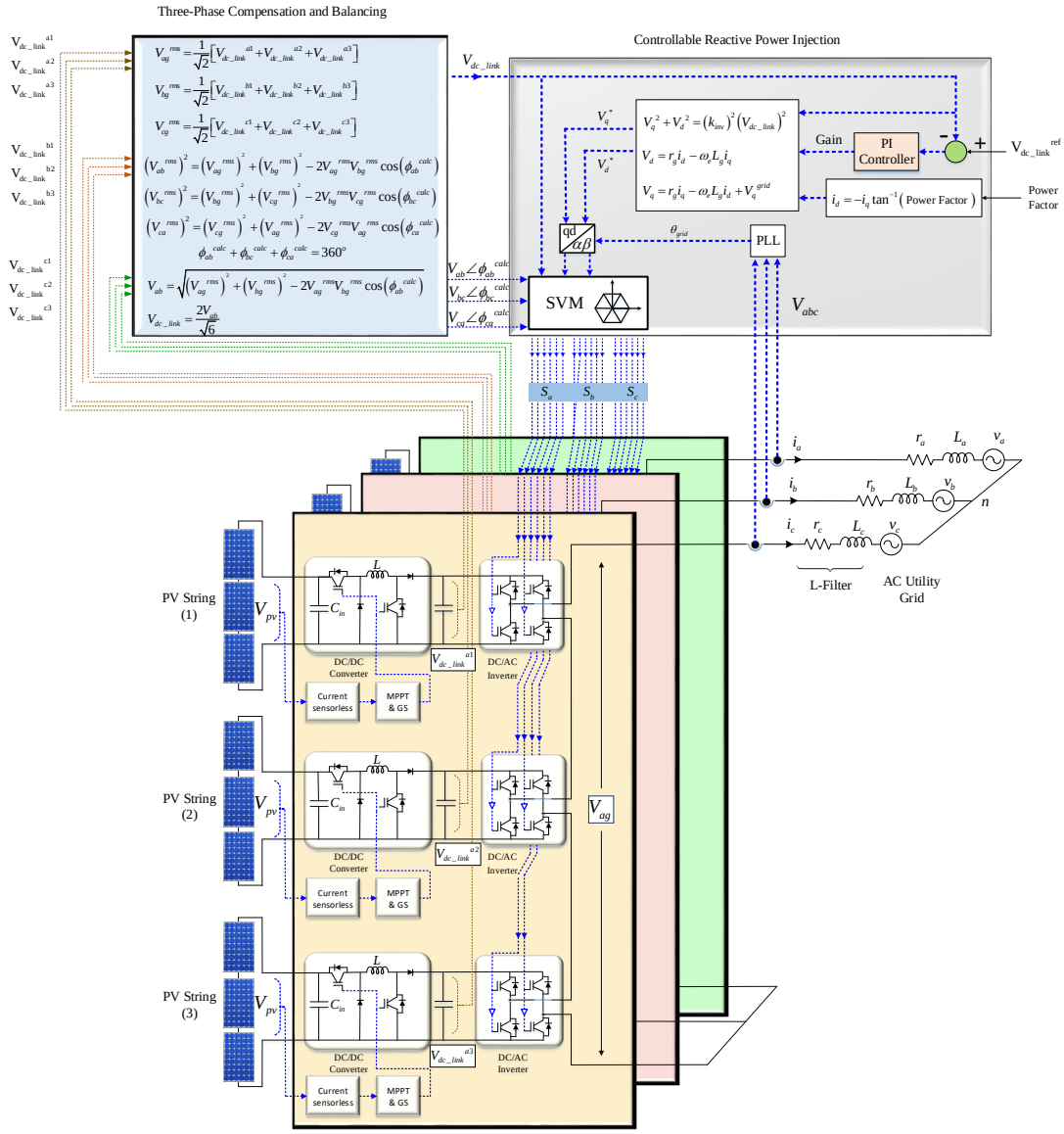

Figure 3.33: Proposed scheme configuration of a grid-connected PV solar system utilizing CHB

Figure 3.33 elaborates the proposed grid-connected PV system connected to a cascaded H-bridge converter. In the introduced system, the reference V_{dc_link} voltage is fully controlled and easily enforces the DC link voltage at each (phase) converter to converge at the commanded voltage throughout the severe shading. This forces the unshaded cells to generate output voltage the same as the pre-shading stage DC link voltage previously. The unique principles and procedures are summarized in the following steps:

First, the system successfully harvests the maximum power before a couple of the CHB cells start to experience complete shading and unequal generation occurs due to full shading panels. The global search tries to recover but it suddenly fails due to zero PV input power and it cannot eliminate the consequences of losing the CHB's cells.

Second, once a couple of CHB cells are turned off due to acute shading, the phases become unbalanced, and as a result, the three line to line voltage's amplitude are not equal and become asymmetrical.

Third, a quick treatment action will calculate the RMS value for each phase based on the received DC link voltages via already-installed DC link sensors.

$$\begin{aligned} V_{ag}^{\ rms} &= \frac{1}{\sqrt{2}}\left[V_{dc\_link}^{\ a1} + V_{dc\_link}^{\ a2} + V_{dc\_link}^{\ a3}\right] \\ V_{bg}^{\ rms} &= \frac{1}{\sqrt{2}}\left[V_{dc\_link}^{\ b1} + V_{dc\_link}^{\ b2} + V_{dc\_link}^{\ b3}\right] \\ V_{cg}^{\ rms} &= \frac{1}{\sqrt{2}}\left[V_{dc\_link}^{\ c1} + V_{dc\_link}^{\ c2} + V_{dc\_link}^{\ c3}\right] \end{aligned} \tag{3.108}$$

The RMS phase voltages are applied in Equations (3.105), (3.106), and (3.107) to compute the new phase shift angles $\phi_{ab}, \phi_{bc}, \phi_{ca}$ that will result in balanced line to line voltages. Then calculate the equivalent DC link voltage by using the following equation:

$$V_{dc\_link} = \frac{2V_{ab}^{new}}{\sqrt{6}} \tag{3.109}$$

Finally, the DC link voltage reference is now higher than the new computed V_{dc_link}. Through the effective feedback, the PI controller is designed to frequently update the generated gain in order to keep the unified DC link voltage increasing gradually and exactly converging at the DC link reference voltage. The DC link voltage must remain fixed in the PV grid-tied systems and greater than the grid voltage for power transferring assurance.

The system is designed to overcome occurrences of DC link voltage mismatch which will result in unequal line to line voltages. The DC/DC converters see that the required DC link voltage is still the same as pre-shading conditions although one of CHB's cell is already missed because of the full shading. The balanced model along with the power injection model carries out the DC/DC converter and start boosting the DC link voltage to reach higher line to line voltages and fulfill power injection conditions. Therefore, based on this shading scenario, the rating of the DC/DC converter must be considered at the design steps and calculated carefully so the capability of the converter can be increased to be able to adjust the voltage. The total harmonic distortion (THD), which measures the harmonic contents of waveform is going to increase in line to line voltage and can reach 8.03% in the line to line waveform i.e., synthesized by the effected phase. In this case phase C is the effected and has one shaded cells.

For example, let's assume there are three fully working (unshaded) cells of a cascaded H-bridge in phase A, phase B, and only one shaded cell in phase C. For each operating cell in phase C, the V_{MPP} of the PV input side voltage is 26.3 V×2 modules. Thus, the total input voltage at MPP for each unshaded CHB cell is equal to 52.6 V and the DC link voltage side at each cell is 58 V.

The total of three unshaded cells for each phase is 174 V. Now, upon the commanded $V_{dc\_link}^{ref}$ which equals to 174 V, the inverter's switching will control the DC link voltage to maintain at 174V. Therefore, the duty cycle for each positive buck-boost converter can be computed as follows:

The voltage transfer ratio is specified by:

$$V_{dc\_link}(k) = V_{pv}(k)\frac{D(k)}{1-D(k)} \tag{3.110}$$

where $D(k)$ is the desired duty cycle to achieve the inquired voltage boosting and the phases "A" and "B" have three active operating cells (unshaded cells):

$$D(k)^{Calc} = \frac{174/3(Cell)}{52+174/3(Cell)} = 0.527$$

The phase "C" has two active operating cells (one shaded cell), and each cell increases the voltage from 52V at the PV input side to 87V at the DC link side:

$$D(k)^{Calc} = \frac{174/2(Cell)}{52+174/2(Cell)} = 0.626$$

Table 3.3: Simulation Results When a PV Grid-Connected System Is Under Normal Operation

	$V_{dc\_link}^{1,2,3}$	V_{Lg}^{rms}	V_{LL}^{rms}	$V_{LL}^{\max}$	THD%
Phase "A"	58 V×3	123.055V	213.13V	348V	10.27%
Phase "B"	58 V×3	123.055V			
Phase "C"	58 V×3	123.055V			

Table 3.4: Simulation Results When a PV Grid-Connected System Is Under Fully Shaded Conditions

	$V_{dc\_link}^{1,2,3}$	V_{Lg}^{rms}	V_{LL}^{rms}	V_{LL}^{max}	THD% /phase
Phase "A"	58 V×3	123V	205.09V	290V	10.16%
Phase "B"	58 V×3	123V			11.34%
Phase "C"	58 V×2	82V			17.62%

Table 3.5: Simulation Results of a PV Grid-Connected System Though a Cascaded H-Bridge

		Pre-Shading Conditions				**Severe Shading Conditions**					
	Cascaded H-Bridge cells	PV MPP Voltage	DC link (Pre-shading)	Total DC link voltage	Line to line voltages	PV MPP Voltage (shading)	DC link at each cell (shading)	Total DC link (shading)	Line to line voltage (FPSC) V_{max}	New Duty cycles %	Balancing and Boosting
Phase A	Cell (1)	52.0	58.09	174.41	348.06	52.4	58.5	174.43	290	52.75	348.112
	Cell (2)	52.2	58.17			52.2	58.3			52.76	
	Cell (3)	52.4	58.15			52.2	58.2			52.71	
Phase B	Cell (1)	52.2	58.12	174.42	348.22	52.0	58.4	174.3	290	52.898	348.08
	Cell (2)	52.4	58.16			52.4	58.1			52.579	
	Cell (3)	52.0	58.14			52.2	58.12			52.68	
Phase C	Cell (1)	52.2	58.13	174.45	348.13	52.4	58.18 87.12	116.33 174.15	290	52.613 62.44	348.24
	Cell (2)	52.0	58.10			52.2	58.15 87.03			52.69 62.5	
	Cell (3)	52.4	58.22			0	0			0	

*The values are varied based on the operational conditions, whether normal or transient, while the PV grid-tied system is under full shading circumstances.

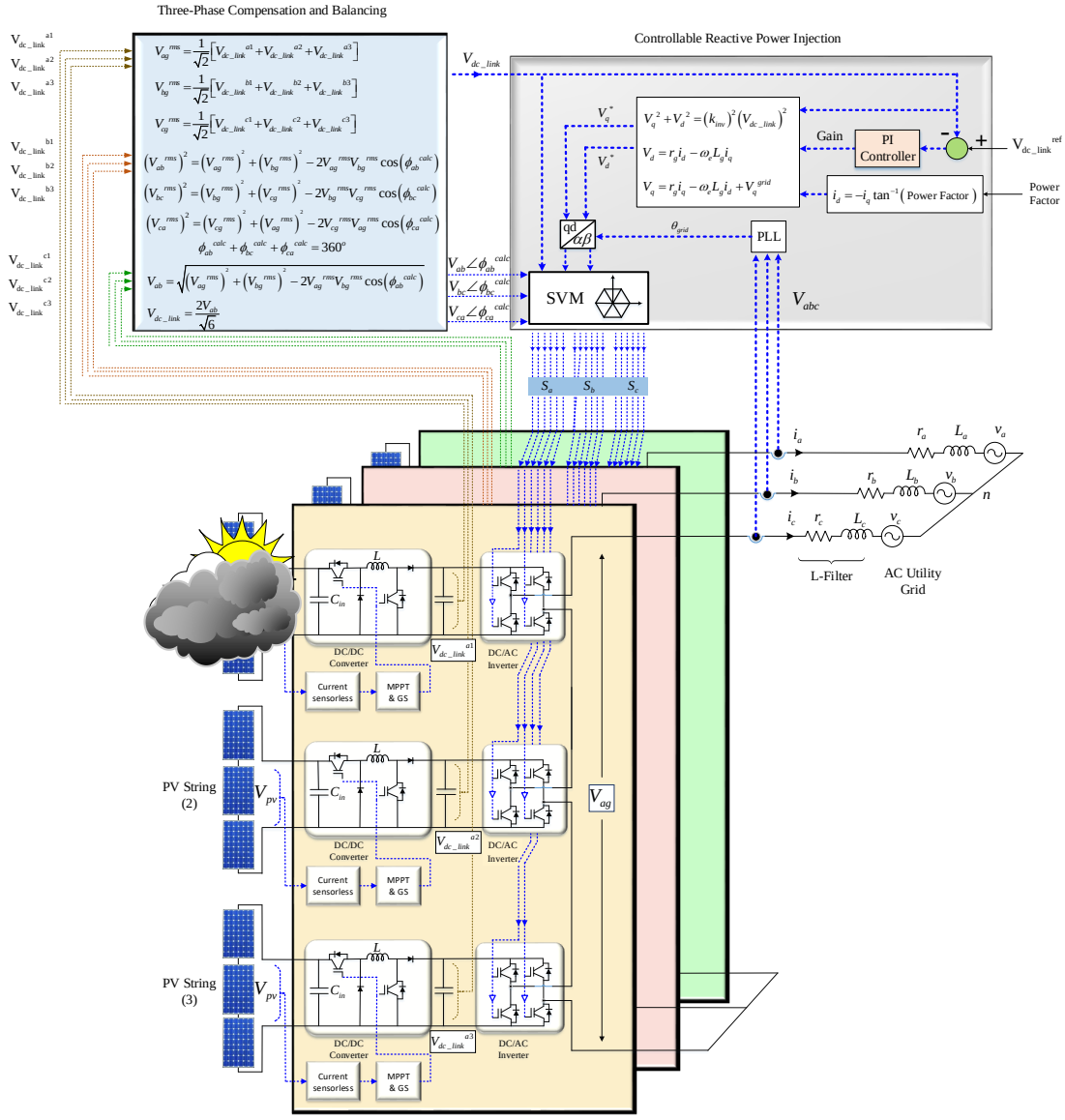

Figure 3.34: The PV grid-connected system schematic while experiencing severe partial shading

The new topology can first bring the PV system to the balancing conditions and reach equal line to line voltages and then gradually step up the DC link voltage to the reference DC link voltage. Figure 3.34 displays the PV grid-connected system under complete shading. The

fundamental phase shift compensation effectively rebalances the line to line voltages before boosting the DC link voltage and increasing the voltage amplitude to re-accomplish grid power injection.

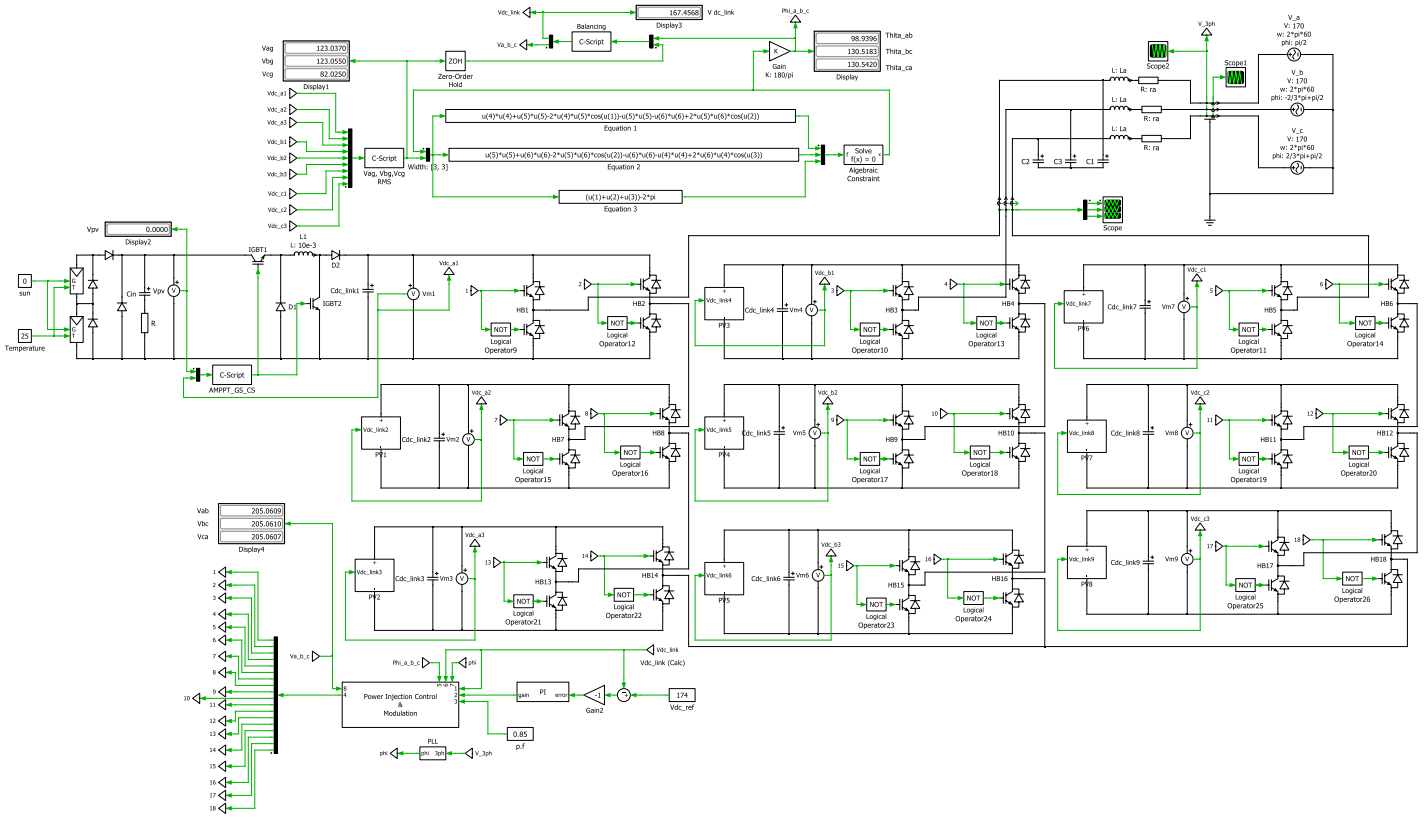

Figure 3.35: Complete PLECS schematic of PV grid-tied system connected through CHB

Figure 3.35 demonstrates the scheme of PV grid-connected system utilized by a PLECS simulation tool. Later, the proposed system starts gradually boosting the DC link voltages and the power injection is resumed by powering the rest of the unshaded cell. Once the PV system generates three phase voltages with a maximum peak higher than the peak of the grid voltage, power delivery into the utility grid will start but the amount of injected power is less due to the loss of fully shaded modules.

In conclusion, severe shading is the worst scenario of PV grid-tied systems due to the incidence of unbalancing and unequal line to line voltages which can lead to power delivery interruption. The special feature of a cascaded H-bridge converter is that each cell works independently. The new control can rebalance the three-phase line to line without turning the entire PV system off and continue supplying and injecting power into the AC utility grid. The fundamental phase shift compensation model is implemented to bring the line to line voltage to equalize the line to line voltages and avoid the PV grid-tied system from being kicked out before the DC/DC positive buck-boost starts boosting and increases the DC link voltage to the commanded DC reference voltage the same as the pre-shaded conditions. Table 3.6 provides the system data based PLECS tool model.

Table 3.6: Parameters of a PV System Connected to a Cascaded H-Bridge Converter

Parameters	**Values**
Nominal AC grid phase-to-neutral voltage and phase-to-phase voltage	V_{LN} (RMS) =120V V_{LL} (RMS)=208V
Nominal DC-link voltage	V_{dc_link} =174 V
Nominal AC frequency	f =60Hz
Rated power from PV generation	P=1200W
Inductance	L_{filter} =50 μH
Resistance	R=0.2 Ω

The obtained results from both approaches will be utilized for practical implementations of grid-connected PV system applications.

Chapter 4

4.1 Implementation Results of the Proposed Models

As this stage, two different outcomes of simulation and experimental results are obtained to verify, validate and fully understand the new introduced technique's performance. The results confirm the achievement of an efficient 99.8% proposed PV grid-connected system. In this chapter, every section shows the related results of models introduced in previous chapters. Therefore, section one presents the dynamic performance of three DC/DC converters: flyback, SEPIC, and positive buck-boost. Section two displays the experimental results obtained from the new adaptive maximum PV power extraction technique. The implementation of the introduced algorithm has been made easier with the advent of fast digital signal processors, FPGAs, and microcontrollers. The method introduces exceptional tracking and excellent performance. It validates and verifies experimentally with other well-known methods by generating various waveforms in different ambient weather conditions.

In section three, simulation results illustrate the performance for the proposed PV grid-tied system under partial shading as well as the obtained results of current sensorless. Next, it provides the power injection outcomes.

Finally, section four shows the waveforms of the PV grid tied system connected to the cascaded H-bridge converter. The overall results in this dissertation ensure the feasibility of applying such new proposed approaches for practical grid-tied solar PV system implementations.

4.1.1 Simulation Results of the Dynamic Performance

The first simulation results analyze three DC/DC converters: flyback, SEPIC, and positive buck- boost. Figure 4.1 illustrates the transient stability response of these converters after applying a small step change in each duty ratio while the converters are operating near the MPP. The result is verified by performing MATLAB simulation and PLECS add-on library.

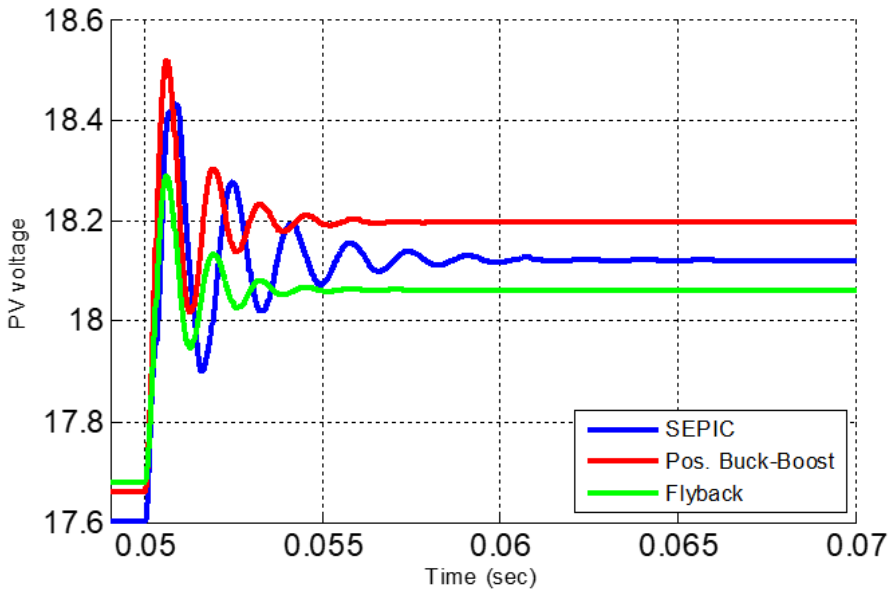

Figure 4.1: Step response of the three DC/DC converters to step change of duty cycle at MPP [139]

It can be clearly noticed that positive buck-boost has the highest overshoot response, SEPIC comes next, and flyback has lowest overshooting. Both positive buck-boost and flyback have shorter settling times and reach the steady state faster at 0.055 seconds, whereas SEPIC takes more time, exceeding 0.061 sec to stabilize. It can be seen that the three converters have the same

rise time.

Figures 4.2, 4.3, and 4.4 are related to the five operating points listed in Table 3.1. Likewise, three transfer function equations obtained in Chapter 3 are also exploited to verify the dynamic response of the three DC/DC converters in both transient and steady states.

Figure 4.2 illustrates the dynamic performance of SEPIC in five operating points. According to the obtained result in Figure 4.2, the input voltage oscillates when the operating point is at power region I and the input voltage is being harshly distorted in the current-source region since the SEPIC phase plot drops below -180^{o} as shown in Figure 4.5. Otherwise, the SEPIC exhibits perfect dynamic performance at the rest of the operating points including the maximum power point.

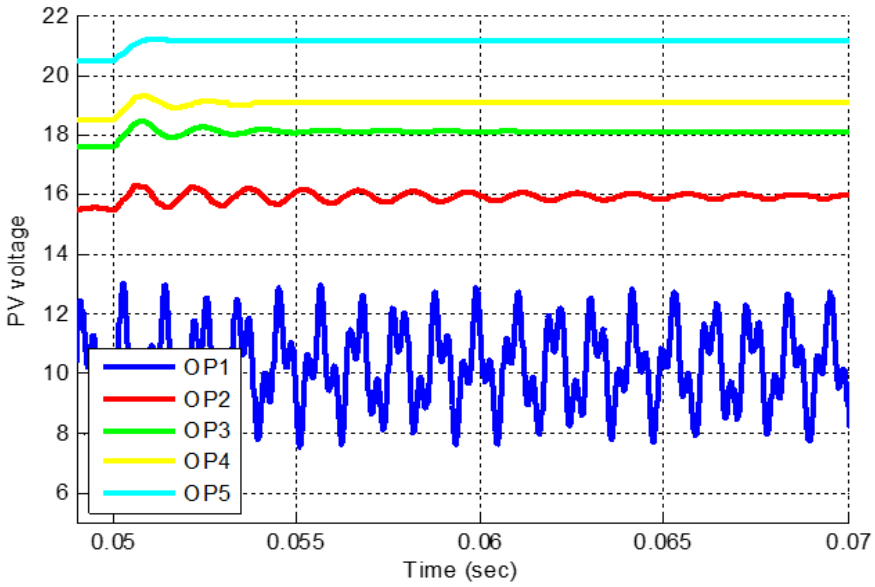

Figure 4.2: Response of SEPIC to a step change of duty cycle in the four power regions and MPP [139]

Figure 4.3 shows the resulting waveforms of dynamic performance of the positive buck-boost converter. The dynamic response refers to the operating points listed in Table 3.1. The performance displays a robust stability margin compared to previous responses and converges faster at the

voltage set. Per the outcome results, the positive buck-boost is more stable and only oscillates in a range of $\pm 2V$ which is reasonable in the current source region.

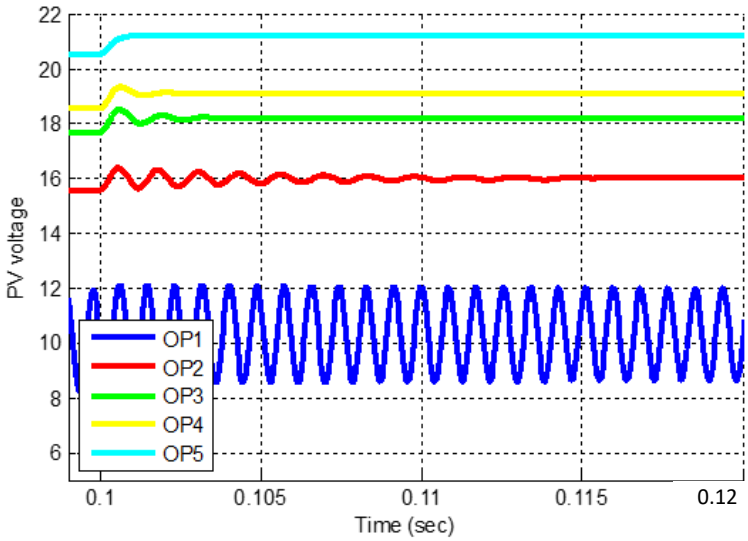

Figure 4.3: Response of a positive buck-boost to a step change of duty cycle in five P-V regions [139]

Figure 4.4 verifies the relative distinction of the flyback in terms of dynamic performance. The converter shows a similar behavior to the positive buck-boost.

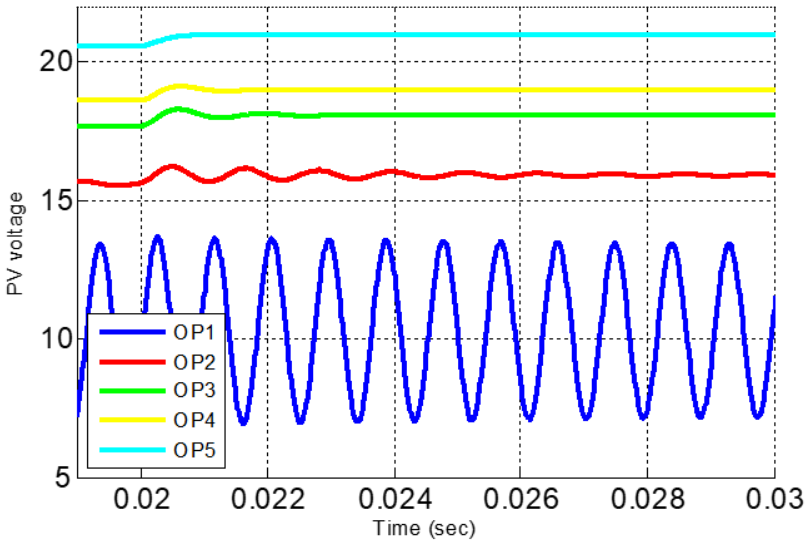

Figure 4.4: Response of flyback to a step change of duty cycle within five P-V regions [139]

However, the flyback has a wider range of oscillation (±4V) when it operates in the current source region.

Figure 4.5 applies Bode plots to obtain an open loop frequency response from SEPIC, positive buck-boost, flyback. The plot illustrates the three converters when the operating point is exactly at the maximum power point. The Bode plots confirms that all the converters are stable. The SEPIC shows a bump before -180^{o} since it contains two complex conjugate pairs of poles and one complex conjugate of zeroes. As a result, designing a controller is complicated because the controller gain crossover frequency is shifted to a frequency much lower than the bump's frequency.

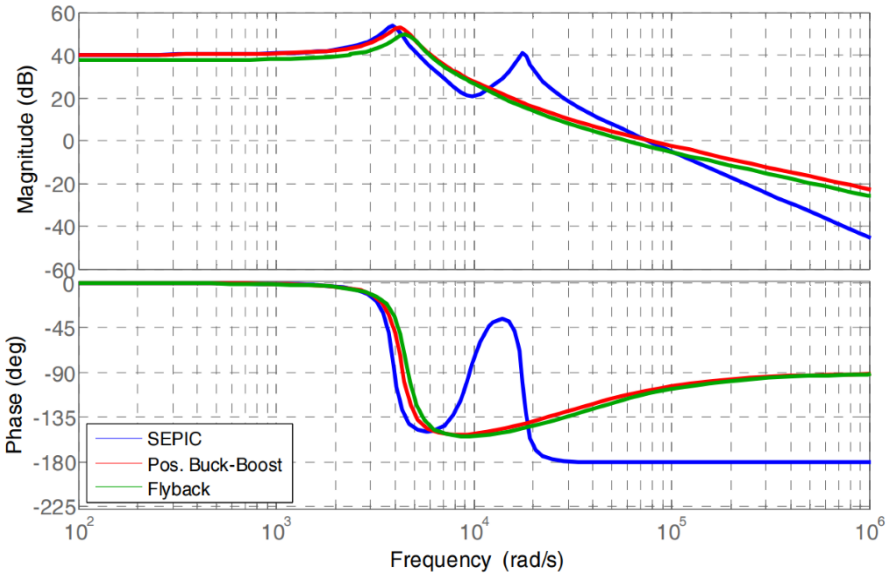

Figure 4.5: The open-loop frequency response of the three selected converters at MPP [139]

The response shows the transient response of the closed loop will be relatively slow. The phase plots of the positive buck-boost and flyback converters always maintain at positive since both converge to -90^{o} This means the phase margin increases while increasing the closed loop gain. Therefore, the closed loop system for each converter can be designed to achieve fast

responses under a high degree of stability. The upper limit of gain in this case will be limited according to the saturation of duty cycle (control signal) as shown on the theoretical formulas obtained in Chapter 3.

4.1.2 Experimental Results of the Proposed MPPT method

The actual experimental lab setup of the system is shown in Figure 4.6. The experimental setup contains a PV module emulator, the nominated positive buck-boost power converter, a digital controller, and two 12V batteries. Both are connected in a series to serve as a 24 V battery.

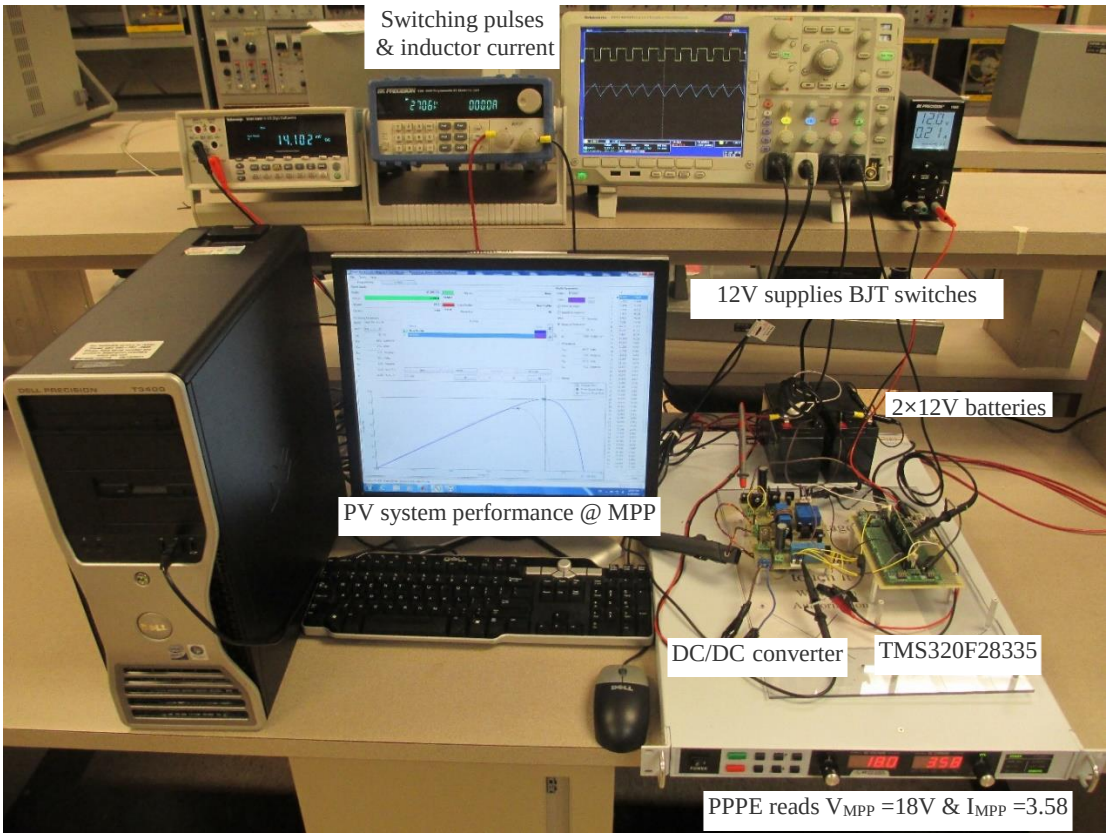

Figure 4.6: The experimental setup of the standalone proposed system

In the university laboratory, a solar array emulator is repeatedly used to emulate the behavior of a PV solar module. The BP365 is selected to utilize a PV module. It is a silicon nitride

multi-crystalline 65 W PV-module by BP solar technology. The specifications of the PV module in the standard test condition (STC) are as follows:

k_v=-0.32 %℃, k_i=0.065 % ℃, P_{max}=65 W, Voc=22.1 V, V_{mpp}=17.6 V, I_{mpp}=3.69 A, I_{sc}=3.99 A.

SL100 programmable DC power supply is the solar array emulator with an accompanying Windows-based software called Photovoltaic Power Profile Emulation (PPPE), by Magna-Power electronics. The PPPE reads the parameters of the PV panel and controls the DC power supply so that it imitates the P-V curve and I-V characteristics curve of the PV module.

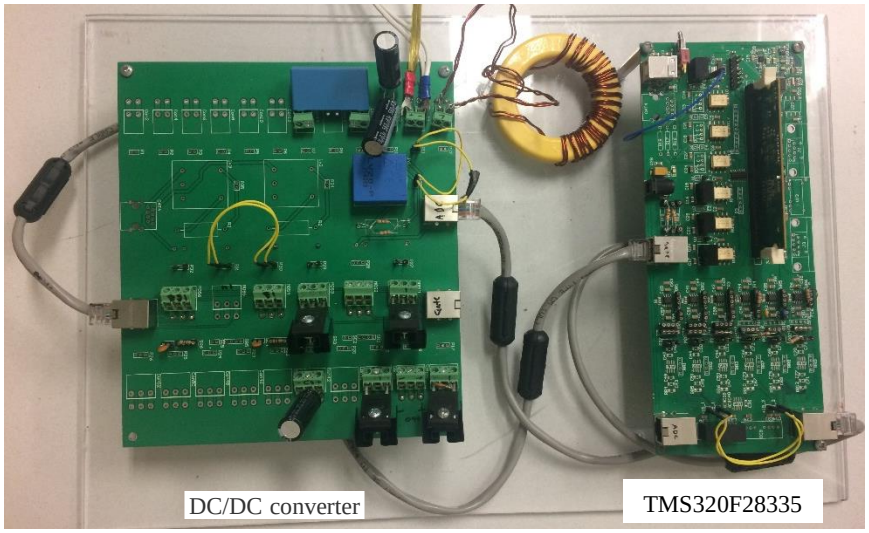

Figure 4.7: The prototype of power and control stages of the PV standalone system

Figure 4.7 displays both a prototype of the power and control stages. The power stage is on the left side and contains DC/DC converter (positive buck-boost). It is designed under these criteria, where $P_{in} = P_{out}$=300 W, PV input voltage V_{in} varies in a range of (0 – 22 V). The parameters of the positive buck-boost converter are: Inductance L=50μH, input capacitor is C_{in} =560 µF, and the switching frequency is $f_{s\omega}$=100 kHz.

The right side is the control stage and consists of amplifiers for low-level voltage regulation and to adjust and adopt the input signals from both PV voltage and current sensors to the microcontroller. A TMS320f28335 is the selected digital signal processor (DSP) from Texas Instruments, which is utilized to implement the new maximum power harvesting strategy. An I/O board has the voltage and current sensors and gate driver circuitry which is designed to accompany the DSP.

Typically, the new PV harvesting strategies are measured and evaluated based on response speed, convergence accuracy, tracking precision, and the range of oscillations around the maximum power peak. Indeed, a fast, dynamic response is extremely significant criteria under the continuing variation in the ambient temperature and irradiance levels.

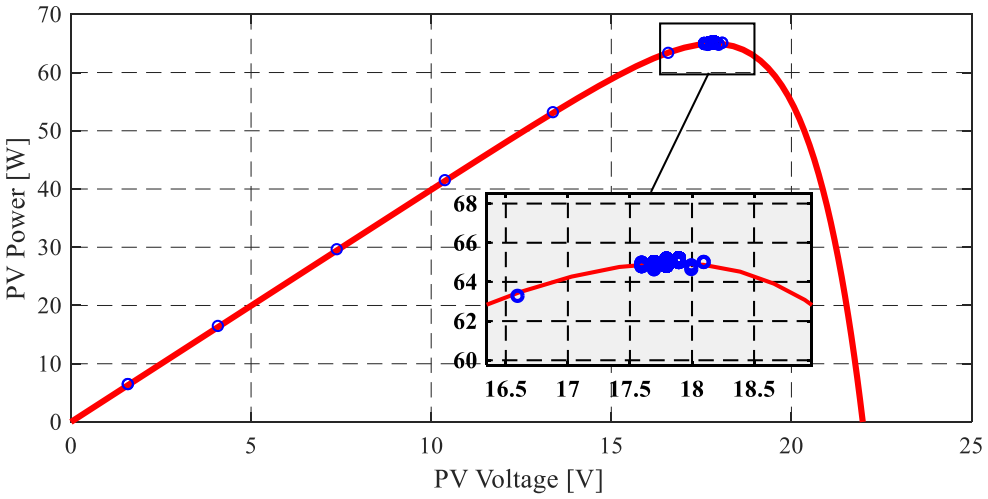

Figure 4.8: Startup of the proposed approach on P-V curve

Figure 4.8 shows an experiment result of startup performance on P-V curve. The outcome is related to the PV module BP365 under standard test conditions (STC) where the ambient temperature is set to 25℃ and 1000 W/m^2 for the local irradiation. According to this Figure, the converter is started by stepping up the power adaptively based on the new power prediction

approach to track the maximum power peak. It illustrates that the climbing steps are wider to reach the maximum power peak more quickly and then converges precisely with negligible variation amplitude around the power peak. This indicates that the new strategy avoids the transient states and evades spending undesired time but accelerates to the targeted maximum power-point peak. Therefore, the figure shows that the experimental implementation of the PV system acts efficiently like the designer view and guarantees the effectiveness of the new approach.

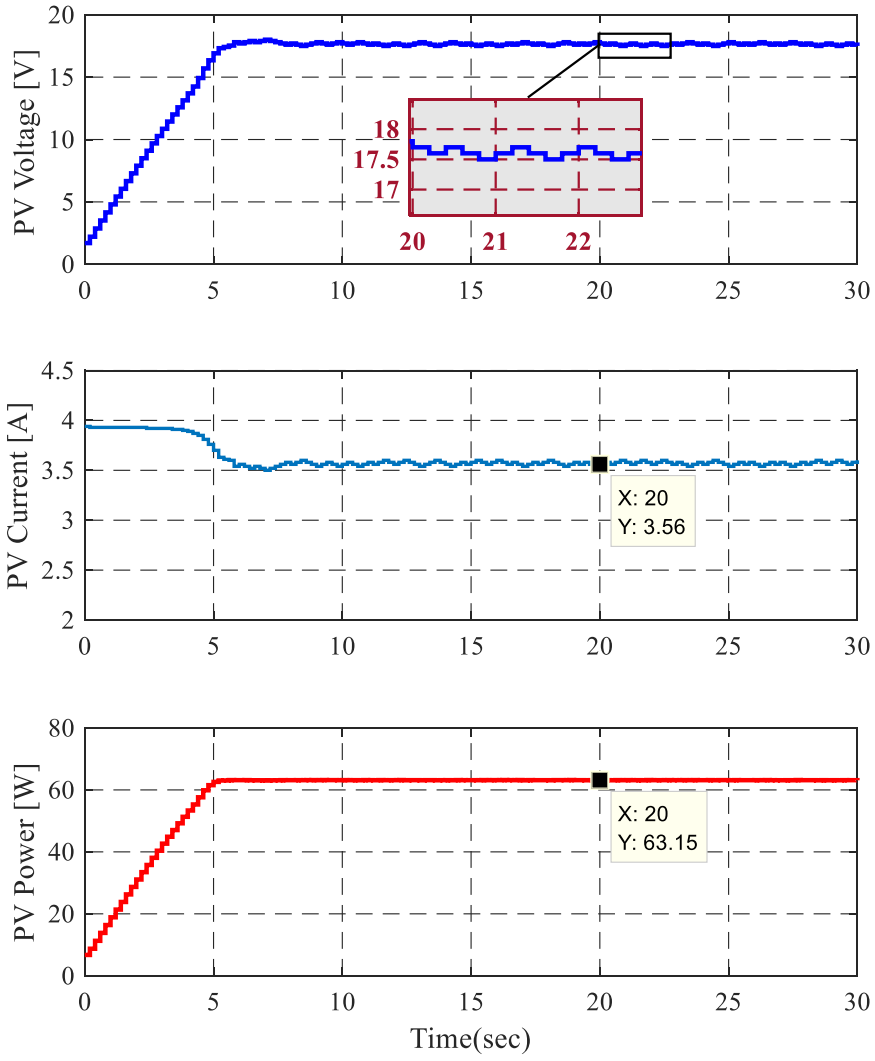

Figure 4.9: Startup performance of PV voltage, current and harvested power via proposed approach

Figure 4.9 shows in detail the previous operating characteristics of the experimental setup while the PV system starts up. It provides how closely the introduced technique performs with respect to PV input voltage, current, and extracted PV power individually. Consequently, the PV input voltage oscillates between 17.7 V to 17.6 V, while the PV input current converges to 3.56 A, and the captured power provides 63.15 W. Moreover, the settling time takes exactly 5.0 seconds to converge.

In Figure 4.10, two P-V characteristic curves of the BP365 are shown for two different temperatures: 25℃ and 50℃. This shows the results of PV input voltage versus harvested PV power on the P-V characteristic curve by using the new harvesting strategy. The ambient temperature of the PV module is set initially to 25℃ and then varies up to 50℃ before switching back to 25℃ after 30 seconds.

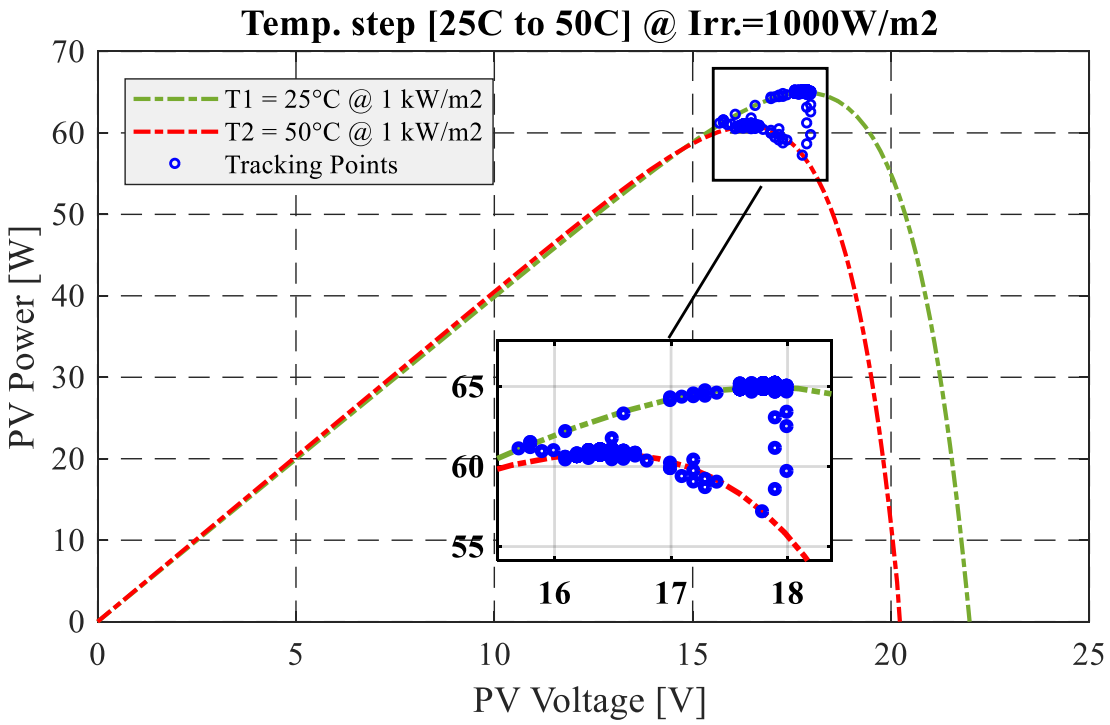

Figure 4.10: Dynamic performance on P-V curves (voltage vs. harvested power) when temp. step change

The PV voltage is nearly constant at 17.6 V when T=25℃ and 16.5V at 50℃ and repeatedly throughout this experiment. Every tracking point captured on the P-V curve represents the real tracking behavior and all real operating points were obtained from the PV emulator while tracking the maximum power point experimentally. The PV emulator has an option where all data points can be generated and saved in an Excel file that contains all operating points.

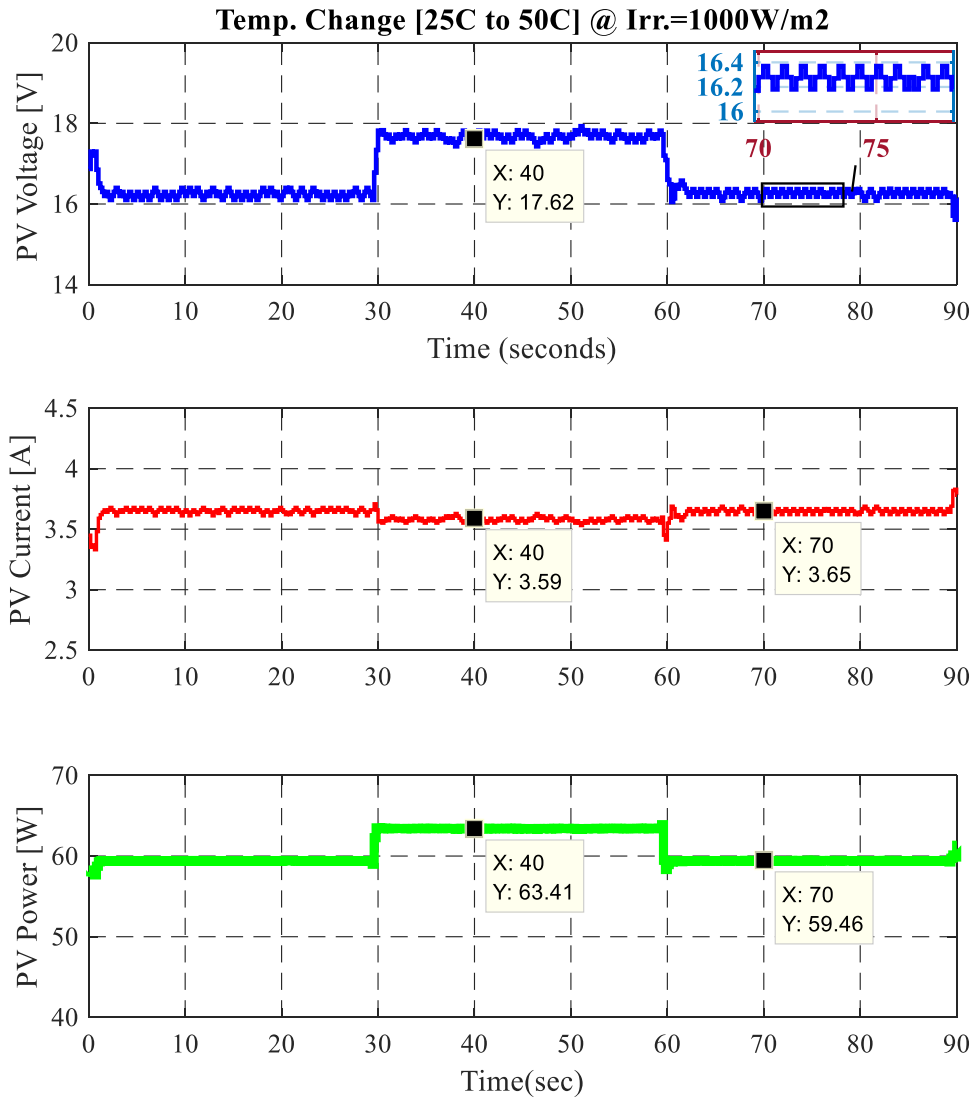

Figure 4.11: Step response when temperature varies from 50℃ to 25℃ and then to 50℃

Figure 4.11 depicts the dynamic response to the variations in ambient temperature and shows the effect of temperature step change in the input voltage, input current, and extracted power versus time. In this experiment, the PV system reacts successfully to track the operating point to the new accurate power peak, while sun illumination is kept constant at 1000W/m^2. The scenario imitates a real physical incident when ambient temperature around the PV modules is unexpectedly varied due to a change in the ambient weather conditions for a long or short period of time.

Nevertheless, it can be clearly noticed, that whenever the temperature raises up, the PV input voltage drops. As a result, the captured PV power decreases and vice versa. However, the PV input current raises slightly when the ambient temperature increases too. The drop-in panel's voltage while the ambient temperature increases is referred to as temperature coefficient in the panel manufacture's specification. Typically, in traditional modules made from silicon, temperature coefficient varies between -0.4 to -0.5%. In thin film panels, it ranges from -0.2 to -0.3%. Eventually, other modules made from crystalline materials have a positive temperature coefficient which means they exhibits highly efficient performance as the temperature increases but they are very expensive.

Figure 4.12 illustrates time versus input voltage, input current, and generated power, respectively. The figure presents the response of the proposed method when the ambient temperature regularly drops from 50℃ to 25℃ and then increases gradually again to 50℃. Similarly, the proposed algorithm validates the robustness against the changes in temperature, acts faster, and accurately and effectively traces the operating point to the desired peak.

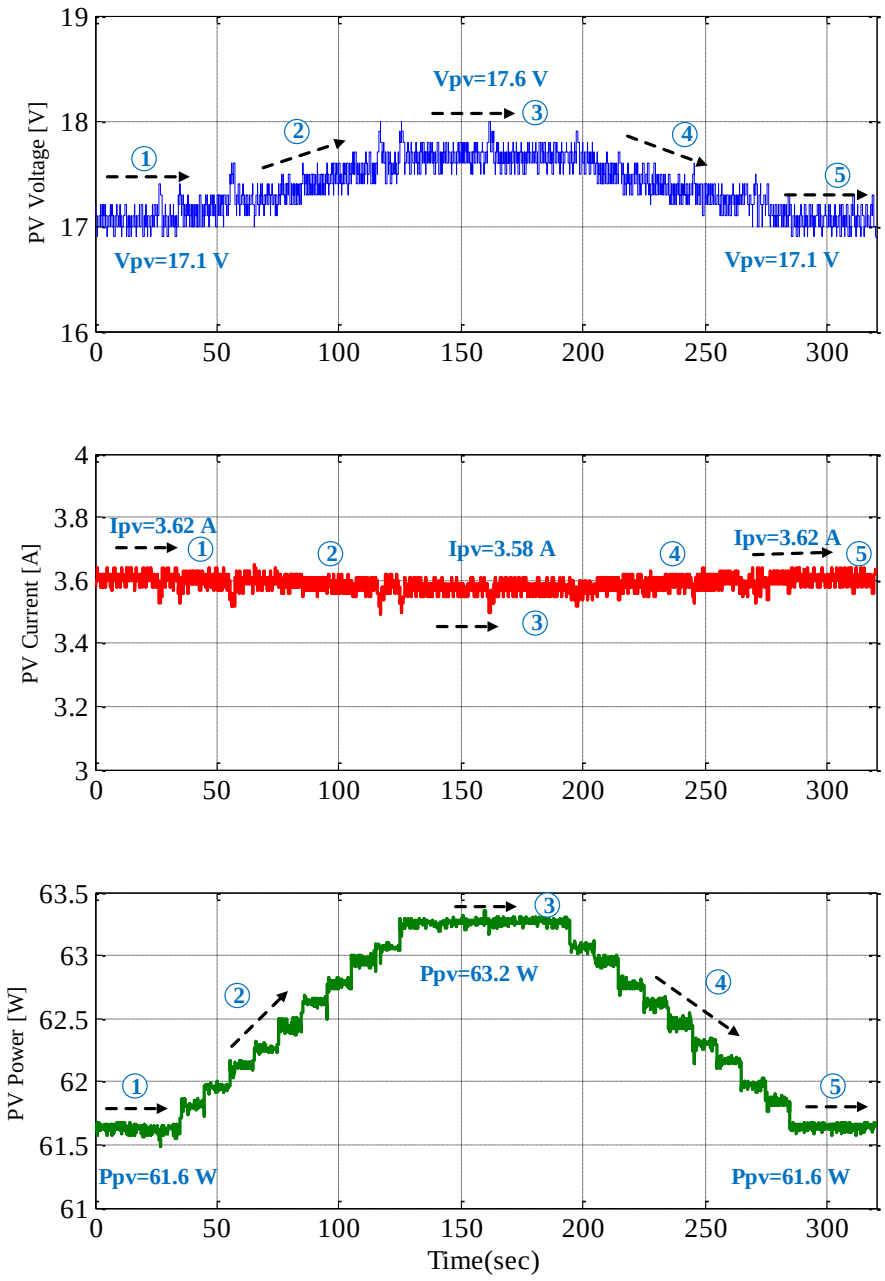

Figure 4.12: The response to gradual temperature increases from 25℃ to 50℃ then to 25℃ [140]

Figure 4.13 is as same as Figure 4.12. The only difference is that the operating time is extended under the same ambient temperature i.e., it gradually rises. As shown, the proposed approach maintains strictly the operating point of the PV module at the target maximum available power peak.

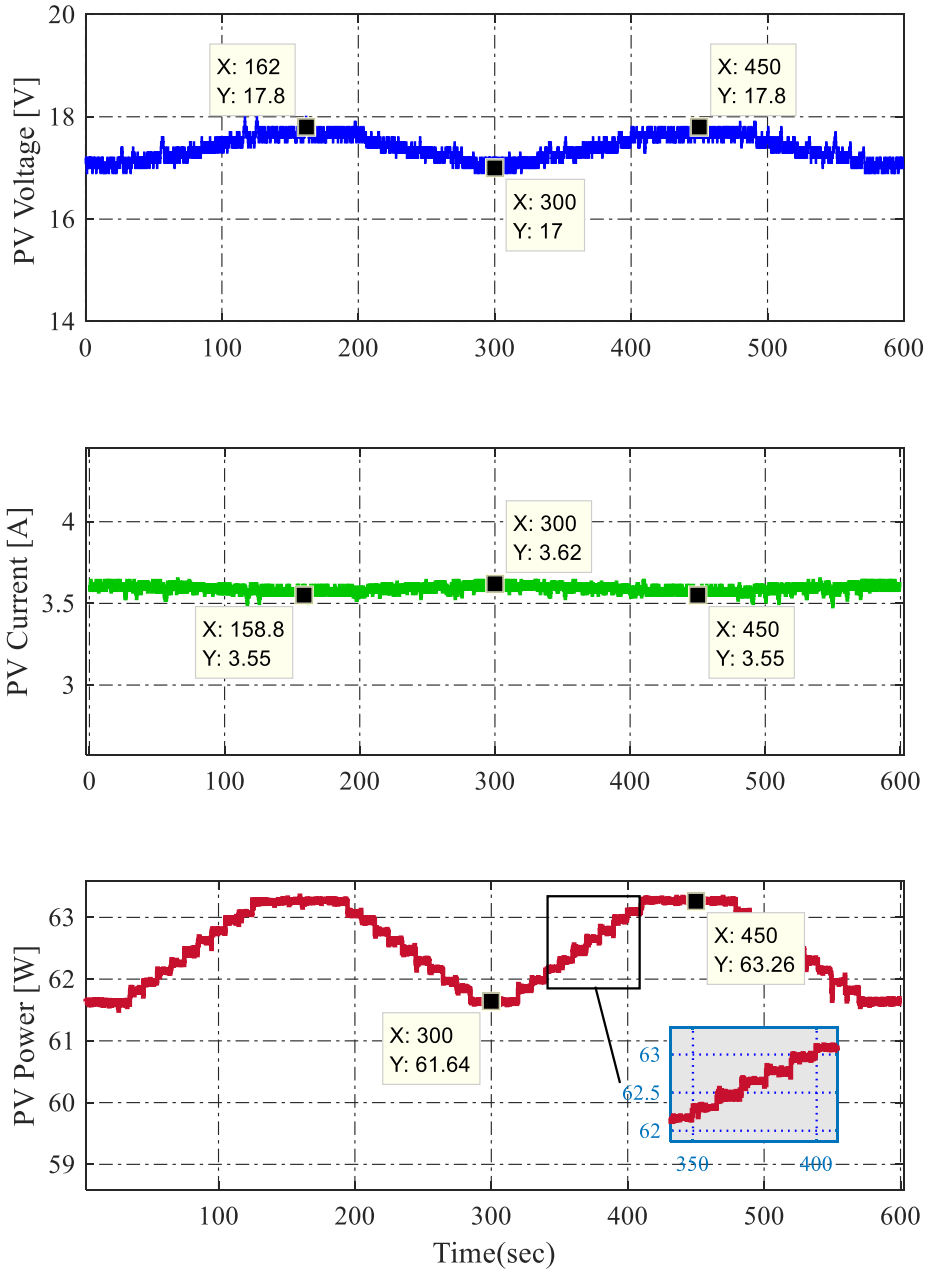

Figure 4.13: Operating time extended when temperatures gradually change from 50℃ to 25℃

The next reported result is an experiment on behavior of the PV generating system when the temperature is kept constant at 25℃ while the sunlight irradiance is varied. It starts going up

slowly from 800 W/m^2 and holds at 1000 W/m^2. Figure 4.14 demonstrates the transient response of the PV system due to a gradual change in sun illumination. As presented, the PV input current generated by solar cells is a function of the amount of irradiance that hits the PV panels' surfaces. Thus, the more irradiance that hits the panels, the more current will be generated, which goes up to the cell's material's limitation.

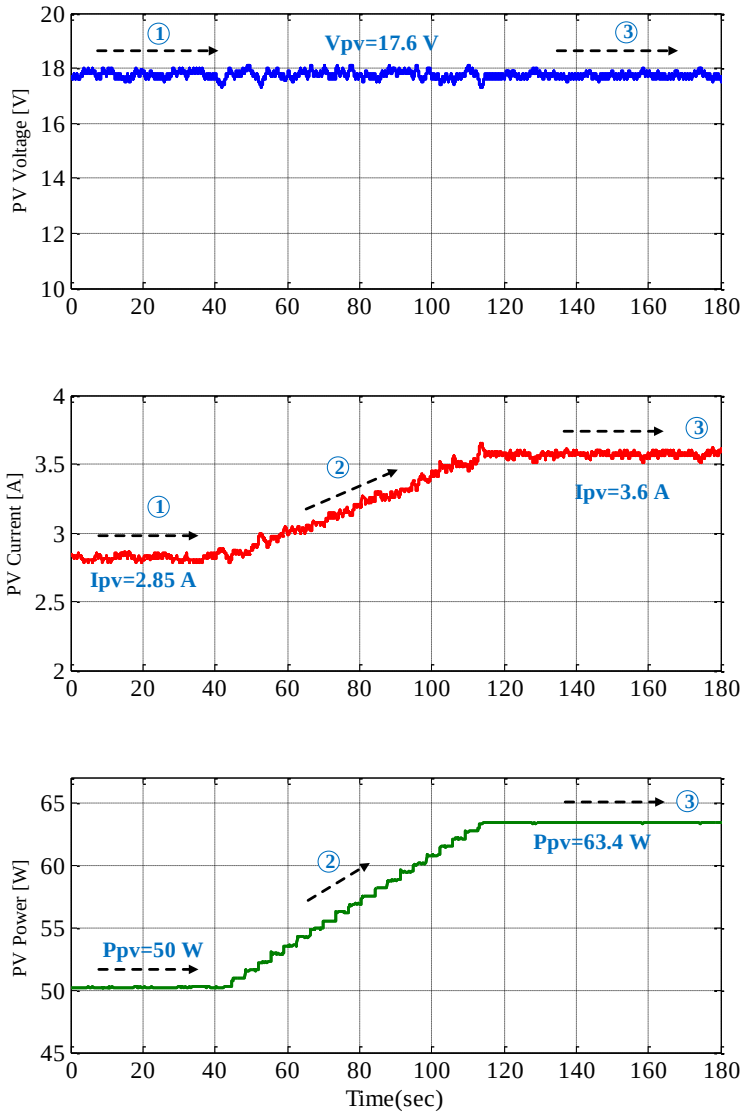

Figure 4.14: PV voltage, current and extracted power while irradiance gradually changes [140]

It is obvious that as long as the gradual change is in the level of local irradiance received by the PV module surface; it occurs directly on the PV current. It begins from 2.85 A at 800 W/m^2 and raises up gradually to I_{MPP} =3.6 A at 1000 W/m^2. Nevertheless, the PV input voltage keeps fluctuating slightly at V_{MPP} =17.6 V.

The next section is a comparison attempt to verify the operation of the new presented methodology and its performance as well as the objectives of introducing the method. A comprehensive comparison with respect to well-known traditional methods are investigated experimentally using the same described experimental setup in Figure 4.6.

4.1.3 Comparative Analysis of the Experimental Results

Figure 4.15 is included to present preliminary simulation results of the proposed PV solar energy to validate the proposed method in terms of its rapid response to dynamic environmental

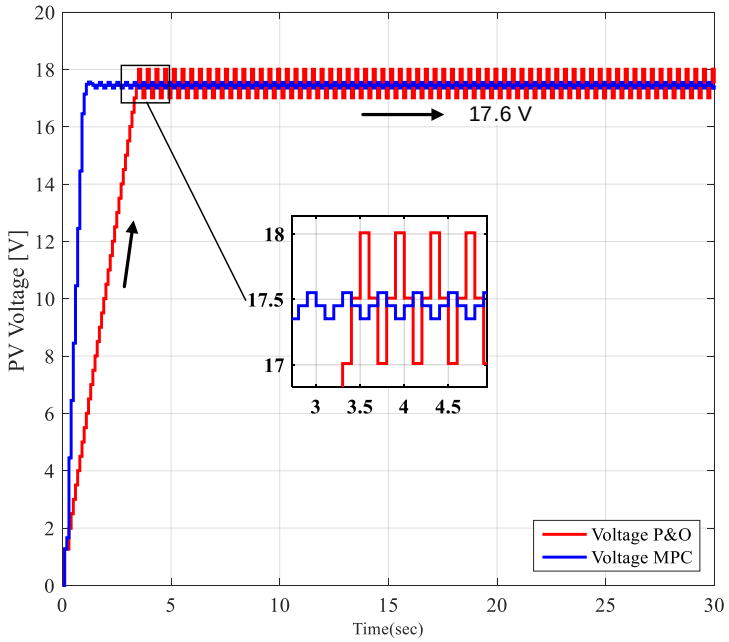

Figure 4.15: The startup performance of the proposed method compared with the P&O method

conditions. It demonstrates the operation of the proposed method during startup and displays the effect varying the climb step has on dynamic reaction. The larger climb step increases the speed of convergence for the traditional P&O technique to converge faster, but it ultimately makes the oscillatory states around the maximum peak much larger. Thus, the adaptive step in the introduced method offers additional flexibility to the predictive control to act properly beyond one step ahead (k+1).

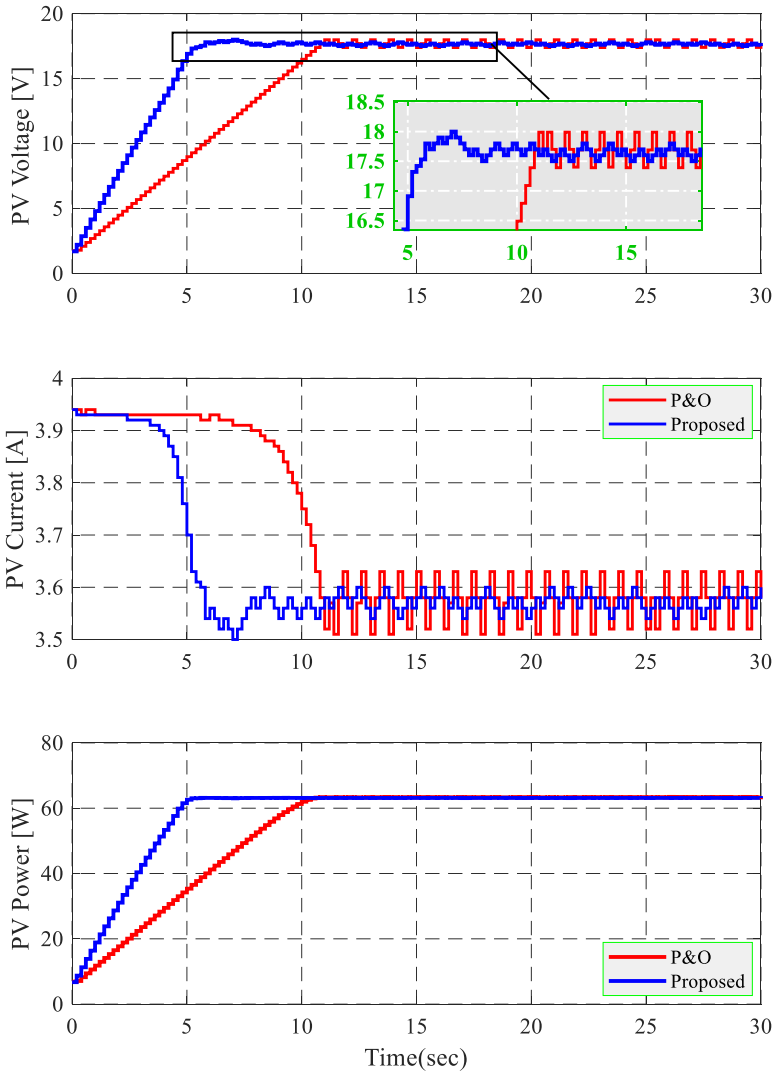

Figure 4.16: The startup performance of the proposed method compared with the P&O method [140]

The oscillatory states in traditional P&O can easily be a reason for failure or unwanted swings while the system faces a transient status. It leads to confusion in locating the MPP. However, the new technique has the feature of prediction schemes corroborated by adaptive climb step change to start up faster and then the step is reduced to exhibit less fluctuation convergence as appears in PV voltage and current waveforms. Figure 4.16 gives the experimental performance of startup behavior.

After the comparison of the startup performance to validate the response of the new PV power harvest method, the temperature step change is also compared to the traditional P&O. This is an attempt to check the response to expected dynamic environmental conditions experimentally. In Figure 4.17, the PV panel is set to the level of delivered irradiance fixed at 1000 W/m^2 while the temperature is changed from 25℃ to 50℃. The scenario matches possible sudden fluctuations in ambient daytime temperatures. It confirms the real experimental result of the proposed strategy compared with P&O. As represented, the introduced strategy exhibits fewer oscillations around the power peak point in the steady state condition. The PV voltage converges to 16V in both methods, but the P&O oscillates more. Once the temperature step change appears, the new PV harvesting approach responds instantly which presents the effectiveness of introduced such algorithm and the features of prediction control in addition to enhancement from the adaptive step. It converges exactly at the new peak as given on the panel's specifications. As depicted, when the temperature drops back again, the new presented algorithm reacts as expected; however, P&O is tricked into increasing the voltage and thus the PV current deviates and drops deeply to 2.8 A, which causes a significant power drop of 51.5 W. Therefore, the P&O method shows significant impact to sudden temperature changes while it starts to converge back to the new maximum after

having struggled to locate the new peak.

In addition, the outcome displays that the traditional P&O technique creates an unavoidable delay before making the right decision, which leads to an inexact transient performance. The new PV harvesting method generates a control signal that continuously dictates the new operating point to the true location precisely and possesses a rapid response regardless of ambient environment variations to emphasize a robust balancing.

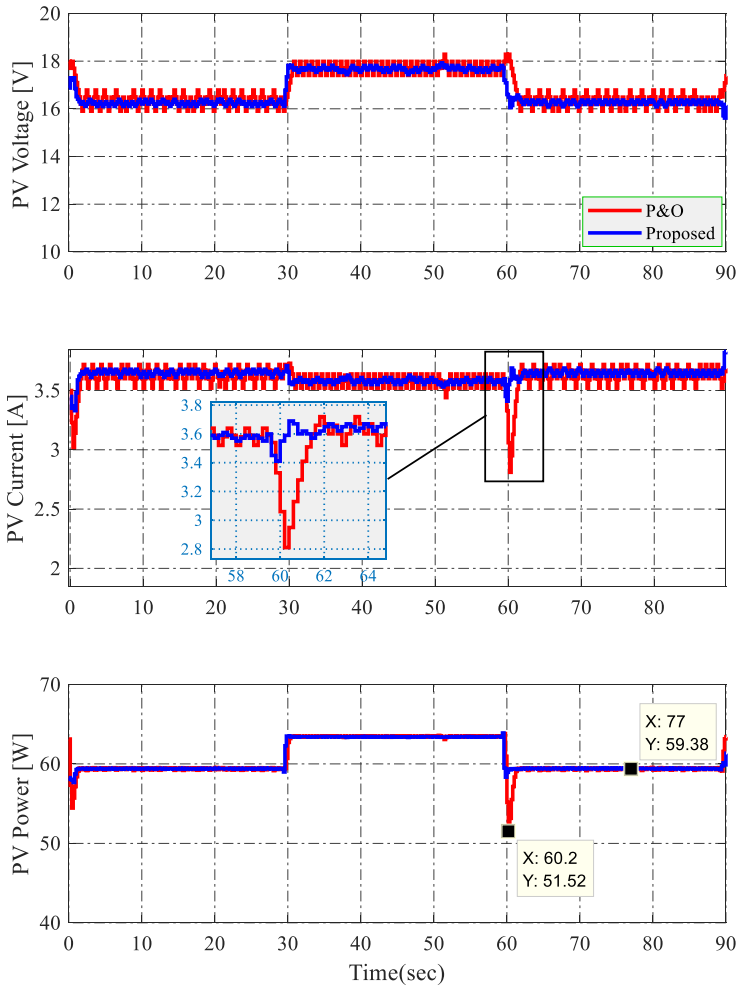

Figure 4.17: Step response of the two methods in case of a PV temperature step from 25℃ to 50℃.

Next, a comprehensive comparison of five selected techniques along with the proposed method are illustrated to verify and evaluate the performance experimentally. The experimental

results for the five PV power tracking techniques are depicted to provide realistic validity. All the shared parameters and ambient weather conditions were applied equally to perform a fair comparison between the candidates' techniques. The irradiance is constant at 1000 W/m^2, but the temperature starts at 25℃ and goes up to 50℃ for 30 seconds and then steps down back to 25℃.

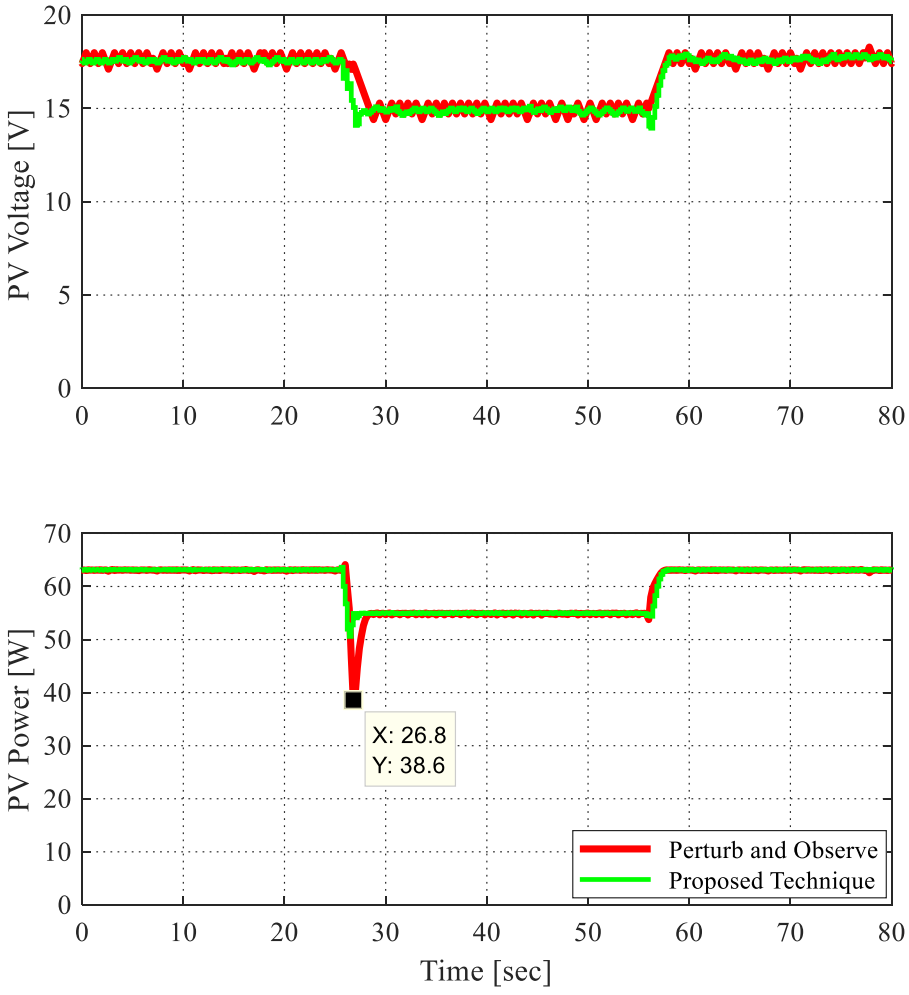

Figure 4.18: PV voltage and harvested DC power using the perturb and observe technique

The generated results can be compared on different serious factors; for instance, fluctuations around the desired power peak at steady-state operation, response to ambient change, speed of convergence, and detection of tracking weakness. Figure 4.18 shows that the traditional

P&O method exhibits an unavoidable 1.0 V range of oscillation and converges to the maximum desired point in 2.0 seconds after step-up direction and 3.2 seconds in step-down direction. The new PV harvesting energy method appears to produce an excellent performance tracking.

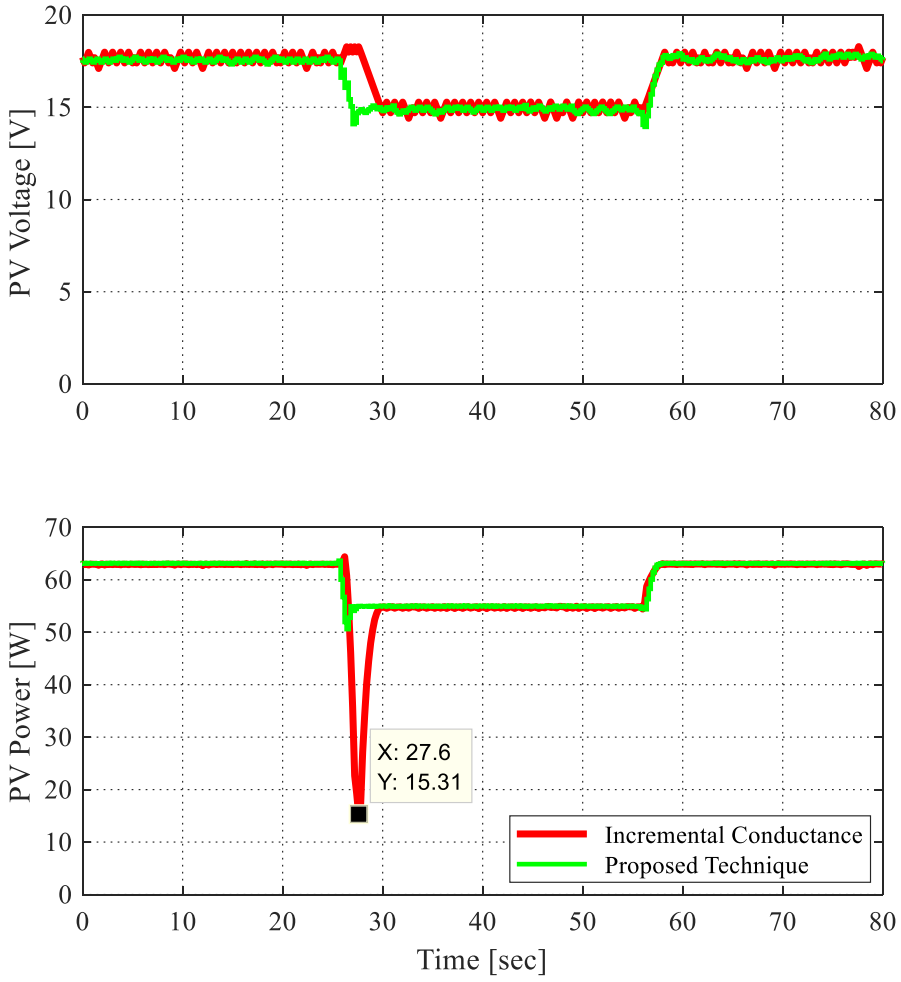

Figure 4.19: PV voltage and harvested DC power by incremental conductance technique

It addresses and mitigates the transient tracking when experiencing step change in the ambient temperature. It has negligible oscillation range and convergence takes 1.8 seconds in step-down and 2.0 seconds in step-up. Moreover, the power drop is 20 W, which is a 29.8% drop, while the new method drops only 5 W, or 0.9%. For the same incident, the incremental conductance strategy exhibits 2.2 seconds in step-up and 4.4 seconds in step-down. However, it takes nearly

2.4 seconds for the estimated perturb-perturb method to converge in the step-up direction and 4.2 seconds in step-down. Further, the power drop is twice that of conventional P&O, which is a vast performance deterioration.

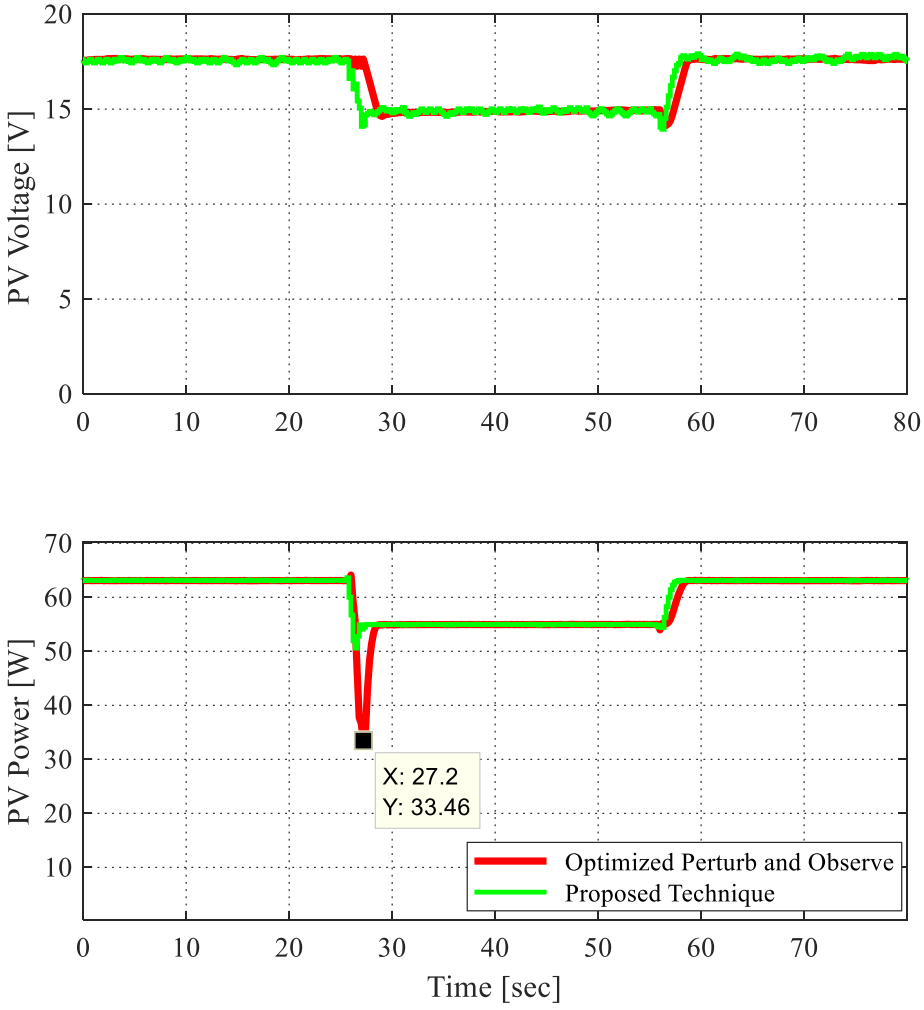

Figure 4.20: PV voltage and extracted DC power by the optimized perturb and observe technique

The optimized perturb and observe strategy has 3.0 seconds convergence time in the step-down direction; however, surprisingly it has a slow response, 2.5 seconds, in the step-up direction. In terms of oscillations around the maximum peak, the optimized perturb and observe approach seems to have the advantage over all other approaches, while the incremental conductance seems

to be the worst of the four in terms of the power drop even though it is the developed version of perturb and observe. The oscillation values that were generated in the perturb and observe, incremental conductance, and estimated perturb-perturb are shown in Table 4.2.

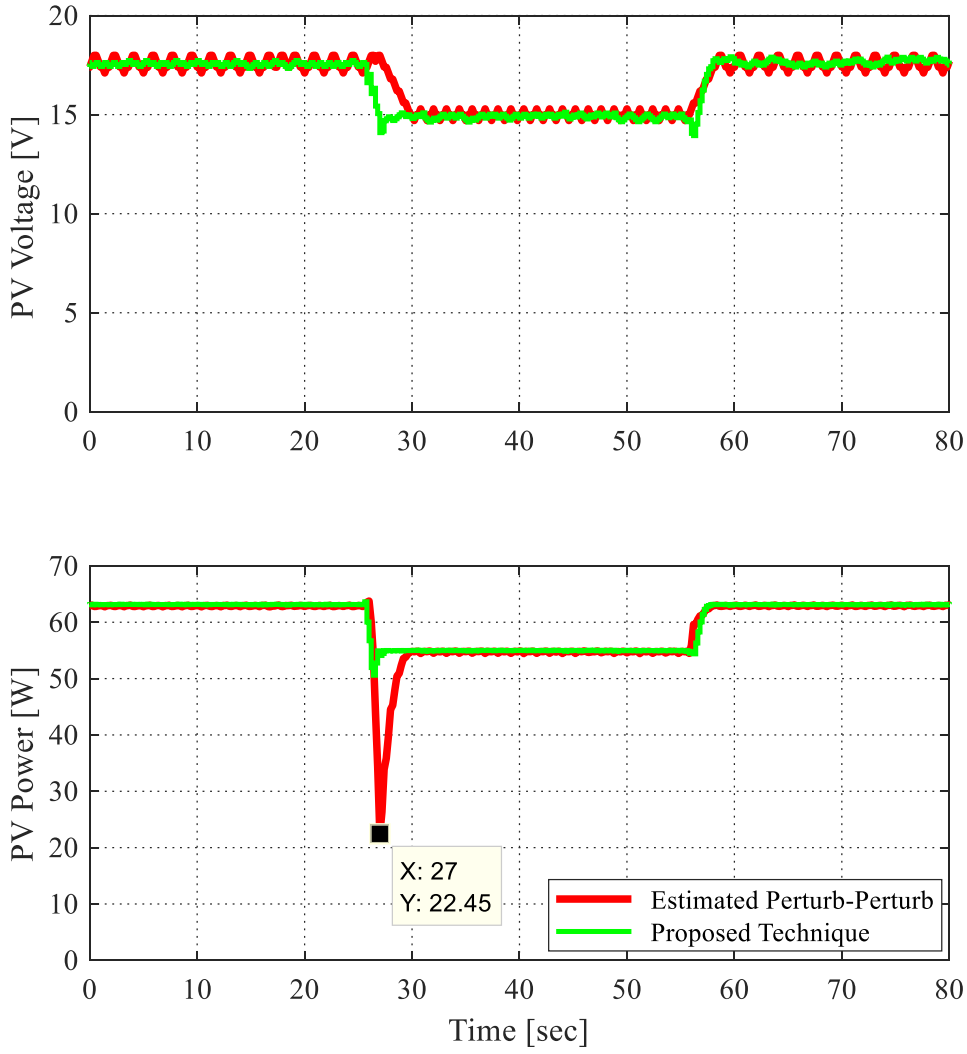

Figure 4.21: PV input voltage and the extracted DC power by estimated perturb-perturb technique

The behavior of the available harvesting techniques shows that when the techniques get confused and are tricked into increasing the voltage, power drops occur. The more time spent on false tracking, the more severe the power dip will be. The time delay on tracking the power peak is because the methods need more samples to make the right decision.

On the other hand, since the selected DC/DC converter is positive buck-boost, the first step before comparing the approach with fuzzy logic control is to build the lookup table accordingly. It is only suitable for DC/DC converters with the same voltage transfer ratio. However, converters such as positive buck-boost have different tables on account of the voltage characteristic ratio.

Table 4.1: Lookup table of rules base of positive buck-boost

ΔV \ ΔP	NB	NS	ZO	PS	PB
NB	PB	PS	NS	NS	NB
NS	PS	PS	NS	NS	NS
ZO	NS	NS	ZO	PS	PS
PS	NS	NS	PS	PS	PS
PB	NB	NS	PS	PS	PB

Figure 4.22 confirms the proposed method with respect to the fuzzy logic method. To highlight the new algorithm effective tracking, temperature step change is applied twice. Based on the experimental results, it can be concluded that the PV module can deliver the maximum power; however, the performance of the new strategy is better than the sophisticated method. It has multiple parameters that need to be set and adjusted carefully; otherwise, the tracking decision can easily get confused. In summary, fuzzy logic control has wider range of control capability, but more time is required for trial and error learning, which is a common approach used while tuning the process for proper control decisions. As depicted, the method tries to keep the PV system at good standing at maximum power delivery under the change in ambient temperature. It takes 5.2 seconds in step-down and 4.0 seconds in step-up.

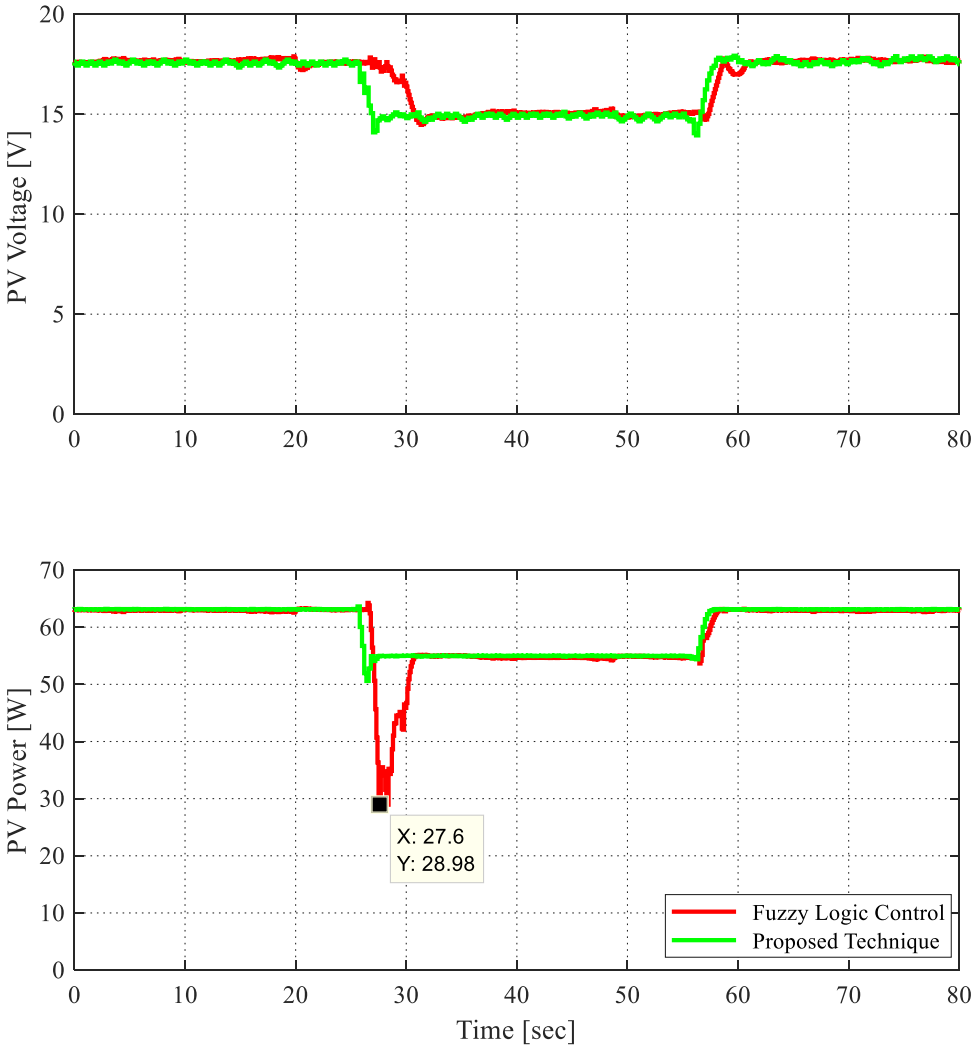

Figure 4.22: PV input voltage and extracted DC power by the fuzzy logic control technique

Further, comparative analysis and another configuration of experimental results using the tracking efficacy between the introduced strategy with two special methods. Figure 4.23 compares optimized P&O with new techniques and Figure 4.24 compares the new algorithm with fuzzy logic, which is a sophisticated method with a high complexity of computational process. The tracking strategies assist indirectly in reducing harmonic ripples, which is a problem of the power quality of the PV grid-connected systems as well as preventing power drop. Thus, they have to avoid tracking failure while searching on the maximum power point. The figure shows that the

output power effectively reach the maximum point based on the new designed model of maximum power tracking with less oscillation and neglected power drop. However, the efficacy of optimized P&O falls to 60.83% at the abrupt change and takes a duration of 4.4 seconds to converge properly.

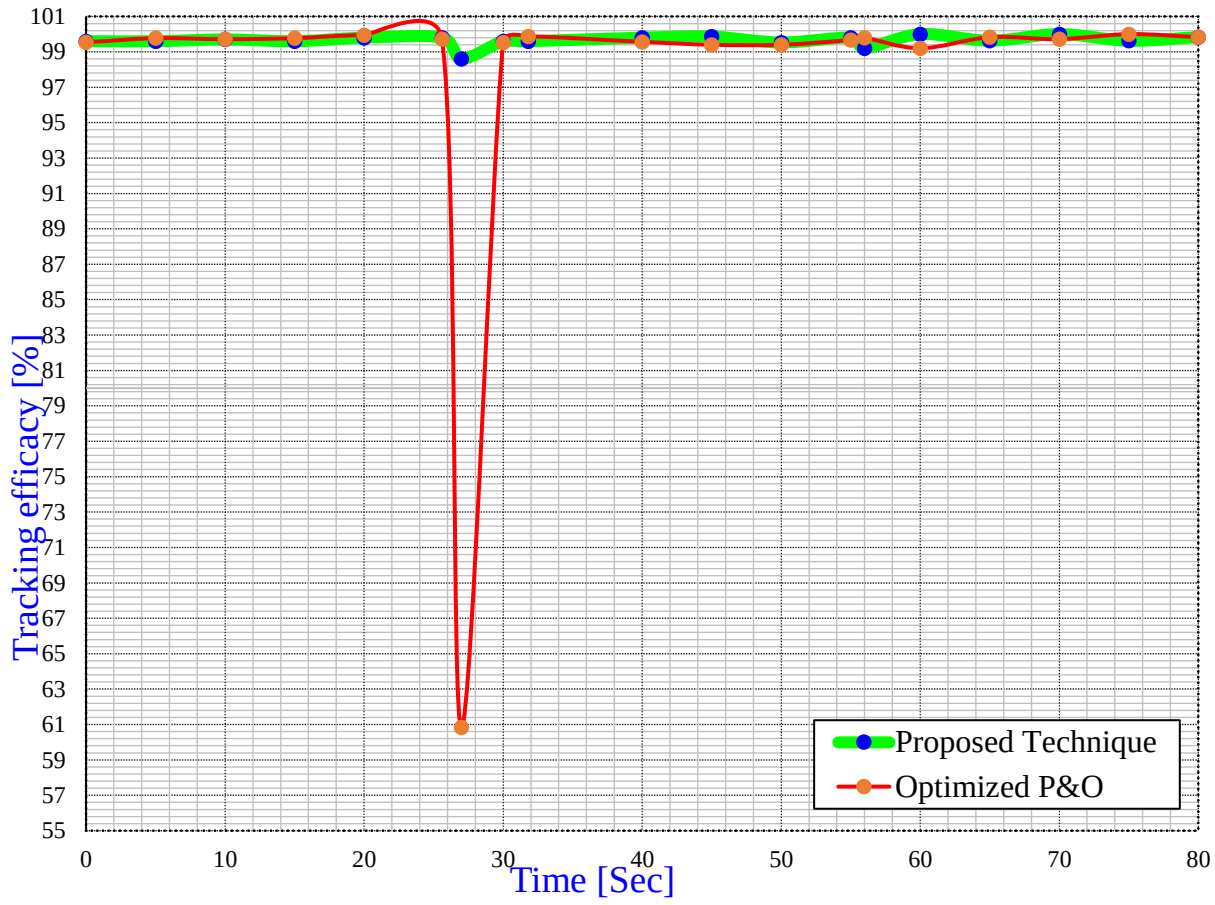

Figure 4.23: Tracking efficacy of the proposed technique versus optimized P&O over change in temperature

To further authenticate the enactment of the introduced approach, Figure 4.24 depicts the control effectiveness of the new harvesting strategy compared with the fuzzy logic control technique over a range of irradiance values. The method could not prevent a significant power drop; however, it immediately attempts to get recovered by capturing the available power and improving the tracking accuracy. The Figure describes the tracking efficacy and show that the

efficacy falls to almost 52.69% at the abrupt change of degradation and takes 6.2 seconds for tracking correction.

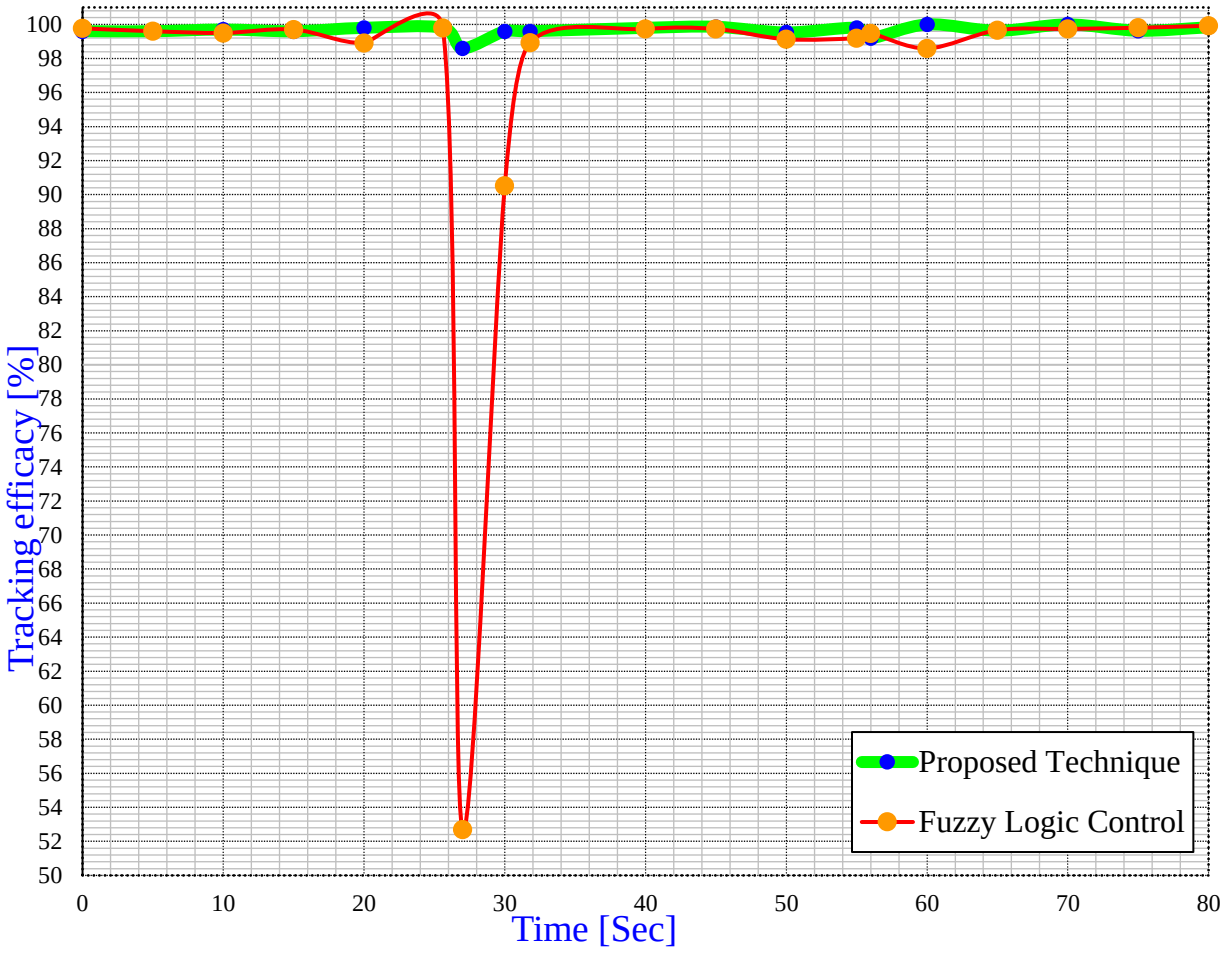

Figure 4.24: Tracking efficacy of new technique versus fuzzy logic control over change in temperature

The two selected methods show that tracking efficacy can be described as less efficient with less capability to prevent undesired fluctuations and improper efficacy failure. It may lead to a stability problem created by inaccurate tracking. This problem must be paid attention to, although the instability phenomenon doesn't appear in real time experiment of the new introduced technique.

The 3-D figures are another form of comparison that provides an extra verification and a

clear detailed description of strengths and weaknesses.

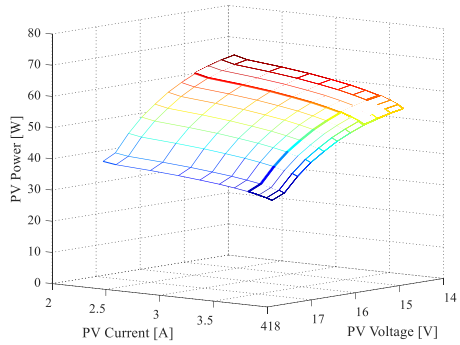

(a) 3D-Perturb and Observe

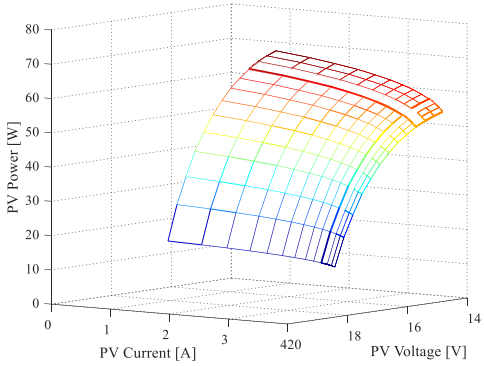

(b) 3D-Incremental Conductance

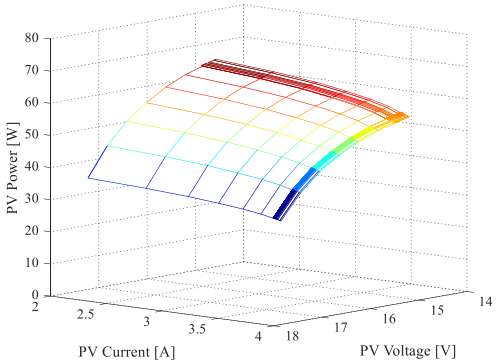

(c) 3D-Optimized Perturb and Observe

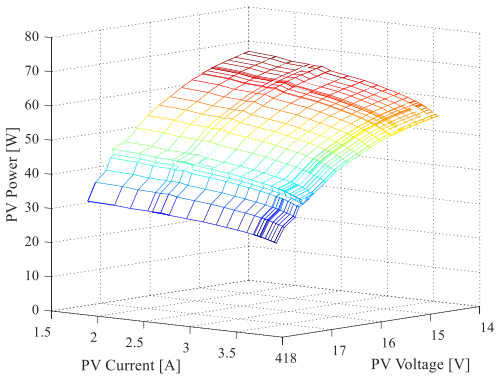

(d) 3D-Fuzzy Logic Control

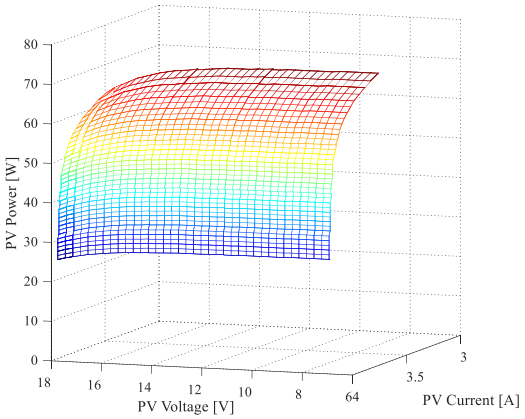

(e) 3D-Estimated Perturb-Perturb

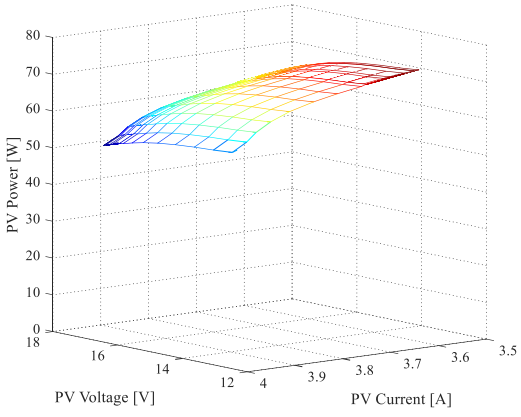

(f) 3D-results of proposed technique

Figure 4.25: PV voltage, current and harvested power of five common techniques and proposed method

According to Figure 4.25, the outcomes can present different aspects of the performance and provide their own dynamic configurations. The figures give an impression of how the proposed method reacts robustly without exhibiting a severe power drop compared to the other available power extracting techniques. The worst power drops were reached by the IncCond method. That power drop was 15 W, which is 27% of the anticipated power of 55 W upon ambient conditions in addition to the estimated perturb-perturb, which exhibits 22 W, a 60% power drop.

Table 4.2: Details of the experimental results

	PV Tracking Strategy	Ambient Temp. Condition @ 1000W/m^2	PV Voltage (V)	PV Current (A)	PV Captured Power (W)	Power Drop Point (W)	Tracking Time step up -down (sec)	Energy losses W s	Transient Efficacy (%)	Overall Tracking Efficacy (%)
1	Traditional P&O	25℃	17.6, ±0.5	3.61	63.536	38.6	3.2 - 2.0	18.986	70.18	98.72
		50℃	15, ±0.5	3.59	53.85					
2	IncCond	25℃	17.6, ±0.5	3.594	63.25	15.31	4.4 - 2.2	62.464	27.84	97.9
		50℃	15, ±0.5	3.591	53.865					
3	Optimized P&O	25℃	17.6	3.62	63.712	33.46	3.0 - 2.5	22.537	60.83	98.86
		50℃	15	3.61	54.15					
4	Estimated Perturb-Perturb	25℃	17.6, ±1	3.612	63.57	22.45	4.2 - 2.4	57.51	40.82	98.37
		50℃	15, ±1	3.597	53.955					
5	Fuzzy Logic Control	25℃	17.6	3.62	63.712	28.98	5.2 - 4.0	78.28	52.69	97.63
		50℃	15	3.61	54.15					
6	New Strategy	25℃	17.6	3.625	63.8	54.23	1.8 - 2.0	5.17	98.61	99.8
		50℃	15	3.61	54.15					

Table 4.2 presents more numerical details and it shows that the optimized P&O and fuzzy logic show very comparable behavior, but those methods could not prevent the power drop during a temperature step up.

4.2 Simulation Results of the Proposed PV Grid-Tied System

4.2.1 PV Grid-Tied System Under Partial Shading

Figure 4.26 demonstrates the global search and numerous simulations that are carried-out with the proposed new harvesting method to evaluate and analyze the performance of the method according to the three mentioned comparison criteria.

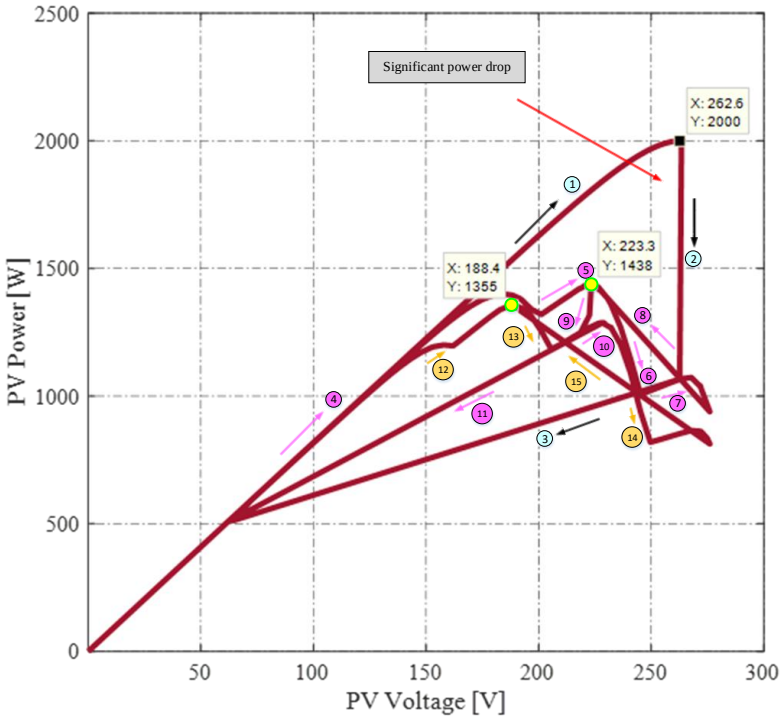

Figure 4.26: Successful global search in the case of two partial shading scenarios

Figure 4.26 illustrates the global search steps for when the PV system is under different patterns of partial shading. It shows that the PV system climbs up at step 1 and generates the maximum power 2000 W during normal operations. In step 2, a significant captured power drop

occurs; therefore, the global strategy starts step 3 and begins scanning the P-V curve globally. In step 4, the PV system climbs up and searches for any available peaks within the P-V curve until it reaches step 7, which is the end of the searching zone. Then at step 8, the PV global search strategy-based power decides to jump to the new global power peak. If no significant power drop occurs or if an interruption was scheduled, the PV system continues operating using the new tracking method. The figure shows a non-significant power drop at step 9. As a result, the operating point was tracked to a local peak at step 10, waiting for a timer interruption to begin a new global search at step 11.

The next figures explain the performance during different environmental conditions and how the partial shading conditions can be efficiently alleviated.

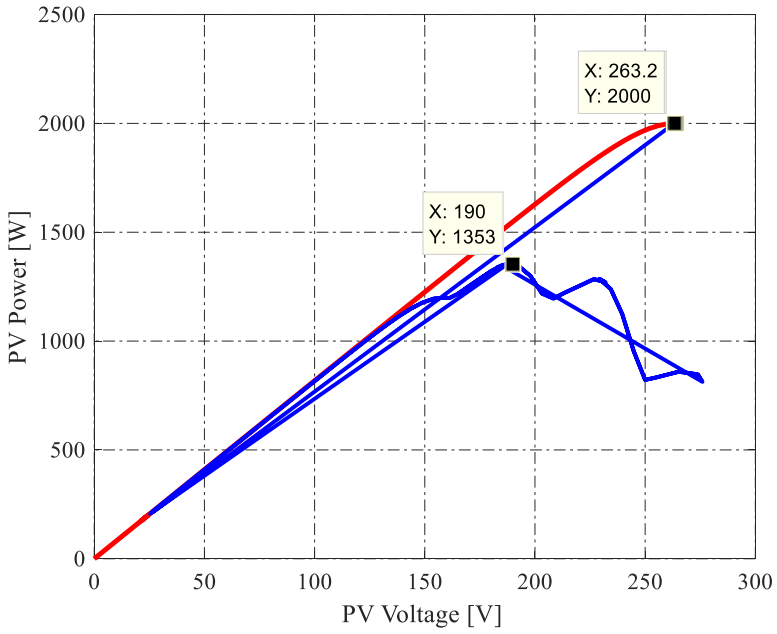

Figure 4.27: P-V characteristics of the proposed techniques under partial shading conditions

In Figure 4.27, the PV captured power drops noticeably due to partial shading. The new global search successfully mitigates the consequences; therefore, the new maximum power peak is correctly located at 1353 W while production was at its maximum 2000 W. It decreased by 67.6%.

In addition, the global search strategy checked four power peaks, which are 1200 W, 1353 W, 1250 W, and 875W before effectively deciding to choose 1353 W.

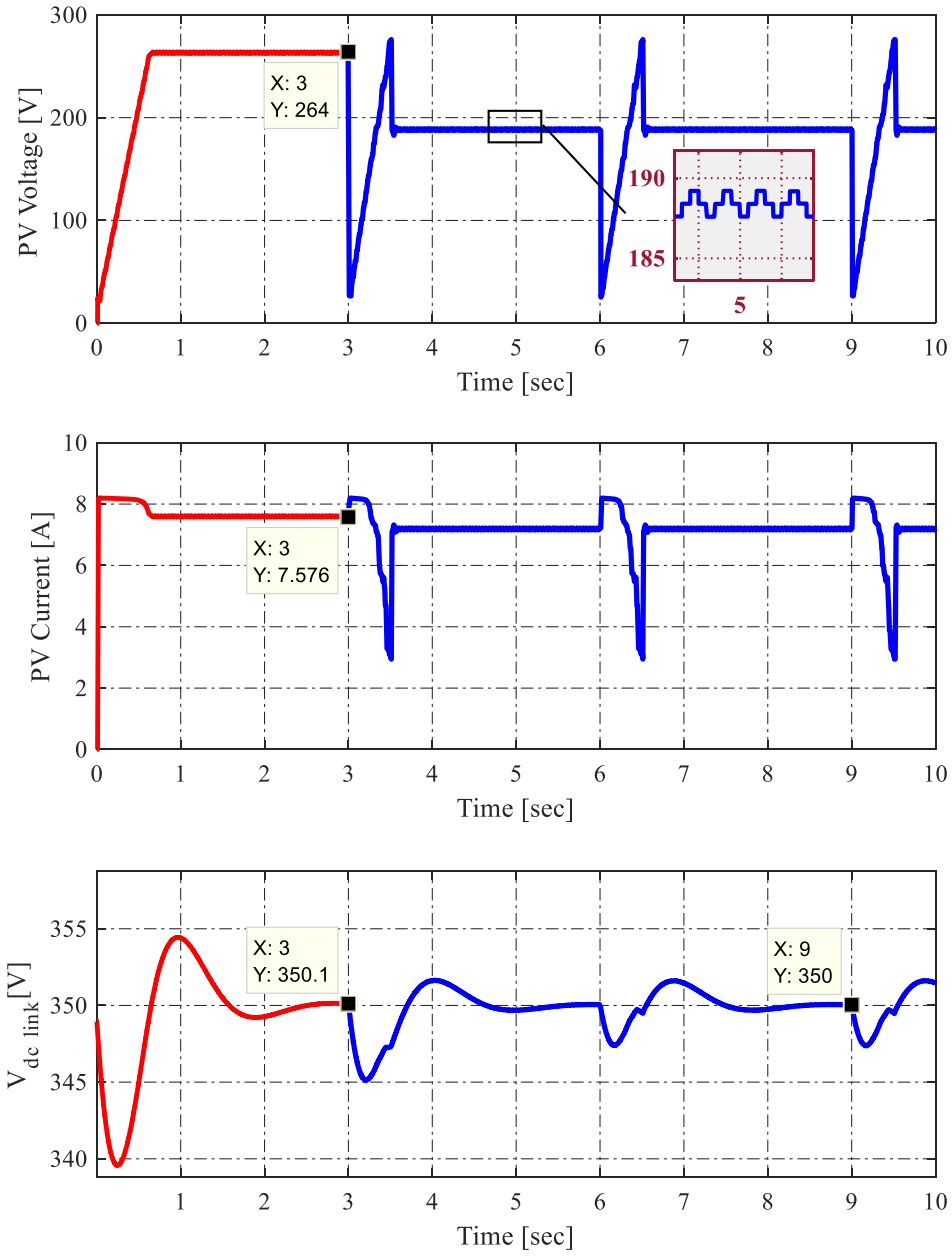

Figure 4.28: P-V voltage, current and Vdc-link of the proposed techniques under partial shading

The new strategy-based power is built to verify any number of possible peaks and can efficiently check as many power peaks as are available. According to this figure, the PV input

voltage shifts from 263 V to 190 V based on the new global power peak. It is obvious that the new peak is no longer at V_{MPP} = 263 V based on the module's specifications, and the attached figure also confirms that the global search keeps updating the power peak to interrupt the counter to validate the power peak, which strengthens the PV system power delivery. It can be seen that the input current decreases from 7.57 A to 7.12 A

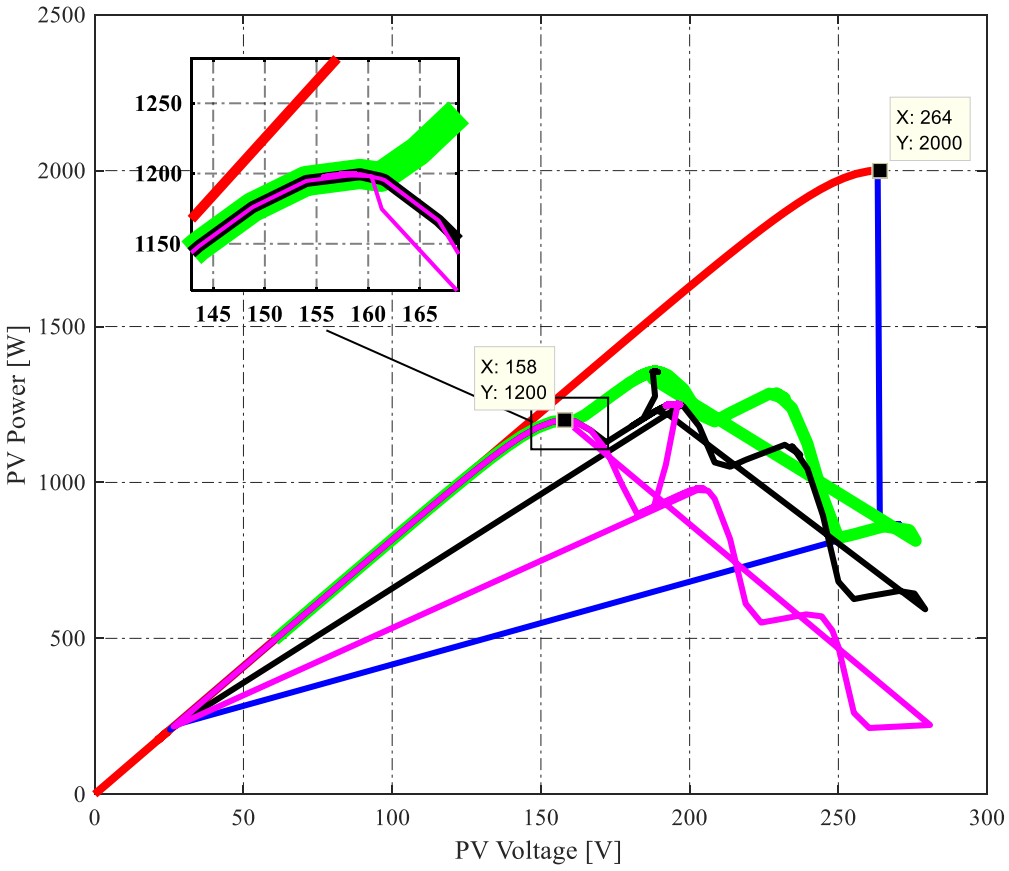

Figure 4.29: P-V characteristics of the proposed techniques under numerous partial shading conditions

Figure 4.29 reveals the worst scenarios of partial shading conditions when the operating point starts alternating randomly due to natural changes in shading. The approach needs to verify the search area limitation in the search zone. The figure shows that the searching strategy is set to start from the right side of P-V curve with a starting power point of 200 W and stop once it reaches

the exact number of pre-defined zones. The counter B increases incrementally by 1 and frequently matches the number of zones.

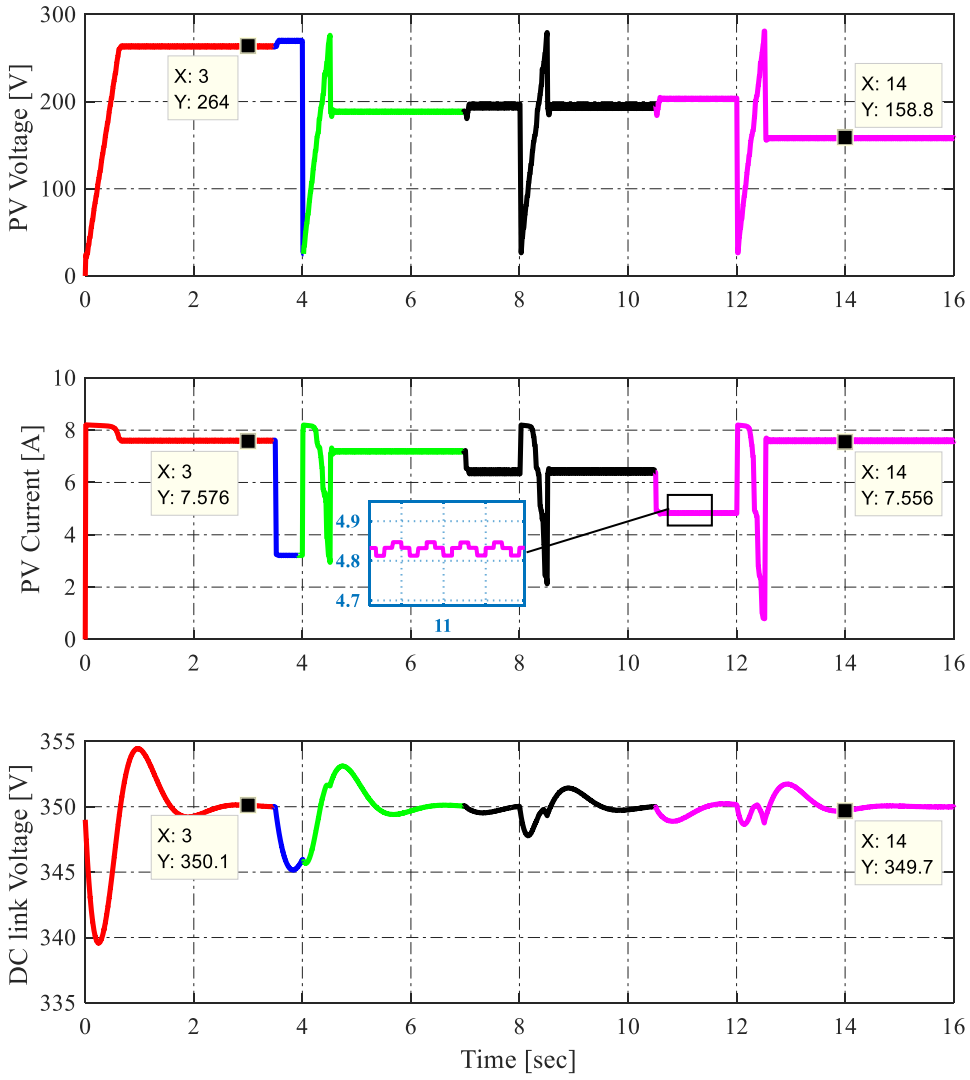

Figure 4.30: P-V voltage, current and Vdc-link of the proposed techniques under partial shading

The new strategy always starts at 200 W but stops at different levels of power based on the scenario available. The power peak is located effectively at each scenario. In first scenario, the maximum peak was 1300 W and then 1350 W, then 1250 W. Figure 4.29 also shows the zoomed view for a time interval of the last scenario in locating the global power peak and how the algorithm

traces while shading occurs. Figure 4.30 describes the changes and provides more details in terms of PV input voltage, current, and DC link voltage. The input voltage starts at 264 V, which is the V_{MPP}, and ends at 158.8 V. PV current also varies; however, it starts at 7.576 A and returns to almost the same value: 7.556 A. By multiplying the last received values of voltage and current, the result is 1200 W which is the last power peak as pointed out in Figure 4.29 on the P-V curve.

4.2.2 Current Sensorless of PV-Side

This section provides the waveforms result of the new current sensorless model.

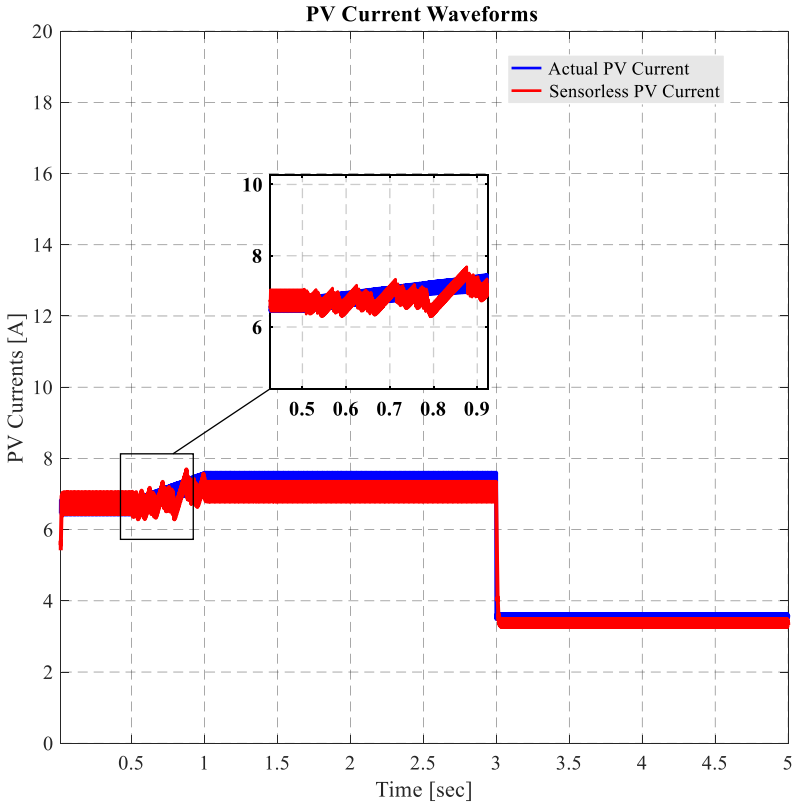

Figure 4.31: Actual PV current sensor and PV current sensorless when irradiance step changes

In Figure 4.31, the current starts at 6.8 A when the irradiance level is 800 W/m^2. Then the irradiance increases gradually to 1000 W/m^2 and as a result, the current raises up to 7.6 A. Once the irradiance drops suddenly to 300 W/m^2, it causes the current to decrease rapidly to 3.8 A.

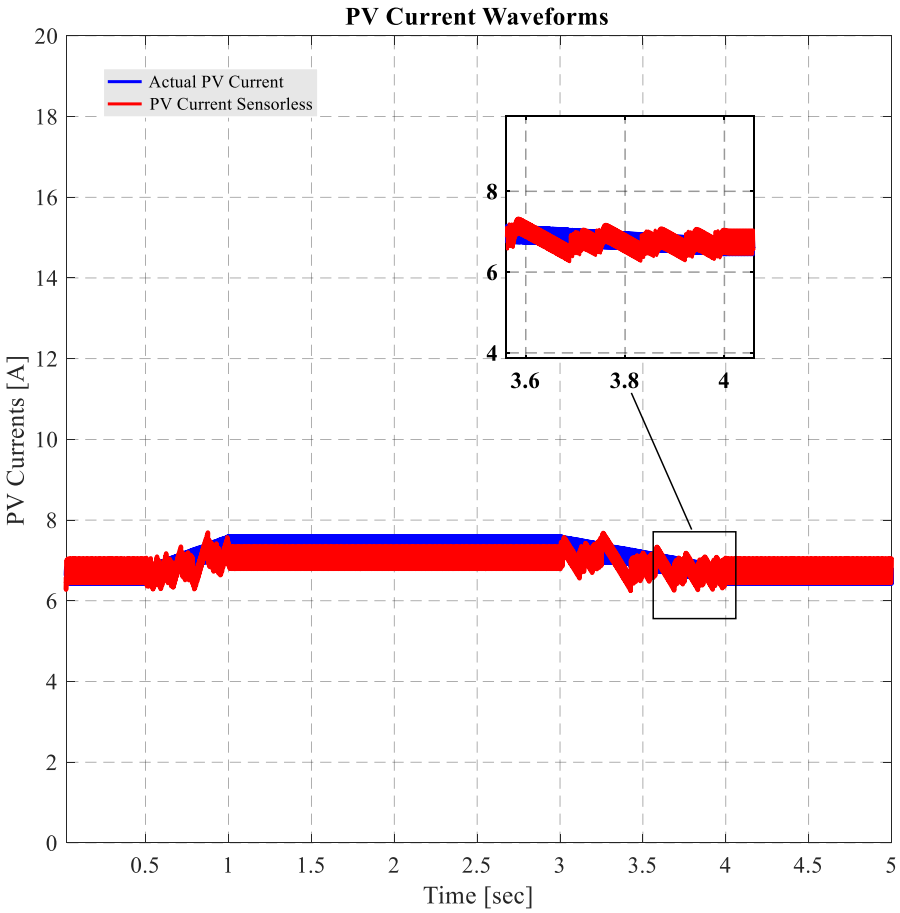

Figure 4.32: PV current waveforms when irradiance gradually changes from 900 W/m^2 to 1000 W/m^2

In Figure 4.32, the current starts at 6.8 A while the irradiance is fixed at 800 W/m^2 and similarly the illumination is increased slowly, and the current is also increased since the relationship is upward. However, when the illumination decreases slowly the current responds but, in both cases, exhibits undesired fluctuations. It is referred to as a derived model and constraints are set based on steady state conditions. The new model is worth noting that such performances do not significantly affect the operating conditions and the design is still able to develop and strengthen; however, it attempts to cut off equipment and become cost-effective with negligible oscillations in transient situations. As long as it responds within an acceptable range of oscillations, it is a sufficient model. Overall, using the current sensorless observer model for the PV current

demonstrates a similar performance, principally if it is compared to an actual current sensor. Therefore, the new introduced model eliminates the current sensor and the performance remains similar except it exhibits less negligible amplitude.

4.2.3 AC Waveforms of the PV Grid-Tied System

This section contains the AC waveforms of the PV grid-tied solar system and national grid side. Figure 4.33 shows the difference between the sinewave of the utility grid and the square waveform produced by the PV system. Sinewave has amplitude of 170 V while the inverter square wave has amplitude of 202 V.

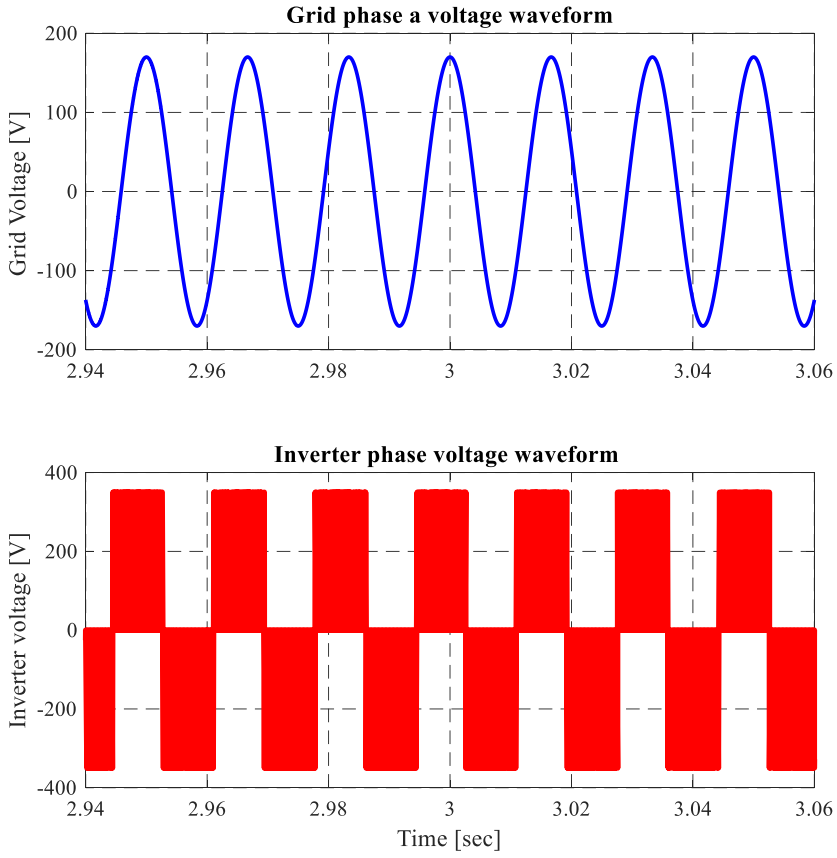

Figure 4.33: Grid voltage and inverter phase A voltage waveforms

In Figure 4.33 the phase voltage of the grid has a standard amplitude equal to 170 V and the inverter phase voltage is equal to 200 V.

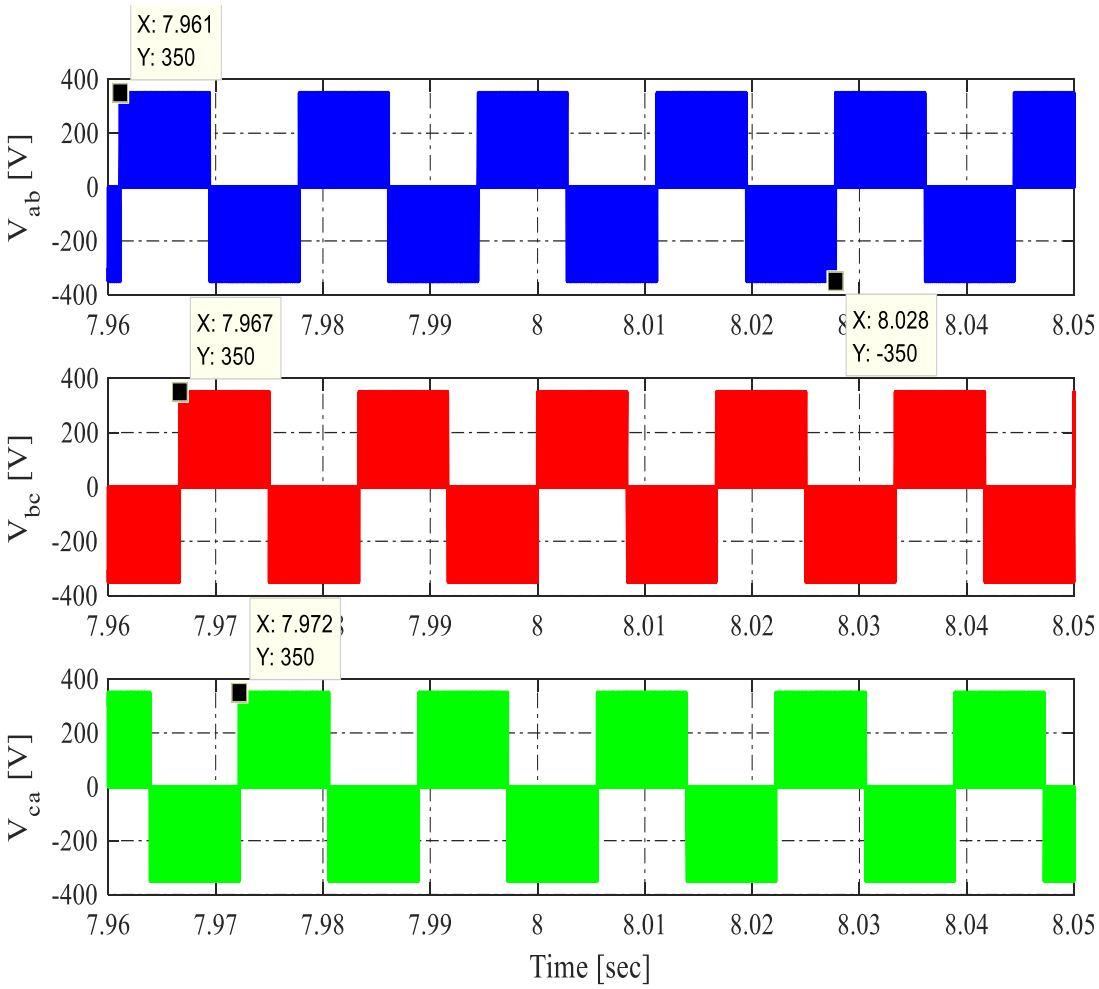

Figure 4.34: The output of the inverter three phase line to line voltage

Figure 4.34 displays the three line to line voltages, which are the output of a traditional inverter. The voltage amplitude of line to line voltage is 350 V which is higher than the voltage amplitude of utility grid 294 V. Otherwise no current would be flowed into the grid. It shows stable waveforms that are appropriate and necessary to maintain under synchronization conditions including a 120^{o} phase shift. As demonstrated, the V_{ab} waveform starts at 7.96 seconds and 120 degrees in time equal to 0.00556 seconds so the phase shift in a form of time for the next waveform

is 0.01112 seconds. This is equivalent to 240^{o} ; and THD is equal to 46.27% and quite high since there are square waveforms.

4.2.4 Simulation Results of Power Injection Model of PV Grid-Tied System

Figure 4.35 presents the introduced PV grid-tied solar system when power factor enforces

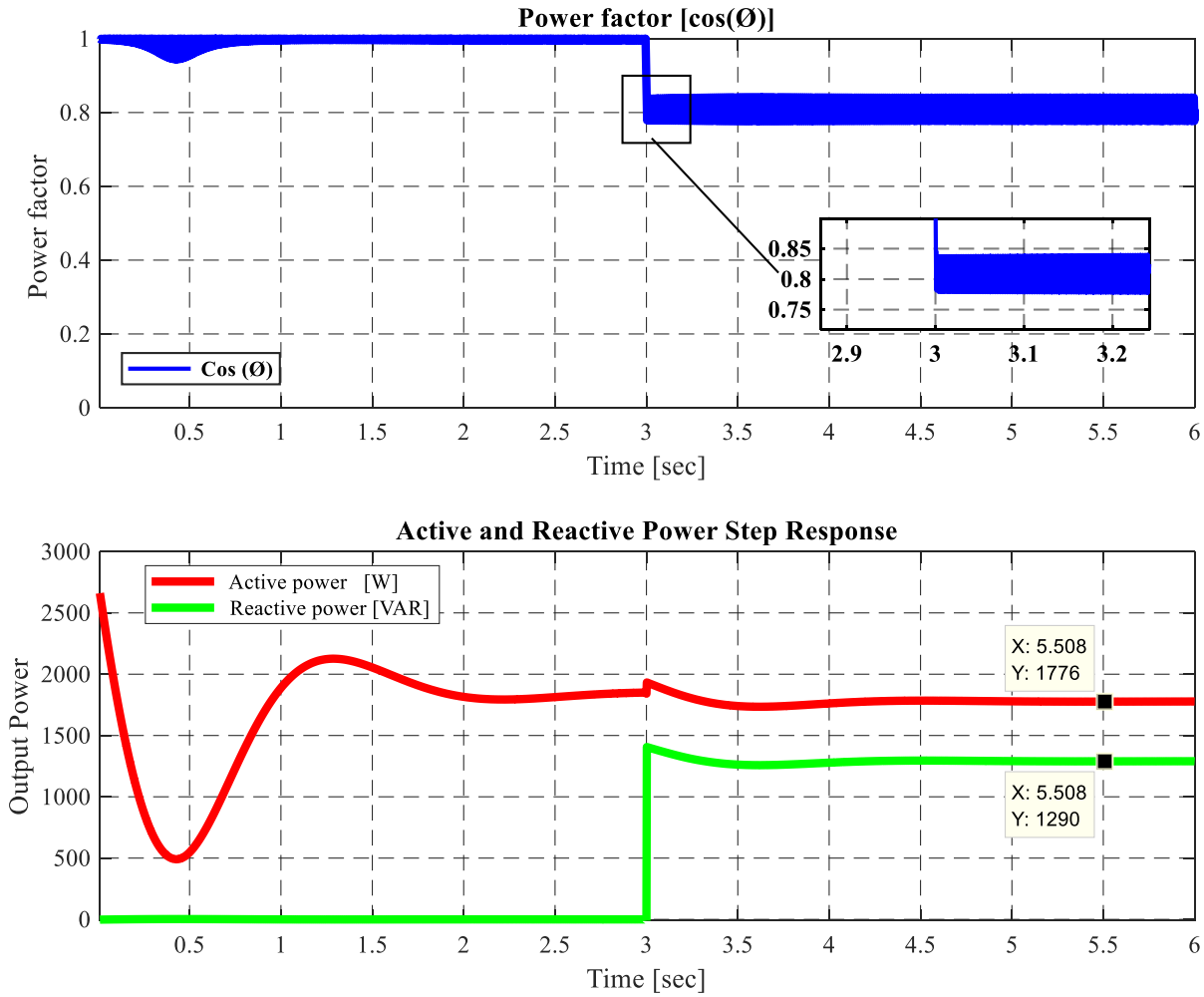

Figure 4.35: Output power (injected active and reactive) when power factor step changes from 1 to 0.8

step change from unity power $\cos\phi = 1.0$ to $\cos\phi = 0.8$. It shows the resulting power factor after setting the step change, which occurs at three seconds. As a result, the output reactive power injects into the AC grid changes from Q=0 VAR to Q=1290 VAR while no change occurs in the output

active power delivered into the grid. It continues delivering P=1776 W. The delivered active power waveform experience is a transient state, and it takes about 2 seconds to settle.

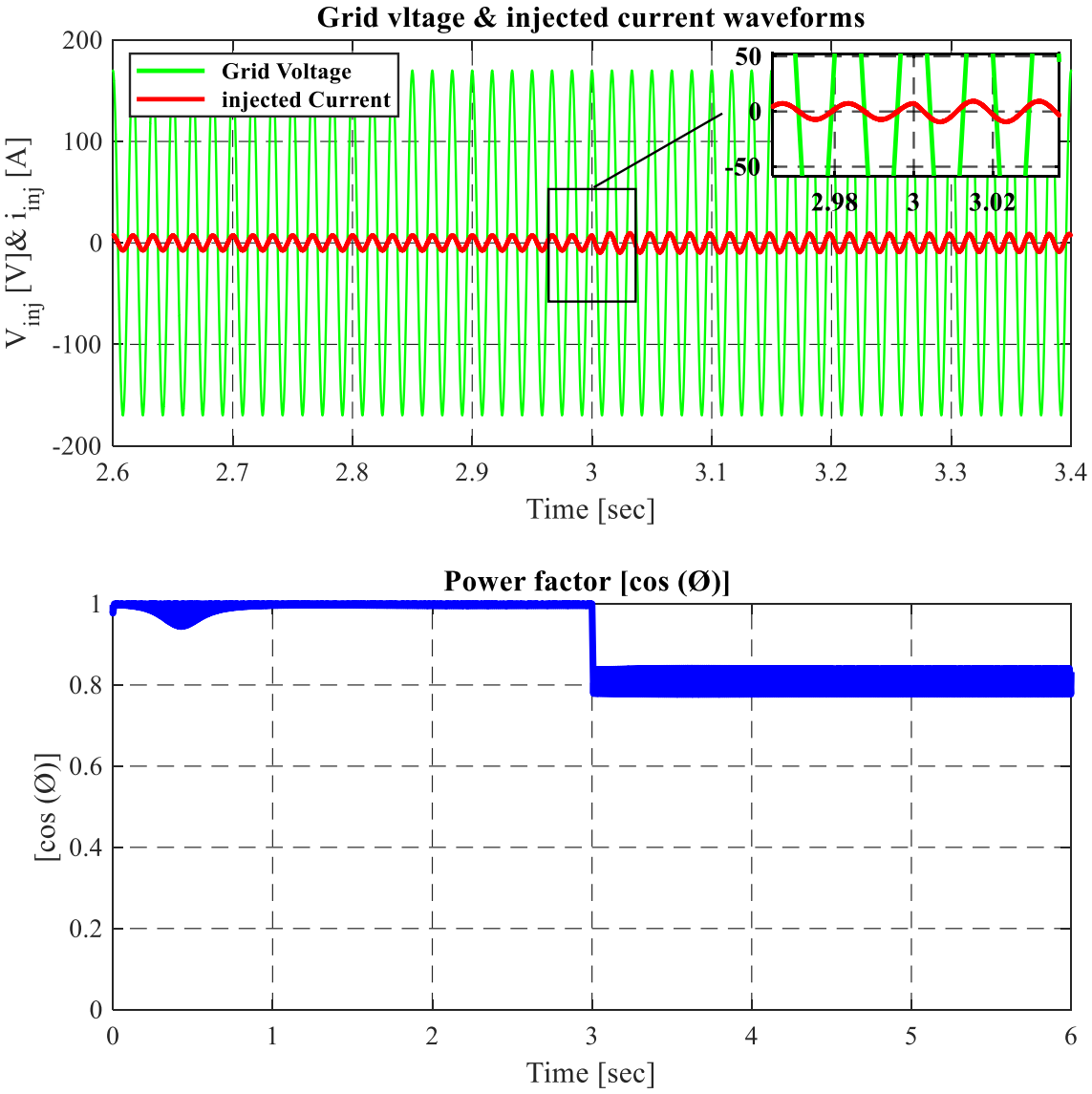

Figure 4.36: Grid voltage and injected current when power factor step changes from 1 to 0.8

The dynamic response upon a power factor step change is illustrated in Figure 4.36. The power factor changes from $\cos\phi=1.0$ to $\cos\phi=0.8$. The figure includes a zoomed-in view for the time interval at step change when $t=3.0$ seconds. The focused zoomed view shows the transition

at zero-crossing at the time axis (x-axis) between the grid voltage and injected current waveforms. It clearly depicts how the injected current responds to the step change and shifts by a new phase shift angle of 36.8^{o}.

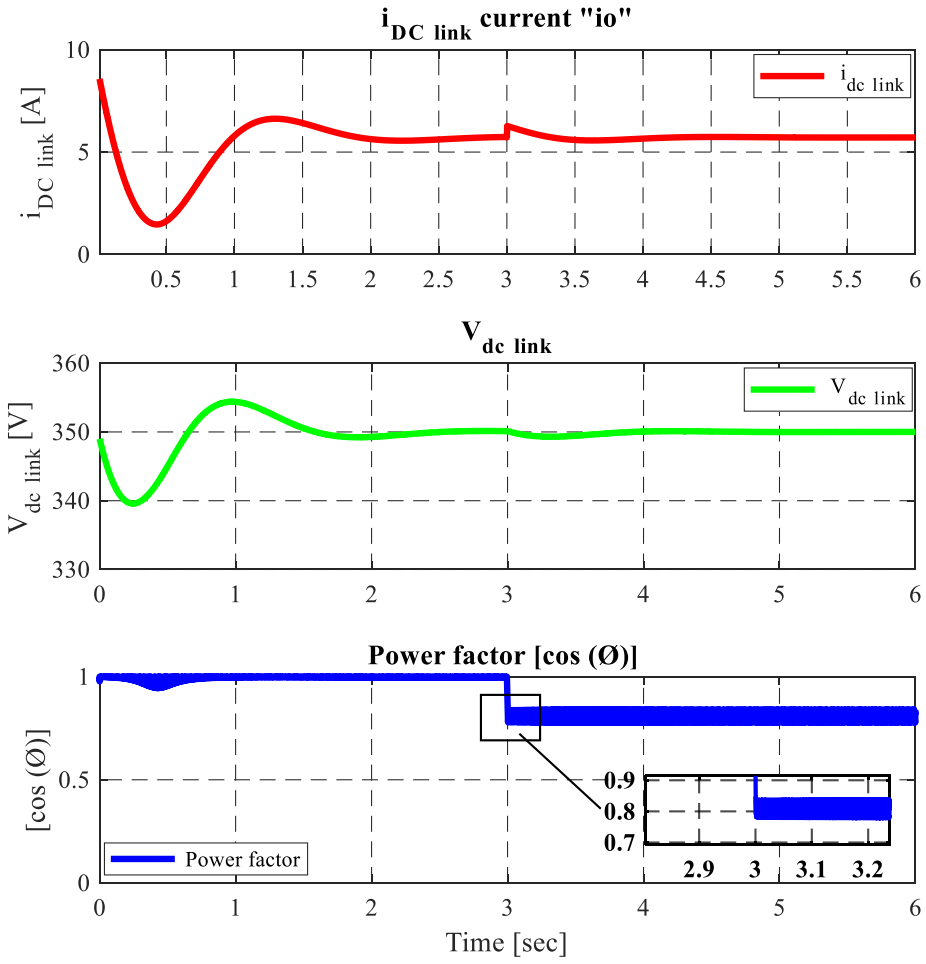

Figure 4.37: Converter output current and Vdc link waveform when the power factor step changes from 1 to 0.8

Figure 4.37 offers more details about the dynamic response as the DC input current passes through the classical DC/AC inverter. The current shows no change while the power factor changes from $\cos\phi=1.0$ to $\cos\phi=0.8$. Likewise, the DC link voltage also stays robust against the step change and converges at the reference value of 350 V. The transient state takes only 2 seconds

before the PV grid-connected system becomes stable. It is obligatory and essential for the PV grid-tied systems to control the DC link voltage effectively and prevent any fluctuation. However, these systems can encounter such scenarios due to the aforementioned ambient changes or as a result of desired changes such as adjusting the power factor, but the system should show solidness and steadiness to overcome such challenges and be able to address them successfully based on control requirements.

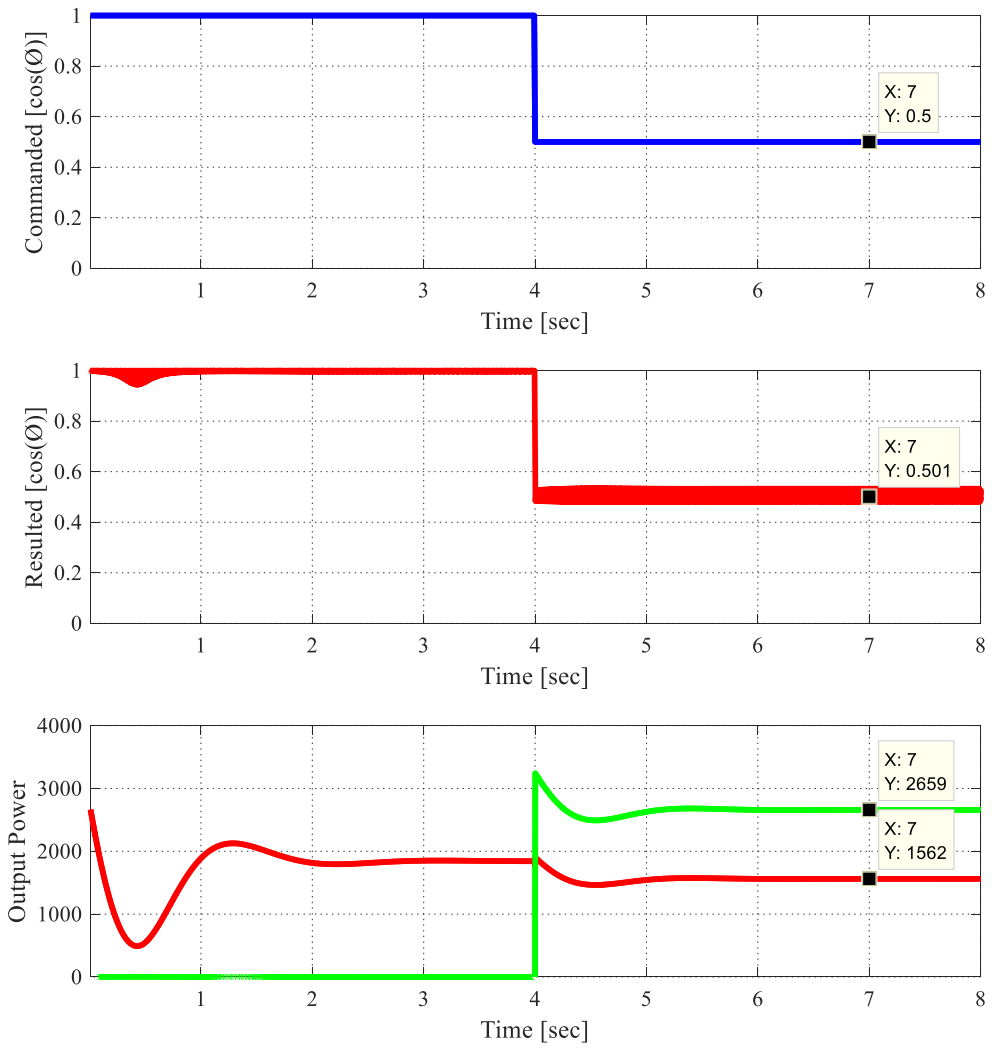

Figure 4.38: Output power factor and injected active and reactive power when power factor step changes from 1.0 to 0.5

Similarly, Figure 4.38 shows a step change of the power factor reference. It is a step change from $\cos\phi=1.0$ after 4 seconds to $\cos\phi=0.5$. The resulting power factor typically has ripples as a result of switching frequency and the transient state at 0.5 seconds. The injected reactive power starts at Q=0 VAR and then steps-up to Q=2659 VAR. The generated active power delivers P=1914 W but once the power factor changes to $\cos\phi=0.5$, the active amount decreases to P=1562 W, which is a decrease of 18.4%.

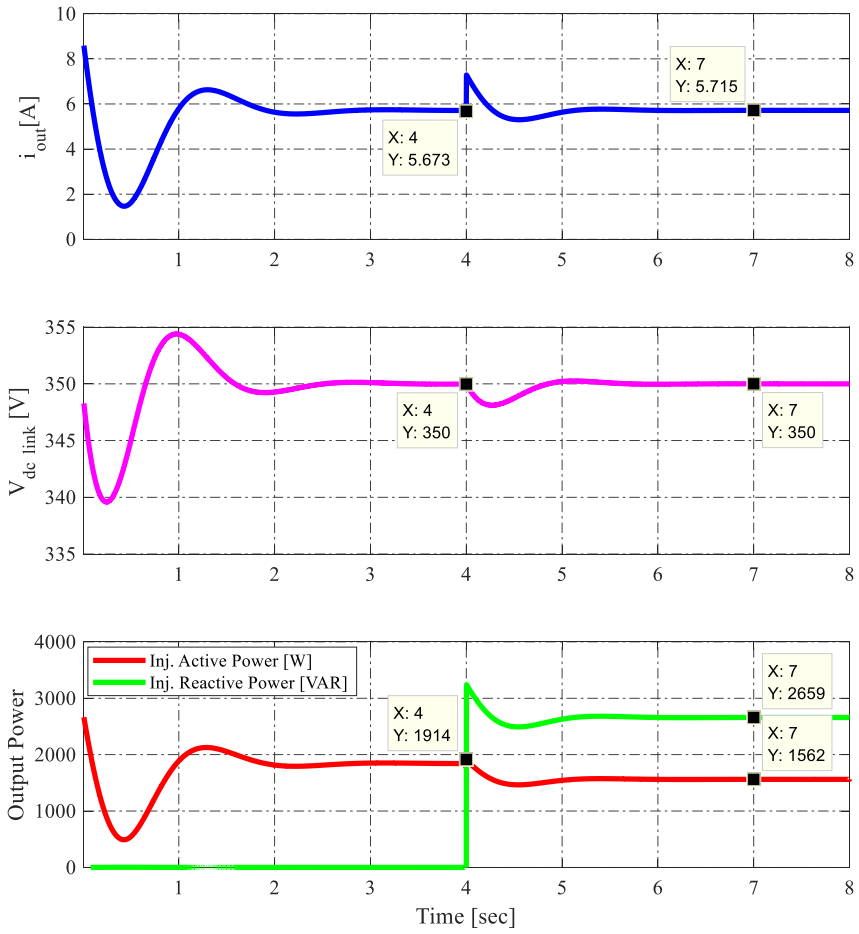

Figure 4.39: Converter output current, DC link voltage and the injected active and reactive power

Likewise, Figure 4.39 displays the DC input current as it passes through the traditional DC/AC inverter. The current varies slightly up from 5.673 A at $\cos\phi=1.0$ when $t<4.0$ seconds

to 5.715 A at power factor step change when $t=4.0$ seconds. The DC link voltage transient state at the beginning takes 2.0 seconds while it tries to settle at the DC link voltage reference of 350 V. The DC link voltage remains constant and converges at the reference despite that it exhibits insignificant transient when the power factor step changes from $\cos\phi=1.0$ to $\cos\phi=0.5$.

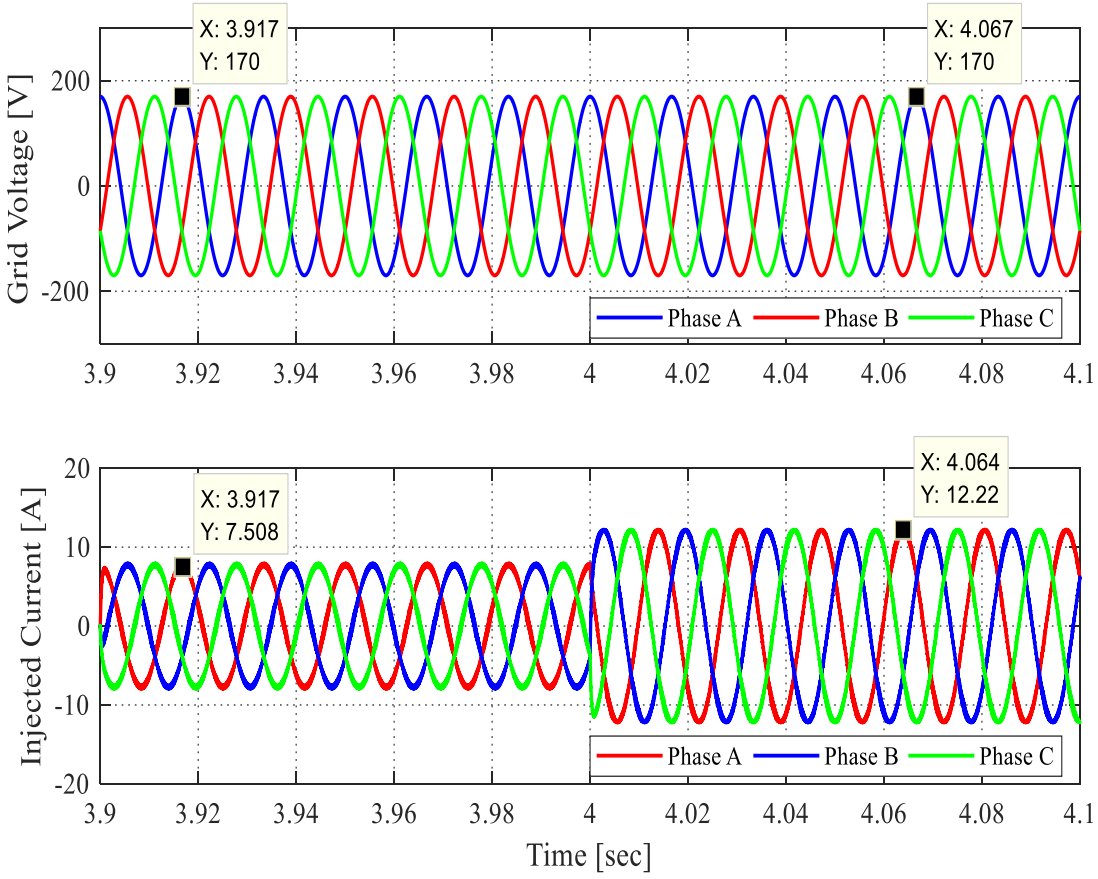

Figure 4.40: The grid phase voltages and injected three phase current

In Figure 4.40, the grid voltage always has a constant phase voltage amplitude of 170 V. The injected current shows a minor transient state at step change once the power switches from 1.0 to 0.5. The DC link voltage still imposes a fixed voltage amplitude current, and safety requirements often dictate a need for isolation between PV arrays. Moreover, Figure 4.41 illustrates only the voltage waveform of phase A and waveform current of phase A and clearly demonstrates how the

new step change in power factor can shift the injected current of phase A according to a new phase shift angle.

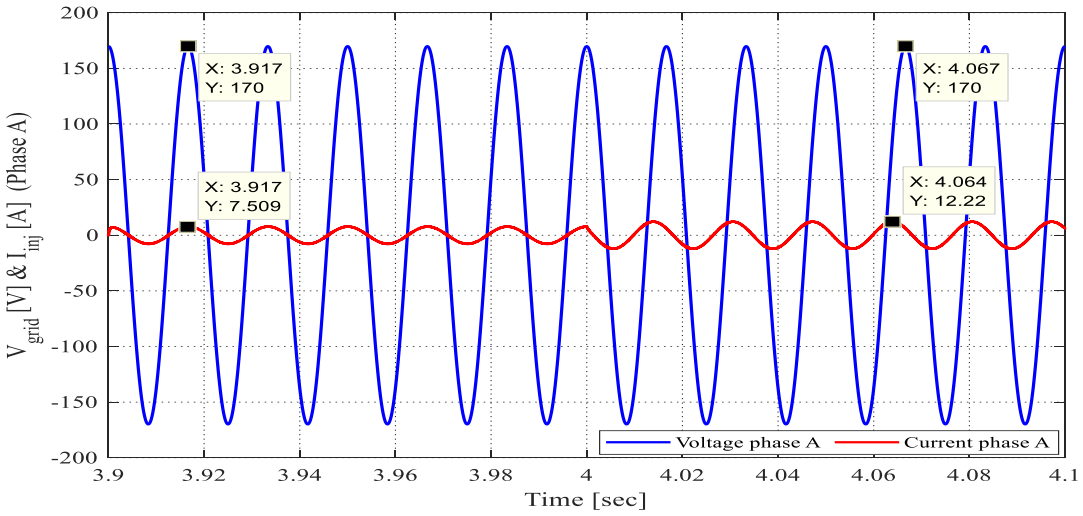

Figure 4.41: The grid voltage and injected of phase A

Figure 4.42 shows step-up behavior when undesirable change occurs in DC link voltage. It presents that the introduced control can control the DC link voltage and the possibility to step it up or down. The DC link voltage is set to jump from 350 V to 360 V. The system's outstanding control can perfectly converge at the targeted voltage reference precisely in a short time. The figure also illustrates an injected active power waveform while the injected reactive power is equal to zero since the power factor is set to 1.0. It can be clearly seen that the load is capacitive.

The upcoming Figures 4.42 and 4.43 are very important and share a significant result. Both present how it would possible to vary the DC link voltage effectively. They confirm the ability to step up or step down without needing to play with the DC/DC converter duty cycle. Consequently, the next section will introduce the obtained result when the PV grid-connected system experiences a loss of cascaded H-bridge converter cells and how the DC link can be boosted up by setting the desired DC link voltage reference.

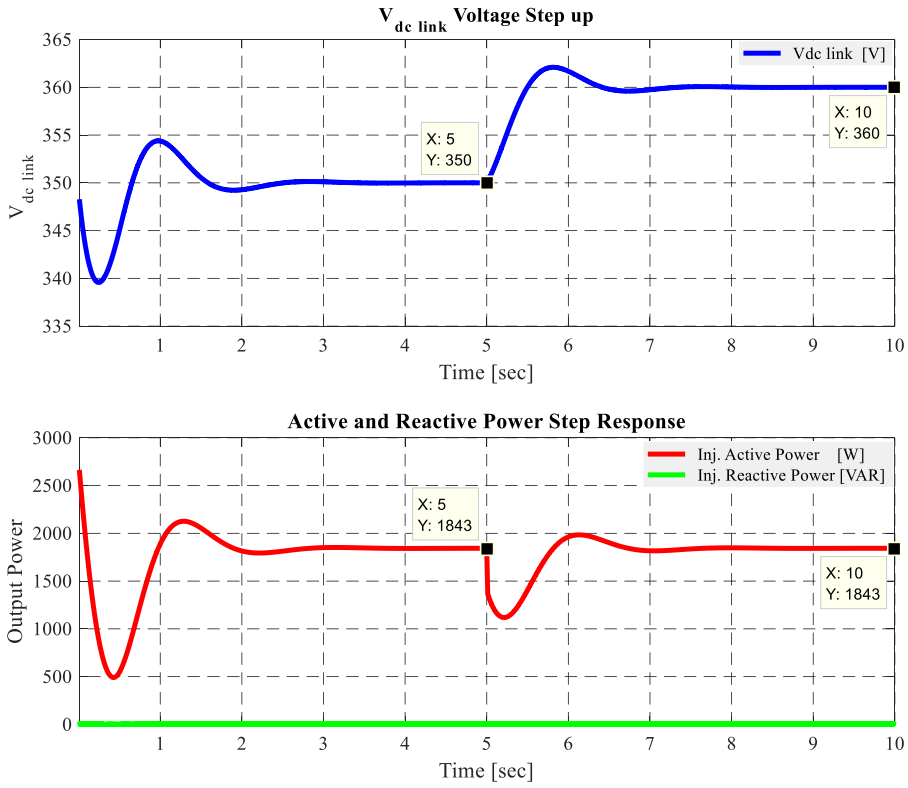

Figure 4.42: Active power waveform when Vdc link voltage step change from 350 V to 360 V

Next, Figure 4.43 elaborates how designed control of the PV grid-connected system can direct the DC link voltage to the reference value. The DC reference voltage was 350 V before the DC link voltage step-up occurs at $t = 5.0$ seconds. The transient state takes 2 seconds at the start and only takes 1.50 seconds after the DC link voltage step change. The delivered active power remains constant as illustrated.

In Figure 4.43, the reference voltage steps down from 350 V to 340 V. Likewise, the control shows a very efficient dynamic response to the DC link voltage step change as it takes only 2 seconds in the transient state from the start point while taking just 1.0 second to settle at a new reference voltage. Since the power factor $\cos\phi=1.0$ the injected reactive power is equal to 0 where Q=0 VAR and the active power is at its maximum power delivery P=1843 W.

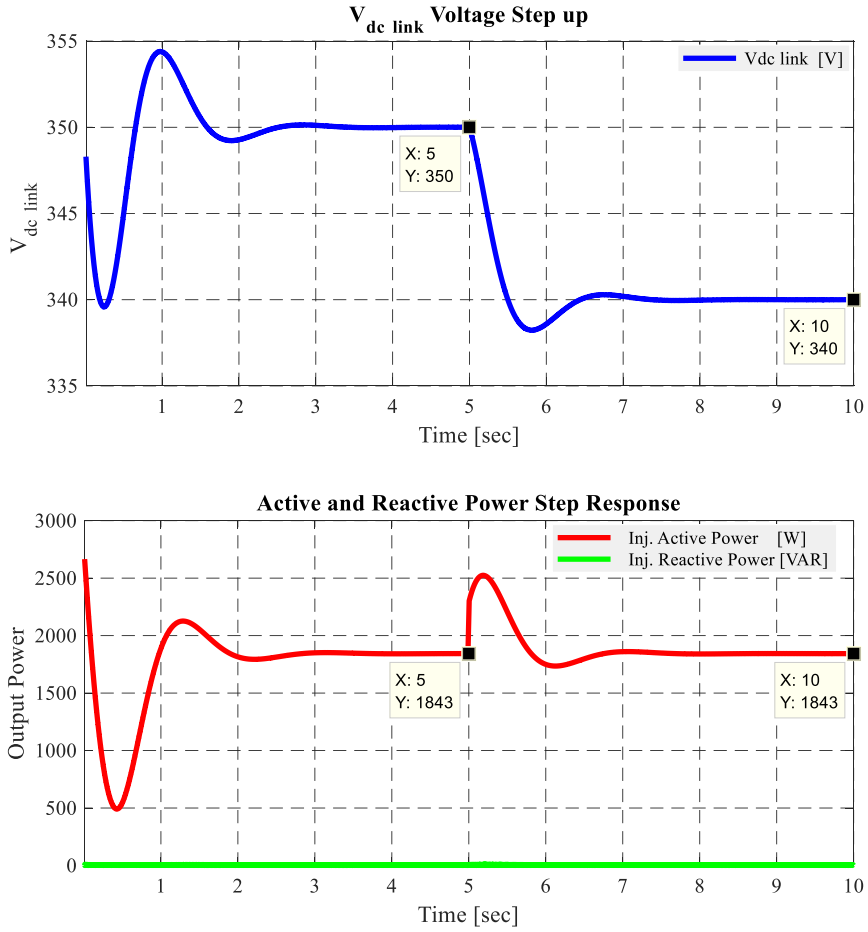

Figure 4.43: Active power waveform when Vdc link voltage step change from 350 V to 340 V

During normal operation, the PV grid-connected system generates line to line voltage amplitude equal to 350 V. The voltage is 1.186 higher than the line to line grid voltage. This will allow the proposed system to inject the designated power into a utility grid.

4.2.5 Simulation Results of a PV Grid-Tied at Fully Shaded Scenario

During the severe partial shading, the new topology applies fundamental phase shift compensation first to quickly impose balanced line to line voltages by using a set of equations based on the number of fully shaded cells in each phase. Figure 4.44 displays the balanced transition of a PV grid-tied system. In the transient state, if the PV system fails to raise up the DC

link voltage, it may go off grid to supply AC loads locally since line to line voltage is less than line to line grid voltage or can be isolated to give time for the voltage to rise once the severe shading get cleared. The figure also shows the system takes around 0.53 seconds to rebalance. The DC link voltage is boosted by the DC/DC converter, and the PI controller is set to provide desired gains to increase the AC voltage through the modulation process and generate balanced line to line voltage.

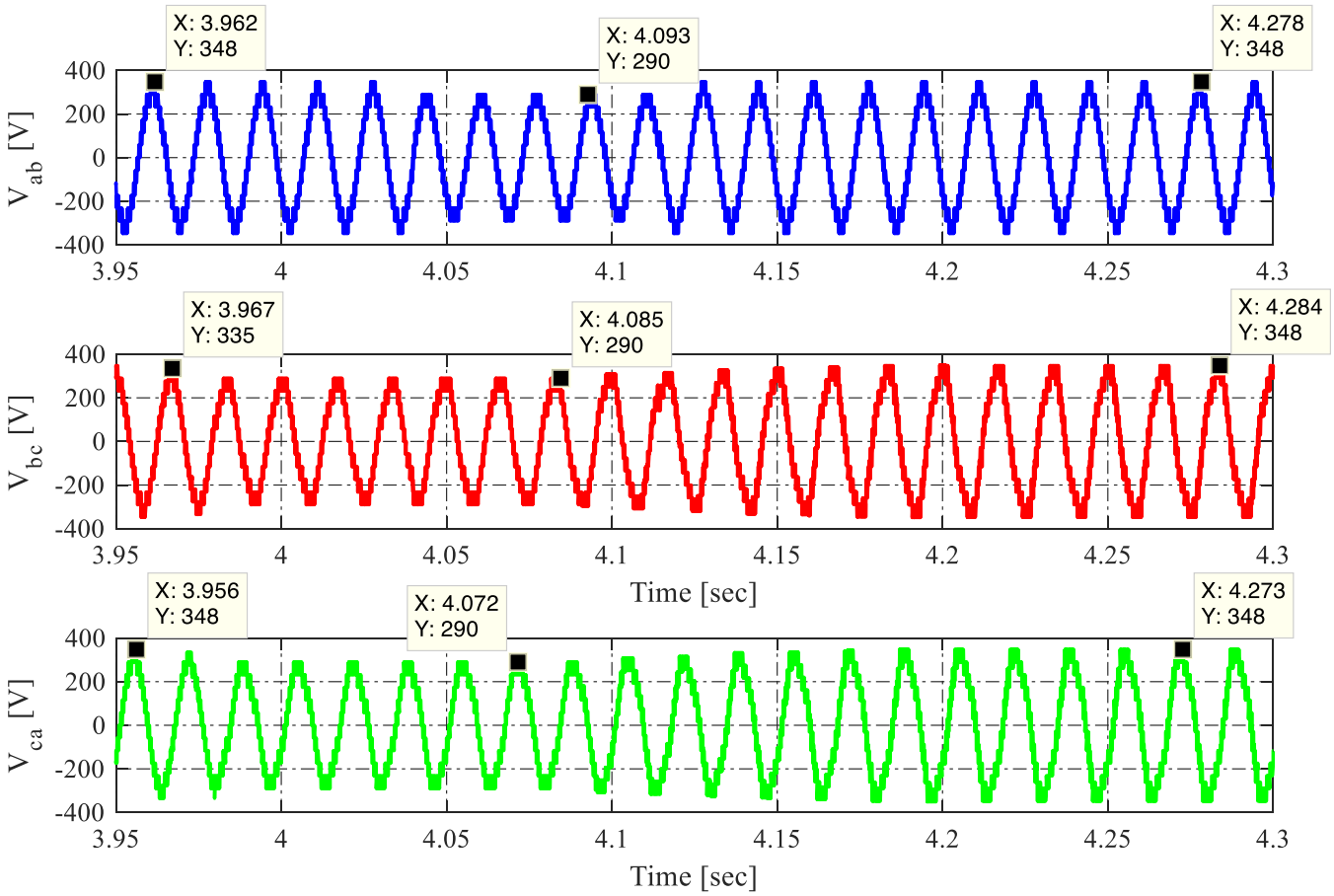

Figure 4.44: CHB output line to line voltage (pre-shading, fully shaded, post shading)

As a result, the four equations are valid to rebalance the line to line voltages as long as the number of shaded cells has not exceeded a certain number. The rebalancing can restore only the line to line voltage. The new line to line voltages with equal amplitudes of 290V are presented;

however, the new balanced amplitude is relatively less than the pre-shading amplitude's voltage (348V). Thus, controlling the DC link voltage is an important feature that can compel the DC link voltage to increase the same as the pre-shading state based on the DC link reference voltage. The unshaded cells with DC/DC converters boost the DC link voltage to pre-shading within the duty cycle limitation. The cascaded H-bridge converter in phase C only depends on the unshaded cells. An important advantage of unifying the DC link voltage is to raise the unshaded cells' voltage to ensure power transfers into the grid and maintain balanced three-line to line voltages at the time of the fully shaded CHB's cell. Thus, unshaded cascaded cells in the same phase can ensure balanced line to line three-phase voltage during module mismatch, which allows the converter to keep the power flow into the grid with balanced line-to-line voltages.

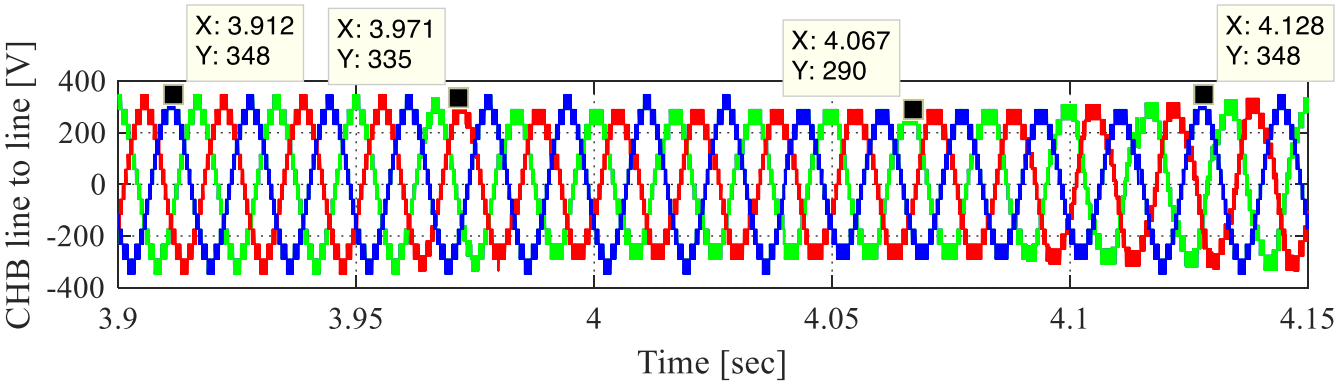

Figure 4.45: Line to line voltages waveforms rebalancing

In chapter 3, Figure 3.34 illustrates a CHB converter's diagram which composed of multiple series connected to multicell per phase when they start to experience full shading. The new control observes the DC link voltage per phase and imposes the balancing under such conditions. It isolates undesired voltage fluctuation to enforce fixed voltage.

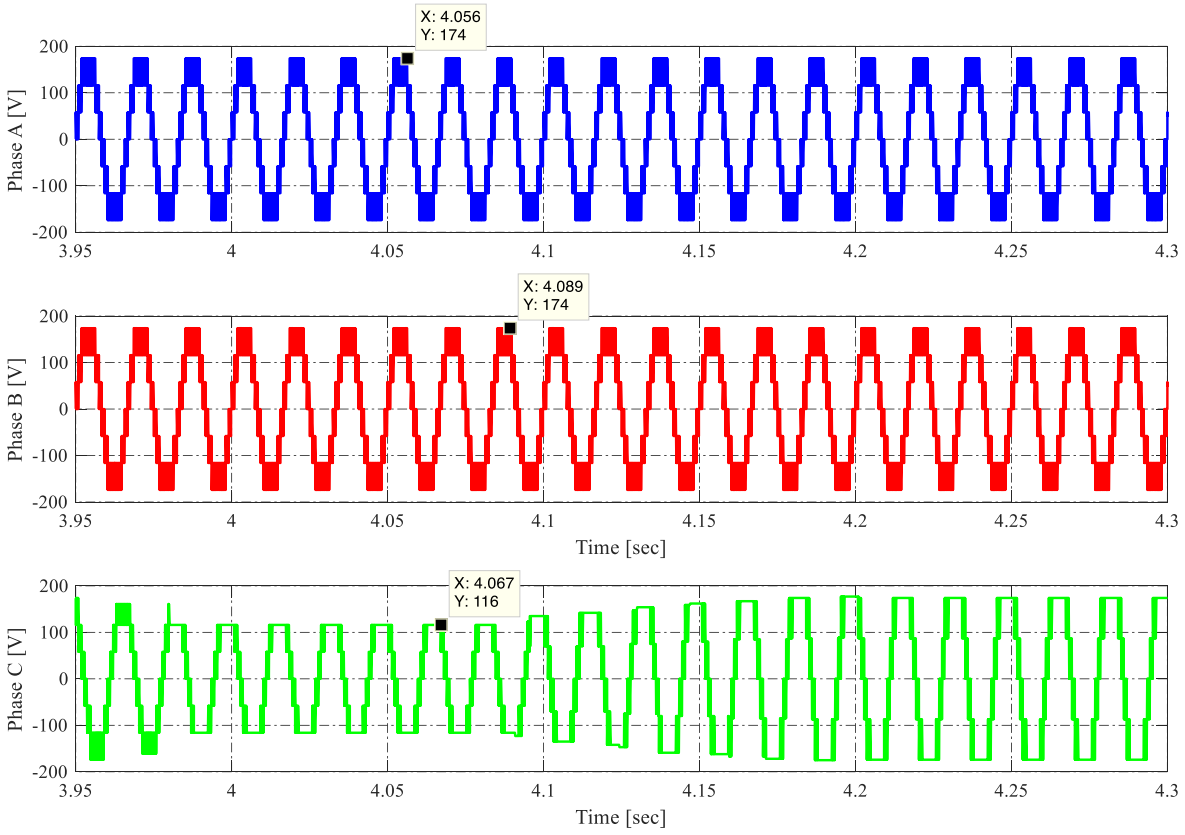

Figure 4.46: Three phase voltage when CHB cells are under full shading

Figure 4.46 clearly describes the transient state while the phase voltages of the PV grid-connected system with cascaded H-bridge converter experiences unbalanced phase voltages due to full shading on a couple of CHB converter cells. As shown in the figure, the voltages' amplitude at phases A and B have the maximum amplitude of 174V, which exhibits the healthy phases. However, Phases C encounters a fully shaded cell, and as a result, phase C provides $\frac{2}{3}$ voltage of what phase A is generating; thus, the maximum voltage amplitude is just 116V.

After 0.25 seconds, the control scheme of the DC/DC converter has boosted the voltage under observation of balancing model and central power injection model.

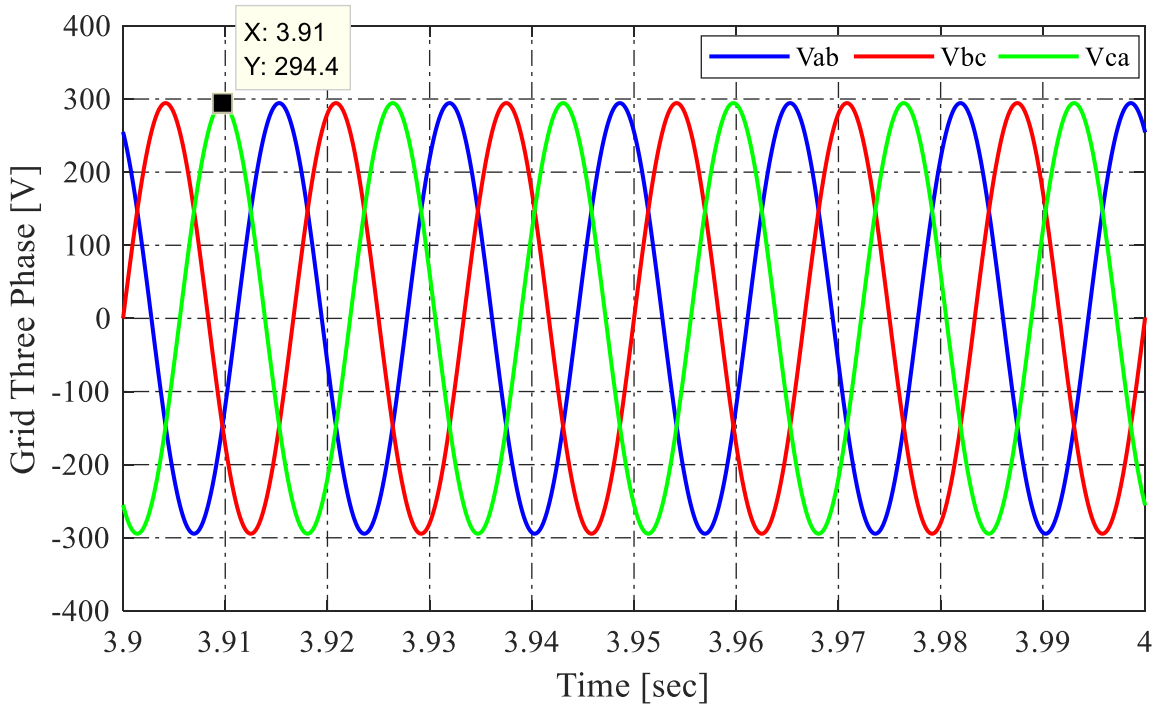

Figure 4.47: Three phase voltages of the utility grid

In Figure 4.44, the line to line voltages' shapes look dissimilar because during severe shading each phase synthesizes differently. Moreover, phases A and B have seven levels, and phase C has five levels. During the boosting process, the obtainable voltage levels per phase are limited to unshaded CHB's cell. This also shows the DC/DC converter boosting the DC link voltage and respond to the desired output (DC link reference) by changing the duty cycle to fulfill the output voltage. Therefore, the represented simulation results validate the feasibility of the proposed control topology. It is clear that the PV system with no control of multilevel grid-connected inverters will stop operating due voltage mismatch, which highlights the advantages of utilizing such controls for the CHB converter. Furthermore, the structures of the topology possess the ability to further improve the generation range and increase the efficiency of the system. The figure confirms that only the unshaded CHB cell boosts to converge to the reference DC link voltage value, achieve rebalanced status and remain under power injection conditions.

Figure 4.47 shows line to line voltages of the utility grid at normal operation and, as depicted, the line to line voltages are balanced with 120^{o} phase shift and a peak of 294.4V.

Table 4.3: Simulation Results at Steady State Performance Using a Classical Inverter

Description	Parameters	Measured Values
PV voltage [V]	V_{MPP}	262
PV current [A]	I_{MPP}	7.59
DC link voltage [V]	V_{dc_link}	350
Line to line grid voltage [V]	V_{LL}^{grid} (RMS)	208.20
RMS value of the injected current [A]	@ PF=1.0	5.309
	@ PF=0.8	6.96
	@ PF=0.5	8.64

The control of maximum power with global search makes each H-bridge cell supply different power levels, allowing for each H-bridge cell an independent maximum power point tracking under observation of the power injection model.

Table 4.4: Simulation Results at Steady State Performance Using CHB

Description	Parameters	Measured Values
PV voltage [V]/phase	V_{MPP}	157.8
PV current [A]/phase	I_{MPP}	7.59
DC link voltage [V]/phase	V_{dc_link}	174
Line to line grid voltage [V] at CHB Terminal	V_{LL}^{CHB} (RMS)	246.11
Line to line grid voltage [V]	V_{LL}^{grid} (RMS)	208.20
V_{LL} Average Total Harmonic Distortion with CHB	Avg. CHB THD [%]	6.38%
V_{LL} at Fully Shaded Cell CHB	Avg. THD [%]	8.03%

Chapter 5

4.3 Conclusion

PV grid-tied systems have a promising future due to increasing interest. The rapid growth indicates that solar power will successfully find its place among all other renewable energy resources in the coming future. The most important overall objective of this dissertation is to further improve the PV grid-connected systems to become easy to implement, more efficient, exhibit better performance, and less expansive. This work accomplishes this task not only by increasing the captured PV power and reinforcing the conversion efficiency via an effective control, but also through power factor control and reducing the converter design costs. Therefore, the proposed work enhances the reliability of the PV grid-tied systems strongly by extending the operation in presence of modules mismatch and minimize the converter cost. The following concludes all the contributions of this work.

First, three selected DC/DC converters were mathematically modeled in this dissertation. The models are used to analyze the dynamic performance of the three selected DC/DC converters. The well-derived transfer functions with respect to the duty cycle are effectively describe the dynamic

performance of SEPIC, Flyback, and Positive Buck-Boost. This analysis helps the identification of the best and most suitable candidate converter for the new PV grid-tied system.

Second, the dissertation introduces a new adaptive PV power extracting strategy in order to harvest the maximum available power at any time during day under various weather conditions. The PV system is fully controlled through an algorithm-based model predictive control technique with unique properties. While the operating point varies nonlinearly as a function of ambient temperature and irradiance, the proposed strategy can successfully track the MPP by moving the current operating point to either one of two predicted points at sampling time of (k+1) based on optimization towards the maximum accessible peak. In addition, the new technique can be digitally implemented using various types of microcontrollers in any PV system without any limitations.

Third, the new power harvesting method is enhanced by developing a new global MPP search method for mitigating the consequences of partial shading. The global search algorithm presents higher degree of efficacy by 99.8% and can effectively addresses all investigated scenarios. The proposed global approach is designed to launch in presence of a significant power drop or through routine interrupts.

Fourth, this dissertation attempts to minimize the converter cost by introducing a new current sensorless control model for Positive Buck Boost DC/DC converter based on the concepts of model predictive control as well. The cost reduction is noticeable when the PV system utilizes large number of current sensors.

Fifth, this work proposes a power balancing technique for injection of balanced three-phase power into the grid via a Cascaded H-Bridge (CHB) converter topology which brings together the entire system and results in the final proposed PV power system. The resulting PV system offers

enhanced reliability by guaranteeing effective system operation under unbalanced phase voltages caused by severe partial shading. The FPSC technique was employed to achieve balanced three phase voltages when the three phase PV system experiences full shading.

Finally, results are provided and discussed for each abovementioned sections to verify the operation of the proposed strategies. The experimental results of the proposed PV harvesting strategy and pervious methods were compared to validate the feasibility. On the other hand, simulation results of the grid-tied system have shown an excellent agreement with the derived theories and can be clearly observed that the introduced PV grid-tied system offers balanced operation in case of mismatch scenarios.

Bibliography

[1] I. E. Agency, "Global Energy & CO2 Status Report 2017," 2018, Available: https://www.iea.org/publications/freepublications/publication/GECO2017.pdf.

[2] M. M. Rojas-Downing, A. P. Nejadhashemi, T. Harrigan, and S. A. Woznicki, "Climate change and livestock: Impacts, adaptation, and mitigation," *Climate Risk Management,* vol. 16, pp. 145-163, 2017/01/01/ 2017.

[3] B. Kroposki *et al.*, "Achieving a 100% Renewable Grid: Operating Electric Power Systems with Extremely High Levels of Variable Renewable Energy," *IEEE Power and Energy Magazine,* vol. 15, no. 2, pp. 61-73, 2017.

[4] H. Wang, M. Liserre, and F. Blaabjerg, "Toward Reliable Power Electronics: Challenges, Design Tools, and Opportunities," *IEEE Industrial Electronics Magazine,* vol. 7, no. 2, pp. 17-26, 2013.

[5] REN21, "Highlights of the REN21 Renewables 2018 Global Status Report in Perspective," *Advanced The Global Renewable Energy Transition,* 2018.

[6] U. S. E. I. Administration, "EIA projects 28% increase in world energy use by 2040," in "TODAY IN ENERGY," 2017, Available: https://www.eia.gov/todayinenergy/detail.php?id=32912.

[7] I. E. Agency, "Renewables 2017," 2017, Available: https://www.iea.org/publications/renewables2017/.

[8] A. v. Jouanne and T. K. A. Brekken, "Ocean and Geothermal Energy Systems," *Proceedings of the IEEE,* vol. 105, no. 11, pp. 2147-2165, 2017.

[9] U. S. E. I. Administration. (2017). *Geothermal Explained*. Available: https://www.eia.gov/energyexplained/index.php?page=geothermal_home

[10] Y. Noorollahi, M. Pourarshad, and A. Veisi, "Solar-assisted geothermal power generation hybrid system from abandoned oil/gas wells," *IET Renewable Power Generation,* vol. 11, no. 6, pp. 771-777, 2017.

[11] U. S. E. I. Administration. (2018). *Hydropower Explained*. Available: https://www.eia.gov/energyexplained/index.php?page=hydropower_home

[12] U. S. E. I. Administration. (2017). *Wind Explained*. Available: https://www.eia.gov/energyexplained/index.php?page=wind_home

[13] U. S. E. I. Administration. (2018). *Biomass Explained*. Available: https://www.eia.gov/energyexplained/index.php?page=biomass_home

[14] L. Yuanyuan. (2017). *China's Solar PV Market Passes 100 GW Milestone*. Available: https://www.renewableenergyworld.com/articles/2017/09/china-s-solar-pv-market-passes-100-gw-milestone.html

[15] G. Energy. (2017). *Global PV capacity is expected to reach 969GW by 2025*. Available: https://www.power-technology.com/comment/global-pv-capacity-expected-reach-969gw-2025/

[16] engineering.com. (2018). *Photovoltaics*. Available: https://www.engineering.com/SustainableEngineering/RenewableEnergyEngineering/SolarEnergyEngineering/Photovoltaics/tabid/3890/Default.aspx

[17] M. G. Villalva, J. R. Gazoli, and E. R. Filho, "Comprehensive Approach to Modeling and Simulation of Photovoltaic Arrays," *IEEE Transactions on Power Electronics,* vol. 24, no. 5, pp. 1198-1208, 2009.

[18] A. S. Sedra and K. C. Smith, *Microelectronic Circuits*. London, U.K: Oxford Univ. Press, 2006.

[19] H. J. Moller, *Semiconductors for Solar Cells*. Norwood, MA: Artech House, 1993.

[20] A. S. C. Ltd. (2018). *How a PV Module Works*. Available: http://www.apricus.com/solar-pv-systems-pv-panels-19.html#.W7zF4WhKhaT

[21] J. Ahmed and Z. Salam, "An Improved Method to Predict the Position of Maximum Power Point During Partial Shading for PV Arrays," *IEEE Transactions on Industrial Informatics,* vol. 11, no. 6, pp. 1378-1387, 2015.

[22] S. Dongaonkar, C. Deline, and M. A. Alam, "Performance and Reliability Implications of Two-Dimensional Shading in Monolithic Thin-Film Photovoltaic Modules," *IEEE Journal of Photovoltaics,* vol. 3, no. 4, pp. 1367-1375, 2013.

[23] M. Z. S. El-Dein, M. Kazerani, and M. M. A. Salama, "Optimal Photovoltaic Array Reconfiguration to Reduce Partial Shading Losses," *IEEE Transactions on Sustainable Energy,* vol. 4, no. 1, pp. 145-153, 2013.

[24] S. Moballegh and J. Jiang, "Modeling, Prediction, and Experimental Validations of Power Peaks of PV Arrays Under Partial Shading Conditions," *IEEE Transactions on Sustainable Energy,* vol. 5, no. 1, pp. 293-300, 2014.

[25] Y. Wang and P. Hsu, "Analytical modelling of partial shading and different orientation of photovoltaic modules," *IET Renewable Power Generation,* vol. 4, no. 3, pp. 272-282, 2010.

[26] W. Chen and C. Tsai, "Optimal Balancing Control for Tracking Theoretical Global MPP of Series PV Modules Subject to Partial Shading," *IEEE Transactions on Industrial Electronics*, vol. 62, no. 8, pp. 4837-4848, 2015.
[27] A. M. S. Furtado, F. Bradaschia, M. C. Cavalcanti, and L. R. Limongi, "A Reduced Voltage Range Global Maximum Power Point Tracking Algorithm for Photovoltaic Systems Under Partial Shading Conditions," *IEEE Transactions on Industrial Electronics*, vol. 65, no. 4, pp. 3252-3262, 2018.
[28] K. Kobayashi, I. Takano, and Y. Sawada, "A study on a two stage maximum power point tracking control of a photovoltaic system under partially shaded insolation conditions," in *2003 IEEE Power Engineering Society General Meeting (IEEE Cat. No.03CH37491)*, 2003, vol. 4, pp. 2612-2617 Vol. 4.
[29] H. Patel and V. Agarwal, "Maximum Power Point Tracking Scheme for PV Systems Operating Under Partially Shaded Conditions," *IEEE Transactions on Industrial Electronics*, vol. 55, no. 4, pp. 1689-1698, 2008.
[30] M. Uno and A. Kukita, "Two-Switch Voltage Equalizer Using an LLC Resonant Inverter and Voltage Multiplier for Partially Shaded Series-Connected Photovoltaic Modules," *IEEE Transactions on Industry Applications*, vol. 51, no. 2, pp. 1587-1601, 2015.
[31] E. Díaz-Dorado, A. Suárez-García, C. Carrillo, and J. Cidrás, "Influence of the shadows in photovoltaic systems with different configurations of bypass diodes," in *SPEEDAM 2010*, 2010, pp. 134-139.
[32] C. Greacen and D. Green, "The role of bypass diodes in the failure of solar battery charging stations in Thailand," *Solar Energy Materials and Solar Cells*, vol. 70, no. 2, pp. 141-149, 2001/12/15/ 2001.
[33] H. Tian, F. Mancilla–David, K. Ellis, E. Muljadi, and P. Jenkins, "Determination of the optimal configuration for a photovoltaic array depending on the shading condition," *Solar Energy*, vol. 95, pp. 1-12, 2013/09/01/ 2013.
[34] H. Ziar, S. Mansourpour, E. Afjei, and M. Kazemi, "Bypass diode characteristic effect on the behavior of solar PV array at shadow condition," in *2012 3rd Power Electronics and Drive Systems Technology (PEDSTC)*, 2012, pp. 229-233.
[35] H. Ziar, S. Mansourpour, A. Arjhangmehr, A. Salimi, and E. Afjei, "Analysis of thermal effect on solar cells with considering bypass diodes at shadow condition through binary coding method," in *2011 2nd International Conference on Electric Power and Energy Conversion Systems (EPECS)*, 2011, pp. 1-6.
[36] E. I. Batzelis, I. A. Routsolias, and S. A. Papathanassiou, "An Explicit PV String Model Based on the Lambert<formula formulatype="inline"><tex Notation="TeX">W</tex></formula>Function and Simplified MPP Expressions for Operation Under Partial Shading," *IEEE Transactions on Sustainable Energy*, vol. 5, no. 1, pp. 301-312, 2014.
[37] M. Elliott, M. McIntyre, J. Lathan, and S. Tidwell, "Partial shading abatement through cell level inverter system topology," in *2015 IEEE 42nd Photovoltaic Specialist Conference (PVSC)*, 2015, pp. 1-5.
[38] A. Ahmed, L. Ran, S. Moon, and J. Park, "A Fast PV Power Tracking Control Algorithm With Reduced Power Mode," *IEEE Transactions on Energy Conversion*, vol. 28, no. 3, pp. 565-575, 2013.
[39] A. A. Elbaset, H. Ali, M. A.-E. Sattar, and M. Khaled, "Implementation of a modified perturb and observe maximum power point tracking algorithm for photovoltaic system using an embedded microcontroller," *IET Renewable Power Generation*, vol. 10, no. 4, pp. 551-560, 2016.
[40] N. Femia, G. Petrone, G. Spagnuolo, and M. Vitelli, "Optimization of perturb and observe maximum power point tracking method," *IEEE Transactions on Power Electronics*, vol. 20, no. 4, pp. 963-973, 2005.
[41] N. Femia, G. Petrone, G. Spagnuolo, and M. Vitelli, "A Technique for Improving P&O MPPT Performances of Double-Stage Grid-Connected Photovoltaic Systems," *IEEE Transactions on Industrial Electronics*, vol. 56, no. 11, pp. 4473-4482, 2009.
[42] F. Paz and M. Ordonez, "Zero Oscillation and Irradiance Slope Tracking for Photovoltaic MPPT," *IEEE Transactions on Industrial Electronics*, vol. 61, no. 11, pp. 6138-6147, 2014.
[43] J. Teng, W. Huang, T. Hsu, and C. Wang, "Novel and Fast Maximum Power Point Tracking for Photovoltaic Generation," *IEEE Transactions on Industrial Electronics*, vol. 63, no. 8, pp. 4955-4966, 2016.
[44] N. S. D. Souza, L. A. C. Lopes, and L. XueJun, "An Intelligent Maximum Power Point Tracker Using Peak Current Control," in *2005 IEEE 36th Power Electronics Specialists Conference*, 2005, p. 172.
[45] T. Esram and P. L. Chapman, "Comparison of Photovoltaic Array Maximum Power Point Tracking Techniques," *IEEE Transactions on Energy Conversion*, vol. 22, no. 2, pp. 439-449, 2007.
[46] O. Wasynezuk, "Dynamic Behavior of a Class of Photovoltaic Power Systems," *IEEE Transactions on Power Apparatus and Systems*, vol. PAS-102, no. 9, pp. 3031-3037, 1983.
[47] A. Al-Amoudi and L. Zhang, "Optimal control of a grid-connected PV system for maximum power point tracking and unity power factor," in *1998 Seventh International Conference on Power Electronics and Variable Speed Drives (IEE Conf. Publ. No. 456)*, 1998, pp. 80-85.

[48] H. Chihchiang and L. Jong Rong, "DSP-based controller application in battery storage of photovoltaic system," in *Proceedings of the 1996 IEEE IECON. 22nd International Conference on Industrial Electronics, Control, and Instrumentation*, 1996, vol. 3, pp. 1705-1710 vol.3.

[49] O. Wasynczuk, "Dynamic Behavior of a Class of Photovoltaic Power Systems," *IEEE Power Engineering Review*, vol. PER-3, no. 9, pp. 36-37, 1983.

[50] W. J. A. Teulings, J. C. Marpinard, A. Capel, and D. O. Sullivan, "A new maximum power point tracking system," in *Proceedings of IEEE Power Electronics Specialist Conference - PESC '93*, 1993, pp. 833-838.

[51] A. Ramyar, H. Iman-Eini, and S. Farhangi, "Global Maximum Power Point Tracking Method for Photovoltaic Arrays Under Partial Shading Conditions," *IEEE Transactions on Industrial Electronics*, vol. 64, no. 4, pp. 2855-2864, 2017.

[52] A. F. Boehringer, "Self-Adapting dc Converter for Solar Spacecraft Power Supply Selbstanpassender Gleichstromwandler für die Energieversorgung eines Sonnensatelliten," *IEEE Transactions on Aerospace and Electronic Systems*, vol. AES-4, no. 1, pp. 102-111, 1968.

[53] A. Saidi and C. Benachaiba, "Comparison of IC and P&O algorithms in MPPT for grid connected PV module," in *2016 8th International Conference on Modelling, Identification and Control (ICMIC)*, 2016, pp. 213-218.

[54] R. F. A. DOLARA, S. LEVA "Energy Comparison of Seven MPPT Techniquesfor PV Systems," vol. 01, p. 11, 2009.

[55] R. M. Hilloowala and A. M. Sharaf, "A rule-based fuzzy logic controller for a PWM inverter in photo-voltaic energy conversion scheme," in *Conference Record of the 1992 IEEE Industry Applications Society Annual Meeting*, 1992, pp. 762-769 vol.1.

[56] Y. Chen, Y. Wu, C. Song, and Y. Chen, "Design and Implementation of Energy Management System With Fuzzy Control for DC Microgrid Systems," *IEEE Transactions on Power Electronics*, vol. 28, no. 4, pp. 1563-1570, 2013.

[57] W. Chung-Yuen, K. Duk-Heon, K. Sei-Chan, K. Won-Sam, and K. Hack-Sung, "A new maximum power point tracker of photovoltaic arrays using fuzzy controller," in *Proceedings of 1994 Power Electronics Specialist Conference - PESC'94*, 1994, vol. 1, pp. 396-403 vol.1.

[58] A. A. Nabulsi and R. Dhaouadi, "Efficiency Optimization of a DSP-Based Standalone PV System Using Fuzzy Logic and Dual-MPPT Control," *IEEE Transactions on Industrial Informatics*, vol. 8, no. 3, pp. 573-584, 2012.

[59] R. M. Rezoug, R. Chenni, and D. Taibi, "Fuzzy Logic-Based Perturb and Observe Algorithm with Variable Step of a Reference Voltage for Solar Permanent Magnet Synchronous Motor Drive System Fed by Direct-Connected Photovoltaic Array," *Energies*, vol. 11, no. 2, 2018.

[60] C. Cecati, F. Ciancetta, and P. Siano, "A Multilevel Inverter for Photovoltaic Systems With Fuzzy Logic Control," *IEEE Transactions on Industrial Electronics*, vol. 57, no. 12, pp. 4115-4125, 2010.

[61] T. Hiyama, S. Kouzuma, and T. Imakubo, "Identification of optimal operating point of PV modules using neural network for real time maximum power tracking control," *IEEE Transactions on Energy Conversion*, vol. 10, no. 2, pp. 360-367, 1995.

[62] L. Zhang, B. Yunfei, and A. Al-Amoudi, "GA-RBF neural network based maximum power point tracking for grid-connected photovoltaic systems," in *2002 International Conference on Power Electronics, Machines and Drives (Conf. Publ. No. 487)*, 2002, pp. 18-23.

[63] R. Subha and S. Himavathi, "Neural network based maximum power point tracking scheme for PV systems operating under partially shaded conditions," in *2014 International Conference on Advances in Green Energy (ICAGE)*, 2014, pp. 39-43.

[64] P. Bhatnagar and R. K. Nema, "Maximum power point tracking control techniques: State-of-the-art in photovoltaic applications," *Renewable and Sustainable Energy Reviews*, vol. 23, pp. 224-241, 2013/07/01/ 2013.

[65] M. A. Danandeh and S. M. Mousavi G, "Comparative and comprehensive review of maximum power point tracking methods for PV cells," *Renewable and Sustainable Energy Reviews*, vol. 82, pp. 2743-2767, 2018/02/01/ 2018.

[66] A. Gupta, Y. Chauhan, and R. Kumar Pachauri, *A comparative investigation of maximum power point tracking methods for solar PV system*. 2016, pp. 236-253.

[67] I. Abdalla, J. Corda, and L. Zhang, "Multilevel DC-Link Inverter and Control Algorithm to Overcome the PV Partial Shading," *IEEE Transactions on Power Electronics*, vol. 28, no. 1, pp. 14-18, 2013.

[68] K. Chen, S. Tian, Y. Cheng, and L. Bai, "An Improved MPPT Controller for Photovoltaic System Under Partial Shading Condition," *IEEE Transactions on Sustainable Energy*, vol. 5, no. 3, pp. 978-985, 2014.

[69] Y. Hu, W. Cao, J. Wu, B. Ji, and D. Holliday, "Thermography-Based Virtual MPPT Scheme for Improving PV Energy Efficiency Under Partial Shading Conditions," *IEEE Transactions on Power Electronics*, vol. 29, no. 11, pp. 5667-5672, 2014.

[70] K. Ishaque and Z. Salam, "A Deterministic Particle Swarm Optimization Maximum Power Point Tracker for Photovoltaic System Under Partial Shading Condition," *IEEE Transactions on Industrial Electronics,* vol. 60, no. 8, pp. 3195-3206, 2013.
[71] K. Ishaque, Z. Salam, M. Amjad, and S. Mekhilef, "An Improved Particle Swarm Optimization (PSO)–Based MPPT for PV With Reduced Steady-State Oscillation," *IEEE Transactions on Power Electronics,* vol. 27, no. 8, pp. 3627-3638, 2012.
[72] A. Kouchaki, H. Iman-Eini, and B. Asaei, "A new maximum power point tracking strategy for PV arrays under uniform and non-uniform insolation conditions," *Solar Energy,* vol. 91, pp. 221-232, 2013/05/01/ 2013.
[73] E. Koutroulis and F. Blaabjerg, "A New Technique for Tracking the Global Maximum Power Point of PV Arrays Operating Under Partial-Shading Conditions," *IEEE Journal of Photovoltaics,* vol. 2, no. 2, pp. 184-190, 2012.
[74] Y. Liu, S. Huang, J. Huang, and W. Liang, "A Particle Swarm Optimization-Based Maximum Power Point Tracking Algorithm for PV Systems Operating Under Partially Shaded Conditions," *IEEE Transactions on Energy Conversion,* vol. 27, no. 4, pp. 1027-1035, 2012.
[75] S. Lyden and M. E. Haque, "A Simulated Annealing Global Maximum Power Point Tracking Approach for PV Modules Under Partial Shading Conditions," *IEEE Transactions on Power Electronics,* vol. 31, no. 6, pp. 4171-4181, 2016.
[76] M. Miyatake, M. Veerachary, F. Toriumi, N. Fujii, and H. Ko, "Maximum Power Point Tracking of Multiple Photovoltaic Arrays: A PSO Approach," *IEEE Transactions on Aerospace and Electronic Systems,* vol. 47, no. 1, pp. 367-380, 2011.
[77] T. L. Nguyen and K. Low, "A Global Maximum Power Point Tracking Scheme Employing DIRECT Search Algorithm for Photovoltaic Systems," *IEEE Transactions on Industrial Electronics,* vol. 57, no. 10, pp. 3456-3467, 2010.
[78] P. Sharma and V. Agarwal, "Exact Maximum Power Point Tracking of Grid-Connected Partially Shaded PV Source Using Current Compensation Concept," *IEEE Transactions on Power Electronics,* vol. 29, no. 9, pp. 4684-4692, 2014.
[79] K. Sundareswaran, S. Peddapati, and S. Palani, "MPPT of PV Systems Under Partial Shaded Conditions Through a Colony of Flashing Fireflies," *IEEE Transactions on Energy Conversion,* vol. 29, no. 2, pp. 463-472, 2014.
[80] Syafaruddin, E. Karatepe, and T. Hiyama, "Artificial neural network-polar coordinated fuzzy controller based maximum power point tracking control under partially shaded conditions," *IET Renewable Power Generation,* vol. 3, no. 2, pp. 239-253, 2009.
[81] K. S. Tey and S. Mekhilef, "Modified Incremental Conductance Algorithm for Photovoltaic System Under Partial Shading Conditions and Load Variation," *IEEE Transactions on Industrial Electronics,* vol. 61, no. 10, pp. 5384-5392, 2014.
[82] Y. Wang, Y. Li, and X. Ruan, "High-Accuracy and Fast-Speed MPPT Methods for PV String Under Partially Shaded Conditions," *IEEE Transactions on Industrial Electronics,* vol. 63, no. 1, pp. 235-245, 2016.
[83] P. Sharma and V. Agarwal, "Maximum Power Extraction From a Partially Shaded PV Array Using Shunt-Series Compensation," *IEEE Journal of Photovoltaics,* vol. 4, no. 4, pp. 1128-1137, 2014.
[84] T. Sen, N. Pragallapati, V. Agarwal, and R. Kumar, "Global maximum power point tracking of PV arrays under partial shading conditions using a modified particle velocity-based PSO technique," *IET Renewable Power Generation,* vol. 12, no. 5, pp. 555-564, 2018.
[85] P. Lezana and G. Ortiz, "Extended Operation of Cascade Multicell Converters Under Fault Condition," *IEEE Transactions on Industrial Electronics,* vol. 56, no. 7, pp. 2697-2703, 2009.
[86] P. Midya, P. T. Krein, and M. F. Greuel, "Sensorless current mode control-an observer-based technique for DC-DC converters," *IEEE Transactions on Power Electronics,* vol. 16, no. 4, pp. 522-526, 2001.
[87] G. M. Dousoky, E. M. Ahmed, and M. Shoyama, "Current-sensorless MPPT with DC-DC boost converter for Photovoltaic battery chargers," in *2012 IEEE Energy Conversion Congress and Exposition (ECCE)*, 2012, pp. 1607-1614.
[88] N. Kasa, T. Iida, and C. Liang, "Flyback Inverter Controlled by Sensorless Current MPPT for Photovoltaic Power System," *IEEE Transactions on Industrial Electronics,* vol. 52, no. 4, pp. 1145-1152, 2005.
[89] E. Dallago, D. G. Finarelli, U. P. Gianazza, A. L. Barnabei, and A. Liberale, "Theoretical and Experimental Analysis of an MPP Detection Algorithm Employing a Single-Voltage Sensor Only and a Noisy Signal," *IEEE Transactions on Power Electronics,* vol. 28, no. 11, pp. 5088-5097, 2013.
[90] M. Bond and J. Park, "Current-Sensorless Power Estimation and MPPT Implementation for Thermoelectric Generators," *IEEE Transactions on Industrial Electronics,* vol. 62, no. 9, pp. 5539-5548, 2015.

[91] R. Min, Q. Tong, Q. Zhang, X. Zou, K. Yu, and Z. Liu, "Digital Sensorless Current Mode Control Based on Charge Balance Principle and Dual Current Error Compensation for DC–DC Converters in DCM," *IEEE Transactions on Industrial Electronics*, vol. 63, no. 1, pp. 155-166, 2016.
[92] M. Metry, M. B. Shadmand, R. S. Balog, and H. Abu-Rub, "MPPT of Photovoltaic Systems Using Sensorless Current-Based Model Predictive Control," *IEEE Transactions on Industry Applications*, vol. 53, no. 2, pp. 1157-1167, 2017.
[93] P. W. Hammond, "A new approach to enhance power quality for medium voltage AC drives," *IEEE Transactions on Industry Applications*, vol. 33, no. 1, pp. 202-208, 1997.
[94] T. A. Meynard, H. Foch, P. Thomas, J. Courault, R. Jakob, and M. Nahrstaedt, "Multicell converters: basic concepts and industry applications," *IEEE Transactions on Industrial Electronics*, vol. 49, no. 5, pp. 955-964, 2002.
[95] A. Nabae, I. Takahashi, and H. Akagi, "A New Neutral-Point-Clamped PWM Inverter," *IEEE Transactions on Industry Applications*, vol. IA-17, no. 5, pp. 518-523, 1981.
[96] M. Ma, L. Hu, A. Chen, and X. He, "Reconfiguration of Carrier-Based Modulation Strategy for Fault Tolerant Multilevel Inverters," *IEEE Transactions on Power Electronics*, vol. 22, no. 5, pp. 2050-2060, 2007.
[97] K. Xiaomin, K. A. Corzine, and M. W. Wielebski, "Overdistention operation of cascaded multilevel inverters," *IEEE Transactions on Industry Applications*, vol. 42, no. 3, pp. 817-824, 2006.
[98] M. Marchesoni, M. Mazzucchelli, and S. Tenconi, "A non conventional power converter for plasma stabilization," in *PESC '88 Record., 19th Annual IEEE Power Electronics Specialists Conference*, 1988, pp. 122-129 vol.1.
[99] B. Lin and C. Huang, "Implementation of a Three-Phase Capacitor-Clamped Active Power Filter Under Unbalanced Condition," *IEEE Transactions on Industrial Electronics*, vol. 53, no. 5, pp. 1621-1630, 2006.
[100] T. A. Meynard and H. Foch, "Multi-Level Choppers for High Voltage Applications," *EPE Journal*, vol. 2, no. 1, pp. 45-50, 1992/01/01 1992.
[101] J. Rodriguez *et al.*, "Multilevel Converters: An Enabling Technology for High-Power Applications," *Proceedings of the IEEE*, vol. 97, no. 11, pp. 1786-1817, 2009.
[102] P. Fang Zheng, J. W. McKeever, and D. J. Adams, "A power line conditioner using cascade multilevel inverters for distribution systems," *IEEE Transactions on Industry Applications*, vol. 34, no. 6, pp. 1293-1298, 1998.
[103] F. Z. Peng, J. W. McKeever, and D. J. Adams, "Cascade multilevel inverters for utility applications," in *Proceedings of the IECON'97 23rd International Conference on Industrial Electronics, Control, and Instrumentation (Cat. No.97CH36066)*, 1997, vol. 2, pp. 437-442 vol.2.
[104] L. Yiqiao and C. O. Nwankpa, "A new type of STATCOM based on cascading voltage-source inverters with phase-shifted unipolar SPWM," *IEEE Transactions on Industry Applications*, vol. 35, no. 5, pp. 1118-1123, 1999.
[105] L. M. Tolbert and F. Z. Peng, "Multilevel converters as a utility interface for renewable energy systems," in *2000 Power Engineering Society Summer Meeting (Cat. No.00CH37134)*, 2000, vol. 2, pp. 1271-1274 vol. 2.
[106] E. Afshari *et al.*, "Control Strategy for Three-Phase Grid-Connected PV Inverters Enabling Current Limitation Under Unbalanced Faults," *IEEE Transactions on Industrial Electronics*, vol. 64, no. 11, pp. 8908-8918, 2017.
[107] F. Carnielutti and H. Pinheiro, "Hybrid Modulation Strategy for Asymmetrical Cascaded Multilevel Converters Under Normal and Fault Conditions," *IEEE Transactions on Industrial Electronics*, vol. 63, no. 1, pp. 92-101, 2016.
[108] P. Correa, M. Pacas, and J. Rodriguez, "Modulation Strategies for Fault-Tolerant Operation of H-Bridge Multilevel Inverters," in *2006 IEEE International Symposium on Industrial Electronics*, 2006, vol. 2, pp. 1589-1594.
[109] B. Gemmell, J. Dorn, D. Retzmann, and D. Soerangr, "Prospects of multilevel VSC technologies for power transmission," in *2008 IEEE/PES Transmission and Distribution Conference and Exposition*, 2008, pp. 1-16.
[110] S. Kouro *et al.*, "Recent Advances and Industrial Applications of Multilevel Converters," *IEEE Transactions on Industrial Electronics*, vol. 57, no. 8, pp. 2553-2580, 2010.
[111] P. Lezana, J. Pou, T. A. Meynard, J. Rodriguez, S. Ceballos, and F. Richardeau, "Survey on Fault Operation on Multilevel Inverters," *IEEE Transactions on Industrial Electronics*, vol. 57, no. 7, pp. 2207-2218, 2010.
[112] P. Lezana, J. Rodriguez, and D. A. Oyarzun, "Cascaded Multilevel Inverter With Regeneration Capability and Reduced Number of Switches," *IEEE Transactions on Industrial Electronics*, vol. 55, no. 3, pp. 1059-1066, 2008.
[113] B. Mirafzal, "Survey of Fault-Tolerance Techniques for Three-Phase Voltage Source Inverters," *IEEE Transactions on Industrial Electronics*, vol. 61, no. 10, pp. 5192-5202, 2014.

[114] J. Rodriguez, P. W. Hammond, J. Pontt, R. Musalem, P. Lezana, and M. J. Escobar, "Operation of a medium-voltage drive under faulty conditions," *IEEE Transactions on Industrial Electronics*, vol. 52, no. 4, pp. 1080-1085, 2005.
[115] W. Song and A. Q. Huang, "Fault-Tolerant Design and Control Strategy for Cascaded H-Bridge Multilevel Converter-Based STATCOM," *IEEE Transactions on Industrial Electronics*, vol. 57, no. 8, pp. 2700-2708, 2010.
[116] C. D. Townsend, Y. Yu, G. Konstantinou, and V. G. Agelidis, "Cascaded H-Bridge Multilevel PV Topology for Alleviation of Per-Phase Power Imbalances and Reduction of Second Harmonic Voltage Ripple," *IEEE Transactions on Power Electronics*, vol. 31, no. 8, pp. 5574-5586, 2016.
[117] W. Zhang, D. Xu, P. N. Enjeti, H. Li, J. T. Hawke, and H. S. Krishnamoorthy, "Survey on Fault-Tolerant Techniques for Power Electronic Converters," *IEEE Transactions on Power Electronics*, vol. 29, no. 12, pp. 6319-6331, 2014.
[118] C. Roncero-Clemente, E. Romero-Cadaval, M. Ruiz-Cortés, and O. Husev, "Carrier Level-Shifted Based Control Method for the PWM 3L-T-Type qZS Inverter With Capacitor Imbalance Compensation," *IEEE Transactions on Industrial Electronics*, vol. 65, no. 10, pp. 8297-8306, 2018.
[119] J. Rodriguez, L. Jih-Sheng, and P. Fang Zheng, "Multilevel inverters: a survey of topologies, controls, and applications," *IEEE Transactions on Industrial Electronics*, vol. 49, no. 4, pp. 724-738, 2002.
[120] "IEEE Standard for Interconnecting Distributed Resources with Electric Power Systems," *IEEE Std 1547-2003*, pp. 1-28, 2003.
[121] H. Jafarian, R. Cox, J. H. Enslin, S. Bhowmik, and B. Parkhideh, "Decentralized Active and Reactive Power Control for an AC-Stacked PV Inverter With Single Member Phase Compensation," *IEEE Transactions on Industry Applications*, vol. 54, no. 1, pp. 345-355, 2018.
[122] S. Jain and V. Agarwal, "A Single-Stage Grid Connected Inverter Topology for Solar PV Systems With Maximum Power Point Tracking," *IEEE Transactions on Power Electronics*, vol. 22, no. 5, pp. 1928-1940, 2007.
[123] "IEEE Standard for Interconnecting Distributed Resources with Electric Power Systems - Amendment 1," *IEEE Std 1547a-2014 (Amendment to IEEE Std 1547-2003)*, pp. 1-16, 2014.
[124] L. Jinjun, Y. Jun, and W. Zhaoan, "A new approach for single-phase harmonic current detecting and its application in a hybrid active power filter," in *IECON'99. Conference Proceedings. 25th Annual Conference of the IEEE Industrial Electronics Society (Cat. No.99CH37029)*, 1999, vol. 2, pp. 849-854 vol.2.
[125] M. Saitou, N. Matsui, and T. Shimizu, "A control strategy of single-phase active filter using a novel d-q transformation," in *38th IAS Annual Meeting on Conference Record of the Industry Applications Conference, 2003.*, 2003, vol. 2, pp. 1222-1227 vol.2.
[126] Y. Yang, H. Wang, and F. Blaabjerg, "Reactive Power Injection Strategies for Single-Phase Photovoltaic Systems Considering Grid Requirements," *IEEE Transactions on Industry Applications*, vol. 50, no. 6, pp. 4065-4076, 2014.
[127] A. Cagnano, E. D. Tuglie, M. Liserre, and R. A. Mastromauro, "Online Optimal Reactive Power Control Strategy of PV Inverters," *IEEE Transactions on Industrial Electronics*, vol. 58, no. 10, pp. 4549-4558, 2011.
[128] C. Wang, K. Zhang, J. Xiong, Y. Xue, and W. Liu, "A Coordinated Compensation Strategy for Module Mismatch of CHB-PV Systems Based on Improved LS-PWM and Reactive Power Injection," *IEEE Transactions on Industrial Electronics*, vol. 66, no. 4, pp. 2825-2836, 2019.
[129] S. Lu and K. A. Corzine, "Advanced Control and Analysis of Cascaded Multilevel Converters Based on P-Q Compensation," *IEEE Transactions on Power Electronics*, vol. 22, no. 4, pp. 1242-1252, 2007.
[130] D. Ostojic, "A multilevel converter structure for grid-connected PV plants," PH.D, Electrical Engineering Department, 2010.
[131] J. Rodriguez, L. Moran, P. Correa, and C. Silva, "A vector control technique for medium-voltage multilevel inverters," *IEEE Transactions on Industrial Electronics*, vol. 49, no. 4, pp. 882-888, 2002.
[132] M. M. H. Abu-Rub, K. Al-Haddad, *Power Electronics for Renewable Energy Systems, Transportation and Industrial Applications*. New York, NY, USA: Wiley, 2014.
[133] A. V. Akkuratov and P. Troshin, *Conjugated Polymers with Benzothiadiazole, Benzoxadiazole, and Benzotriazole Moieties as Promising Semiconductor Materials for Organic Solar Cells*. 2014, pp. 414-442.
[134] J. R. a. P. Cortes, *Predictive Control of Power Converters and Electrical Drives*. New York, NY, USA: Wiley, 2012.
[135] J. B. R. a. D. Q. Mayne, *Model Predictive Control: Theory and Design*. Madison, WI, USA: Nob Hill Publishing, 2009.

[136] W. Sanmin, W. Bin, S. Rizzo, and N. Zargari, "Comparison of control schemes for multilevel inverter with faulty cells," in *30th Annual Conference of IEEE Industrial Electronics Society, 2004. IECON 2004*, 2004, vol. 2, pp. 1817-1822 Vol. 2.

[137] K. Irisawa, T. Saito, I. Takano, and Y. Sawada, "Maximum power point tracking control of photovoltaic generation system under non-uniform insolation by means of monitoring cells," in *Conference Record of the Twenty-Eighth IEEE Photovoltaic Specialists Conference - 2000 (Cat. No.00CH37036)*, 2000, pp. 1707-1710.

[138] P. S. Rao, G. S. Ilango, and C. Nagamani, "Maximum Power from PV Arrays Using a Fixed Configuration Under Different Shading Conditions," *IEEE Journal of Photovoltaics*, vol. 4, no. 2, pp. 679-686, 2014.

[139] A. A. Abushaiba, S. M. M. Eshtaiwi, and R. Ahmadi, "Dynamic performance analysis of a PV charger system," in *IECON 2014 - 40th Annual Conference of the IEEE Industrial Electronics Society*, 2014, pp. 2069-2074.

[140] A. A. Abushaiba, S. M. M. Eshtaiwi, and R. Ahmadi, "A new model predictive based Maximum Power Point Tracking method for photovoltaic applications," in *2016 IEEE International Conference on Electro Information Technology (EIT)*, 2016, pp. 0571-0575.